

CYTOSKELETAL MECHANICS IN ENDOTHELIAL CELLS

By

ROBERT JOHN RUSSELL

A DISSERTATION PRESENTED TO THE GRADUATE SCHOOL
OF THE UNIVERSITY OF FLORIDA IN PARTIAL FULFILLMENT
OF THE REQUIREMENTS FOR THE DEGREE OF
DOCTOR OF PHILOSOPHY

UNIVERSITY OF FLORIDA

2011

© 2011 Robert John Russell

To my parents and my lovely wife

ACKNOWLEDGMENTS

I would like to acknowledge the people who supported me during my time at the University of Florida and through my doctoral studies. I first would like to acknowledge my advisor Professor Tanmay Lele and my co-advisor Professor Richard Dickinson. Professor Lele was supportive and patient throughout my time here and his expertise was extremely helpful in both selecting problems and completing this work. Professor Dickinson provided an insightful perspective for my research and provided me experience with applying models to biological systems. Both advisors have provided me a great opportunity to learn how to conduct research and improve my knowledge of chemical engineering. I would like to thank the other members of my supervisory committee. Professor Benjamin Keselowsky has been supportive and offered helpful advice. I would like Professor Yiider Tseng for allowing me to start on my research in his lab as well being willing to discuss problems and offer advice as needed. I would also thank Professor Daniel Purich for holding the Cytoskeleton Journal Club through which I gained much insight into cytoskeletal processes. Professor Shen-Ling Xia provided me access and help with the multi-photon confocal microscope at the VA hospital.

I would also like my coworkers in the Lele Lab and other students that helped throughout my time at the University of Florida. First I would like to express my appreciation to Dr. Hengyi Xiao who taught me the necessary biology lab skills to get started doing research. Pei-Hsun Wu, TJ Chancellor, Jun Wu and Jiyeon Lee were always helpful in getting the lab running, figuring out new experimental techniques troubleshooting problems and discussing results. Jun and I had enjoyable time working on the microtubule project together. David Lovett and Alex Grubbs were supportive and helpful during my the end of my time in the lab. I would like to thank the undergraduates

that worked with me over the years most specifically Sunil Magroo and Sandra Nakasone.

I would like to thank all of my family members that supported me throughout the years and made this a reality. My parents have always been encouraging, loving and have motivated me to achieve my goals. They have always been willing to listen to me and give good advice on how to move forward. I would like to thank my brother for being a great friend and being supportive during my time in Florida. My wife's parents have been helpful to us during our time in Gainesville which we both appreciate. Lastly I would like to acknowledge the support and love of my wife Rose. Her patience, resourcefulness and success have always inspired me, and her encouragement and understanding have always motivated me. Without Rose I am certain that this would not have been possible and certainly not as enjoyable. I look forward to our future as we take another step together in life.

TABLE OF CONTENTS

	<u>page</u>
ACKNOWLEDGMENTS	4
LIST OF FIGURES.....	9
LIST OF TERMS	11
ABSTRACT	14
CHAPTER	
1 INTRODUCTION	16
Function of the Endothelium	16
Endothelial Cytoskeleton	17
Actin Cytoskeleton.....	17
Microtubule Cytoskeleton	18
Evidence for Stress Fibers in the Intact Endothelium	19
Microstructure of Endothelial Stress Fibers.....	21
Mechanics and Dynamics of Stress Fibers	23
Sarcomere Mechanics Models.....	25
Mechanics of Microtubules	26
Organization of this Document.....	27
2 SARCOMERE MECHANICS IN CAPILLARY ENDOTHELIAL CELLS	33
Materials and Methods.....	36
Cell Culture and Transfection	36
Laser Ablation of Stress Fibers	37
Image Correlation Based Tracking of Dense Bodies.....	39
Parameter Estimation for Sarcomere Model.....	41
Results and Discussion.....	42
Sarcomeres Contract in the Severed Stress Fiber	42
Potential Energy is not Stored in Severed Stress Fibers	44
A Mechanical Model for the Sarcomere	45
Insight into the Mechanics of Stress Fibers	48
Summary of Findings	49
3 SARCOMERE LENGTH FLUCTUATIONS AND FLOW IN CAPILLARY ENDOTHELIAL CELLS.....	58
Materials and Methods.....	59
Cell Culture and Transfections	59
Micropatterning of Bovine Capillary Endothelial Cells	60
Time- Lapse Imaging of Labeled Sarcomeres.....	61

Image Analysis	61
Results	62
Fluctuations in Sarcomere Length	62
Flow of Nascent Sarcomeres from Focal Adhesions	63
Sarcomere Flow Velocity from Focal Adhesions is Tension Independent	64
Sarcomeres are Consumed at 'Sinks'	64
Discussion	65
Summary of a Comprehensive Sarcomere Model	67
4 EFFECTS OF DYNEIN ON MICROTUBULE MECHANICS	78
Materials and Methods	79
Cell Culture, Plasmids and Transfection	79
Laser Ablation	80
Root Mean Squared Curvature Calculations	82
Results	84
Dynamics of Severed Microtubules	84
Dynein Inhibition Alters the Dynamics of Severed Microtubules	86
Discussion	87
Summary of Findings	89
5 CONCLUSIONS	96
Summary of Findings	96
Stress Fiber Sarcomere Mechanics	97
Sarcomere Dynamics in Endothelial Cells	98
Effects of Dynein on the Microtubule Force Balance	100
Future Work	100
Biophysical Analysis of Mechanical Factors Leading to Atherosclerosis	100
Force Transmission Between Endothelial Cells in a Mono-Layer	102
Mechanics of Myofilament Repair in C2C12 Myoblasts	104
APPENDIX	
A MATLAB CODE FOR ANALYZING SARCOMERE DYNAMICS	107
Dense Body Tracking Software	107
Correlation Processing Function	113
Paraboloid Fitting Function	113
Averaging Position Software	115
Sarcomere Length Calculation	119
Model Fitting Code	122
Four Parameter Fitting	123
Two Parameter Fitting	125
B MATLAB CODE FOR DETERMINING MICROTUBULE CURVATURE	127
Microtubule Tracing Code	127

Linear Gaussian Fitting Function.....	133
Curvature and Bending Energy Calculation Code	134
LIST OF REFERENCES	137
BIOGRAPHICAL SKETCH.....	147

LIST OF FIGURES

<u>Figure</u>	<u>page</u>
1-1 Schematic of forces exerted on the endothelium in the vasculature	29
1-2 Elements of the cellular cytoskeleton	30
1-3 Microstructure of stress fibers consists of sarcomeric subunits	31
1-4 Microtubules exhibit short wavelength buckling at the cell periphery	32
2-1 Sarcomeres contract in a severed fiber	50
2-2 Cartoon schematic of microscope system used for ablation and imaging	51
2-3 Time dependent length change of a sarcomere	52
2-4 Histograms of sarcomere contraction parameters	53
2-5 Potential energy is not stored in a severed stress fiber	54
2-6 Second example of potential energy not stored in a severed stress fiber	55
2-7 Fully contracted severed stress fibers do not relax when treated with ML7	56
2-8 Proposed mechanical model for the sarcomere	57
3-1 Sarcomeres undergo dynamic length fluctuations	71
3-2 Sarcomeres undergo length fluctuations in cells with confined shaped	72
3-3 Nascent sarcomeres flow from all focal adhesions	73
3-4 Nascent sarcomeres flow inwards from all focal adhesions in patterned cells ..	74
3-5 Sarcomere flow rate is independent of mechanical stress	75
3-6 Sarcomeres are consumed at sinks and join end-on to maintain tension	76
3-7 Sarcomeres are consumed to maintain tension	77
4-1 Depolymerization rates differ between plus-ended and minus-ended microtubules	90
4-2 Minus-ended microtubule fragments increase in curvature after severing	91
4-3 There is no correlation observed between the change in RMS curvature and either the initial RMS curvature or position of the microtubule	92

4-4	Bent microtubules are stable over significant time scales	93
4-5	Severed microtubules in dynein inhibited cells were observed to straighten	94
4-6	Cartoon schematic of proposed model of dynein force generation in microtubules	95
5-1	Severed myofilaments in C2C12 myoblasts display a repair mechanism.....	106

LIST OF TERMS

ATP	Adenosine Triphosphate Nucleotide
BCE	Bovine Capillary Endothelial Cells
$C(\tau)$	Autocorrelation function of sarcomere fluctuations
CCD	Charge-Coupled Device
D	Effective diffusion coefficient of sarcomere fluctuations
DBS	Donor Bovine Serum
DMEM	Dulbecco's Modified Eagle Medium
EC	Endothelial Cells
ECM	Extracellular Matrix
EM	Electron Microscopy
EGFP	Enhanced Green Fluorescent Protein
EYFP	Enhanced Yellow Fluorescent Protein
FGF	Fibroblast Growth Factor
F_M	Force generated by myosin molecules
F_S	Force exerted by stiff elastic element in series with myosin molecules
G-Actin	Globular Actin
HEPES	4-(2-hydroxyethyl)-1-piperazineethanesulfonic acid
L_0	Initial length of stress fiber
$L(t)$	Time dependent length of stress fiber
L_{\min}	Minimum length of stress fiber after retraction
MEM	Minimum Essential Medium Eagle
MTOC	Microtubule Organizing Center
NA	Numerical Aperture

$p(x_c)$	Probability distribution of contraction distances
PDMS	Poly(dimethyl)siloxane
PIV	Particle Image Velocimetry
Ptk2	Male Rat Kangaroo Kidney Epithelial Cells
$R(t)$	Relative retraction length
s_1 and s_2	Line segment lengths used for curvature calculation
SF	Stress Fibers
T	Instantaneous stress fiber tension
\bar{T}	Mean stress fiber tension
T_i	Instantaneous tension in i th sarcomere
T_{ext}	External tension in stress fiber
T_{max}	Tension at which contraction stalls
U2OS	Human osteosarcoma cell line
UV	Ultraviolet
V	Linear retraction velocity
v_c	Instantaneous velocity of i th sarcomere
v_d	Drift velocity
v_i	Instantaneous velocity of i th sarcomere
VASP	Vasodilator-Stimulated Phosphoprotein
x_c	Linear contraction distance
$x_{initial}$	Initial sarcomere length
x_{min}	Steady state sarcomere length upon reaching barrier
$x(t)$	Time dependent sarcomere length

Z-lines	Borders that link and separate penultimate muscle sarcomeres
β	Proportionality constant for sarcomere tension-velocity relationship
Δ	Mean contraction distance
δ	Initial contraction distance after release of elastic element
κ	Local curvature of a microtubule
σ	Standard deviation of experimentally observed sarcomere length fluctuations
σ_T^2	Variance of sarcomere tension fluctuations
$\sigma_{T_{ext}}^2$	Variance of external tension fluctuations
σ_v^2	Variance of velocity fluctuations
τ_L	Relaxation time constant of sarcomere length fluctuations
τ_v	Relaxation time constant of sarcomere velocity fluctuations

Abstract of Dissertation Presented to the Graduate School
of the University of Florida in Partial Fulfillment of the
Requirements for the Degree of Doctor of Philosophy

CYTOSKELETAL MECHANICS IN ENDOTHELIAL CELLS

By

Robert John Russell

May 2011

Chair: Tanmay Lele
Cochair: Richard Dickinson
Major: Chemical Engineering

An important function of normal endothelial cells is the ability to sense and transduce applied mechanical forces due to blood flow through the vasculature. Defects in endothelial mechano-sensing result in numerous pathologies including atherosclerosis. The actomyosin and microtubule cytoskeleton gives endothelial cells structural support and the ability to both sense and respond to external forces. This dissertation focuses on how the actomyosin and microtubule cytoskeleton generate and respond to forces in endothelial cells.

Tensile force within endothelial cells is generated in actomyosin stress fibers, which are composed of contractile units called sarcomeres. Using femtosecond laser ablation, we severed living stress fibers and measured sarcomere contraction under zero tension. The time dependent trajectories of contracting sarcomeres suggested three distinct phases: an instantaneous initial response, a sustained change in length at constant velocity and finally a steady state. We proposed a novel model for tension generation in the sarcomere where myosin generated forces in adjacent sarcomeres are directly in balance.

Through live cell imaging we observed that the number of sarcomeres and sarcomere lengths dynamically change in the cell. We show that sarcomere lengths continually fluctuate, new sarcomeres formed at focal adhesions are convected into the stress fiber and that sarcomeres disappear at specific points or “sinks” along the stress fiber. These results show that stress fibers are highly dynamic structures despite their relatively static morphology. Taken together the observation of sarcomere fluctuations and the sarcomere contraction results suggest a model where tension fluctuations determine the distribution of sarcomere lengths.

Microtubules are the stiffest of the cytoskeletal filaments but are consistently observed to exist in bent conformations in living cells and are assumed to be under compression. Individual buckled microtubules were severed using a femtosecond laser to directly determine the nature of the microtubule force balance. Newly formed minus-ended microtubules did not straighten to release bending energy but rather increased in curvature. Interestingly in dynein inhibited cells newly formed minus-ended microtubules were observed to straighten. These results suggest a model where dynein both stabilizes and enhances microtubule buckles. Overall this work considerably advances the understanding of cytoskeletal mechanics in endothelial cells.

CHAPTER 1 INTRODUCTION

Function of the Endothelium

The endothelium serves as a semi-permeable membrane that lines the whole of the vasculature (1). The primary functions of the endothelium are to regulate transport between the blood stream and the surrounding tissues, and provide a smooth boundary condition to reduce turbulent blood flow (1-4). The endothelium is heterogeneous in function depending on the location with varying degrees of permeability (2-4), i.e. extremely low permeability at blood-brain barrier (5) and higher permeability elsewhere (6-8). Interestingly all of this regulation that is crucial for normal physiological function is accomplished with a single layer of specialized endothelial cells. Alterations in the permeability of the vascular endothelium can lead to significant pathologies including acute lung injury, acute respiratory distress syndrome and sepsis (9). Endothelial dysfunction has also been implicated in hypercholesterolemia, atherosclerosis, myocardial ischemia, and chronic heart failure (10). While biochemical signaling pathways have been identified in static cell culture that lead to endothelial dysfunction (11), increasingly the importance of the endothelial cells ability to respond to mechanical stress is being considered (12,13).

The endothelium experiences varying degrees of mechanical stresses depending on the location and function (9). Generally endothelial cells are exposed to shear stress from blood flow and a cyclic wall strain from the compliant vessels undergoing pulsatile blood flow (Figure 1-1 illustrates these external stresses) (13). Endothelial cells in the microvasculature must also resist frequent collisions from red and white blood cells (14). Evidence from both in-situ observations and in-vitro experiments suggest that

endothelial cells dynamically reorient themselves to minimize exposure to stresses (15,16). The mechanisms by which endothelial cells adapt to these applied stresses are not well understood (9). The endothelial cytoskeleton provides structural support and the ability to transduce external mechanical forces. As a result the cytoskeleton plays a crucial role in how endothelial cells respond and adapt to mechanical forces.

Endothelial Cytoskeleton

The endothelial cellular cytoskeleton consists of three distinct subsystems of biopolymer filaments which have varying mechanical properties and functional roles. These subsystems include actin microfilaments, microtubules, and intermediate filaments, visual examples are provided in Figure 2-2. Two of these systems, actin filaments and microtubules, have associated molecular motors that both generate force in these systems and transport cargo.

Actin Cytoskeleton

Actin is a globular protein of approximately 42 kDa found in abundance in all eukaryotic cells (17). The ability of actin to directionally polymerize into helical filaments results in it being a key structural protein for almost all types of cells (18). Actin filaments and their associated proteins such as the motor protein myosin and the cross linking protein α -actinin make up the actin cytoskeleton (19). The actin cytoskeleton has many important physiological functions both at the cellular and tissue level (2). The actin cytoskeleton plays a substantial role in endothelial function including regulating permeability (2). There are generally considered to be three distinct subsections of the actin cytoskeleton in the intact endothelium including the cortical actin rim, the membrane skeleton and actin stress fibers (2). In tissue culture these structures are

similar except the cortical actin rim is replaced by regions of active actin polymerization known as lamellipodia (20).

This document will focus on stress fibers which are force generating and transmitting structures that provide the endothelial cells with structural support and the ability to resist mechanical stresses. Stress fibers have been observed in almost all cell types in tissue culture and appear as continuous cables when stained with actin, (Figure 2-2A) (21). Stress fibers either connect with other stress fibers or terminate at focal adhesions (Figure 2-2A) (22,23). Focal adhesions serve to connect the cell through integrin linkages to the ECM and promote strong adhesion to the basement membrane (24). Furthermore, focal adhesions play both a mechanosensory and signaling role for adhesion dependent cell types (24). While stress fibers and focal adhesions are observed in almost all cell types in tissue culture, stress fibers are observed only in endothelial cells in vivo (25).

Microtubule Cytoskeleton

Microtubules are long tubular biopolymers (Figure 2-2B) that are approximately 25 nm in diameter. In mammalian cells, microtubules generally consist of 13 protofilaments arranged radially around the hollow core (26). Protofilaments are made up of directionally polymerized heterodimers of tubulin consisting of one α -tubulin monomer and one β -tubulin monomer (27). The tubulin heterodimers are arranged such that an alternating pattern of α -tubulin monomers and β -tubulin monomers persists throughout the length of the protofilaments (27). This polarity results in the microtubule as a whole being polarized such that tubulin preferentially adds to one end (referred to as the plus end), over the other end (referred to as the minus end) (26). The depolymerization rate of the plus end is significantly faster than the minus end (28). The plus end of a

microtubule randomly switches from growing to shrinking phases in a process known as dynamic instability (28). Microtubules play critical roles in normal cell functions including the formation of mitotic and meiotic spindles, stabilization of protrusions, and polarization of cells (29). The directionally persistent molecular motors dynein (minus end directed) and kinesin (plus end directed) are responsible for the transport of organelles and proteins (29). In mammalian cells it has been established that most microtubules emanate from a central microtubule organizing center, MTOC, or the centrosome (29,30). At the MTOC, minus ends of the microtubule are both nucleated and stabilized resulting in a star-shaped radial array of microtubules (Figure 2-2B) (30)

Evidence for Stress Fibers in the Intact Endothelium

There have been numerous studies that have reported the presence of stress fibers in the intact endothelium and have investigated the conditions under which they form (25,31,32). Herman and coworkers published evidence and novel observations of stress fibers in vascular endothelial cells in vertebrate tissues in 1982 (25). Using fluorescence microscopy of fluorescently tagged phalloidin, anti-myosin antibodies and anti- α -actinin the authors searched for actin stress fibers in a variety of vertebrate tissues. Ultimately stress fiber like structures were found only in the vascular endothelial cells of cows, chickens, dogs, rats and a cat. Specifically in regions of the vasculature subjected to high velocity and turbulent blood flow, stress fibers were confirmed to show a punctate staining for myosin and α -actinin and were oriented parallel with the flow direction. The authors make some astute comments about the possible role stress fibers play physiologically including the factors that may govern their formation. The authors suggest that stress fibers likely transmit forces to the basement membrane and that hemodynamic forces may be responsible for the formation of stress fibers (25).

Physiological factors influencing expression of stress fibers in vascular endothelial cells were investigated by Fujiwara and coworkers in 1986 (31). Their investigation confirmed the existence of axially oriented stress fibers in vascular endothelial cells specifically mouse and rat thoracic aorta. They reported an increase in stress fiber expression in male rats versus female rats and in same-sex normotensive versus spontaneous hypertensive rats. These findings are consistent with the hypothesis that increased hemodynamic forces (male rats generally have higher blood pressure) result in the expression of stress fibers in vascular endothelial cells (31).

Drenckhahn and Wagner investigated in-situ stress fibers in splenic sinus (a channel of endothelial cells with increased permeability to allow the selective passage of red and white blood cells) endothelial cells (32). This study was one of the first to demonstrate the in situ existence of stress fibers in endothelial cells outside of the large vessel vasculature. The authors established with electron microscopy that the molecular structure of stress fibers from isolated in situ endothelial cells matches that of cultured EC in that they displayed regions of alternating polarity actin filaments separated with myosin fragments. Using immunohistochemistry the authors observed that fluorescently labeled antibodies to actin, myosin, tropomyosin and α -actinin localize strongly to the stress fibers while extracellular matrix proteins (laminin, fibronectin and collagen) were localized to the periphery of the cells. Furthermore the authors demonstrated that stress fibers are contractile in the presence of ATP and Mg^{2+} in permeabilized cells (32).

Further evidence that hemodynamic forces modulate the expression of EC stress fibers was presented by Gotlieb and coworkers through examination of *in situ* rabbit aorta bifurcations (33). Prior to bifurcations, actin localized in EC to two distinct

structures, a peripheral actin and ring and variable numbers of stress fibers. Along the divider wall, ECs exhibited more of the stress fiber phenotype and less peripheral actin and with increasing distance from the bifurcation reverted to an even distribution in peripheral and stress fiber actin. Kim et al. showed that increased hemodynamic forces caused an increased expression of stress fibers in an excised rabbit mid-abdominal aorta (34). Briefly, the authors altered the flow fields by surgically constricting flow in the mid-abdominal aorta. In non-constricted vessels as well as prior to the constriction actin was distributed into a peripheral ring and in a variable numbers of stress fibers. Immediately after the constriction some EC cells lost directionality and all cells displayed actin stress fibers. Further (3-13 mm) from the constriction point cells recovered their directionality but still expressed stress fibers (34).

While most studies initially reported the expression of stress fibers in large arteries and heart chambers, Nehls and Drenckhahm reported the first evidence of stress fibers in microvascular endothelial cells (14). Their results suggest that stress fibers exist at all levels of the microvasculature including capillaries and venules (feeders to main vein) and hypothesize that microvascular endothelial stress fibers may protect the cells from shear stress and collisions of red and white blood cells (14).

Microstructure of Endothelial Stress Fibers

Stress fibers are contractile cables that display a continuous staining for actin until their ultimate termination into focal adhesions, see example in Figure 2-2A (35). There has been significant work done in the past to understand the microstructure of stress fibers from a variety of cells types (36-39). While some conflicting results have been reported between motile and non-motile cell types, the general findings for non-motile cells hold true for the endothelial cells discussed in this document (40). The cross-

linking protein α -actinin is responsible for bundling the 10-30 parallel actin filaments (40) that make up the fiber together. Interestingly it was found through immunohistochemistry that anti- α -actinin antibodies localize to stress fibers in a punctate pattern as illustrated in Figure 2-3 (37). These punctate spots were originally referred to in the literature as dense bodies (Figure 2-3 contains schematic) as they appeared as electron dense regions similar to muscle Z-lines (35). Further studies have identified multiple other proteins that localize to stress fiber dense bodies including filamin (41), fascin (42), and VASP (43). Staining for myosin or tropomyosin reveals a punctate pattern that is offset from the dense bodies (36,38,44). These findings led to the hypothesis that stress fibers were composed of contractile subunits analogous to muscle sarcomeres.

The idealized sarcomeric model of the stress fiber is such that each dense body serves as the boundary between adjacent sarcomeres (Figure 2-3 contains a schematic described below) (36). A single sarcomere consists of opposite polarity actin filaments emanating inwards from the respective dense bodies where the barbed ends are located (45). Bipolar myosin filaments cross-link the opposing bundles of actin filaments (44). Contractile force is generated as the bipolar myosin filaments translocate in opposite directions towards the dense bodies. There exists significant experimental evidence that the idealized sarcomere structure is in fact realized in stress fibers of non-motile cells but maybe more complicated for some stress fibers in motile cells (40,45).

Kries and Birchmeier initially reported that stress fiber sarcomeres are contractile in cultured fibroblasts suggesting that a sliding filament mechanism must be present (46). A key requirement of the sliding filament mechanism is the alternating polarity of

actin filaments. Cramer et al. conducted an electron microscopy study of actin filament orientation in both motile fibroblasts and non-motile PtK2 cells (40). While an earlier study had reported alternating actin polarity from EM studies of PtK2 cell stress fibers (47), this study demonstrated that actin polarity alternated as a function of length with an average period of 0.6 μm (40). Stress fibers in motile cells were reported to contain a more complicated arrangement of actin filaments including both graded and uniform polarities. While this was certainly an interesting finding, stress fibers in motile cells are beyond the scope of this document (40). Actin filaments are dynamic in that there is directional turnover (assembly at plus ends and disassembly at minus ends) of actin subunits with the unpolymerized pool of G-actin. Dense bodies are locations of actin polymerization as demonstrated by imaging the stress fiber immediately after microinjection of labeled rhodamine actin (45). This finding is consistent with the sarcomeric model, which requires that the plus ends to be located in the dense bodies, in order for the directional myosin motor to function.

Mechanics and Dynamics of Stress Fibers

There has been considerable interest in understanding the mechanical properties of stress fibers due to their importance in normal endothelial function. Until recently studying mechanics of stress fibers in living cells was difficult, with earlier work done in permeabilized cells or with isolated stress fibers (21,48). The first evidence of the possibility of contractile stress fibers was in permeabilized systems containing stress fibers and cortical actin where a change in cellular shape was observed upon addition of Mg^{2+} and ATP (46). As this study could not rule out the possibility of other cortical actin being responsible for the observed contraction, Katoh et al. showed that isolated single stress fibers were indeed contractile when treated with Mg-ATP solution (21). When the

contracted fibers were washed of the Mg-ATP solution no relaxation or lengthening of the fiber was observed over the time course of 20 minutes (21). The authors also reported that treatment of isolated stress fibers with the myosin light chain kinase inhibitor KT5926 were not contractile in the Mg-ATP solution, suggesting that the stress fiber contraction is a myosin driven phenomenon (21).

With the advent of transfectable fluorescent protein fusions, the ability to study stress fibers in living cells became a reality. In a recent paper Kumar et al. demonstrated for the first time that stress fibers are contractile in living cells (49). Stress fibers labeled with EYFP-actin in bovine capillary endothelial cells were severed using a femtosecond laser nanoscissor. The authors demonstrated that the observed retraction of cut fiber ends resulted from fiber shortening by cutting before branch points and photobleaching fiduciary markers in the fiber. The authors found that the gap between retracting ends of the fiber followed exponential kinetics as would be expected by the severing of a stretched viscoelastic cable. Thus the characteristic time constant of the recoil would correspond to the ratio of the damping coefficient to the Young's modulus. The recoil of severed stress fibers was partially inhibited when cells were treated with the rho-associated protein kinase inhibitor Y27632 and was completely abolished with treatment with myosin light chain kinase inhibitor ML7. In summary this work was significant in that it clearly demonstrated the stress fibers are contractile in living cells and that stress fiber force generation is myosin dependent (49). Yin and coworkers used atomic force microscopy to probe the mechanics of stress fibers in living cells and found that myosin plays an integral role in determining the apparent stiffness of the stress fiber (50). Stress fibers with decreased contractility, cells treated the myosin ATPase

inhibitor blebbistatin, had decreased stiffness while fibers with increased contractility, cells treated with the serine/threonine phosphatase inhibitor calyculin A, had an increase in stiffness (50). While these studies provided important insight into the mechanics of stress fibers in living cells they did not provide detail into the mechanics of individual stress fiber sarcomeres.

Peterson and coworkers showed that cells treated with calyculin A, a serine/threonine phosphatase inhibitor, displayed both contraction and expansion of sarcomeres within the same stress fibers (51), a result that prompted explanations based on theoretical mechanical models of stress fiber sarcomeres (52,53). In the work by Peterson and coworkers, EGFP labeled α -actinin and myosin II regulatory myosin light chain transfected fibroblasts and fibroma cells were treated with calyculin A which resulted in overall stress fiber shortening (51). The author reported that while sarcomeres at periphery shorted upon calyculin A treatment, central sarcomeres lengthened (51).

Sarcomere Mechanics Models

Two theoretical modeling studies were published to explain the inhomogeneous behavior of stress fibers reported by Peterson and coworkers (51). Besser and Schwarz proposed a mechanical model of the sarcomere consisting of an active force generating myosin element in parallel with both an elastic and viscous element (52). This study included a biochemical feedback loop for myosin activation from force induced signaling in focal adhesions. Stachowiak and O'Shaughnessy published a similar sarcomere model that also included an elastic element in series with active myosin force generation but excluded the viscous element (53). A complication was added to this model in that a repulsive force of overlapping filaments was also included. While these

studies were novel attempts to model the stress fiber as sarcomeric units in series, there is limited experimental evidence to support these mechanical models.

Mechanics of Microtubules

Because of their hollow geometry, microtubules are approximately 100 times stiffer than either actin filaments or intermediate filaments (54,55). Microtubules have been established to generate pushing forces as a result of their directional polymerization (56). Despite a thermal persistent length in the millimeter range, microtubules have been widely observed and documented to exist in bent shapes in cultured cells (29,55) see Figure 2-4A . Thus these buckled microtubules have been widely assumed to be under compressive loading. Polymerizing microtubules have been shown to buckle upon impinging on an immovable boundary in in-vitro studies (56) and in-vivo experiments (55), see Figure 2-4B. It has been hypothesized that microtubules play the role of 'struts' in the cell that can balance the tensional forces generated by acto-myosin systems (57-59). An issue with this hypothesis is that microtubules reach significant lengths in cells which cannot support the large forces generated. An opposing viewpoint is that microtubules do not play a structural role in interphase animal cells but only serve as a 'highway' for intracellular trafficking. Recently there has been increasing interest in determining the cause for the bent shapes of microtubules (29,55,60) .

Microtubules have been hypothesized to bend due to polymerization of a microtubule against an immovable boundary (55,56), actomyosin contractility (61,62) , and microtubule based motors interacting with cortical actin (63-67). Recently Weitz and coworkers proposed that buckled microtubules could support larger compressive loads if they were laterally supported by an elastic medium (55). Their findings suggest that

single microtubules buckle with shorter wavelengths than expected for classic Euler buckling under a compressive load. Their conclusion was that single microtubules supported by an elastic matrix would be able to support significantly larger compressive loads and exhibit the observed short wavelength buckles (55).

Another study investigated the mechanism involved in microtubule buckling through direct observation of buckling microtubules in living cells (29). By performing fluorescence speckle microscopy Odde and coworkers found that buckling microtubules move in the direction of the cell periphery, instead of towards the cell center which would be suggestive of polymerization driven buckling. Furthermore the authors found that the F-actin surrounding buckling microtubules was stationary which suggests that the actomyosin activity or actin retrograde flow do not play a substantial role in buckling microtubules. The authors hypothesized that the anterograde-driven buckling is indicative of microtubule based molecular motors (29). While this paper provides evidence that microtubule based motors are responsible for buckling it is still unclear which motor is involved and the mechanism by which the motor acts to buckle microtubules.

Organization of this Document

The endothelial cytoskeleton plays a crucial role in normal cell function but fundamental questions remain about how ensembles of molecular motors generate forces in both actomyosin and microtubule cytoskeleton. This dissertation focuses on how the actomyosin and microtubule cytoskeleton generate and respond to forces in endothelial cells. In Chapter 2, a novel technique of femtosecond laser ablation is applied to study the mechanics of stress fiber sarcomeres in Bovine Capillary Endothelial Cells. A novel mechanical model for the stress fiber sarcomere is proposed

and the implications of this model on the overall behavior of stress fibers are discussed. In Chapter 3 novel observations of the dynamics of stress fiber sarcomeres are reported and these observations are discussed in the terms of the model proposed in Chapter 2. In Chapter 4 the dynamics of severed microtubules and the role of dynein in stabilizing and enhancing microtubule buckles will be discussed. In Chapter 5 the results from this document are summarized and future work is proposed to continue this study.

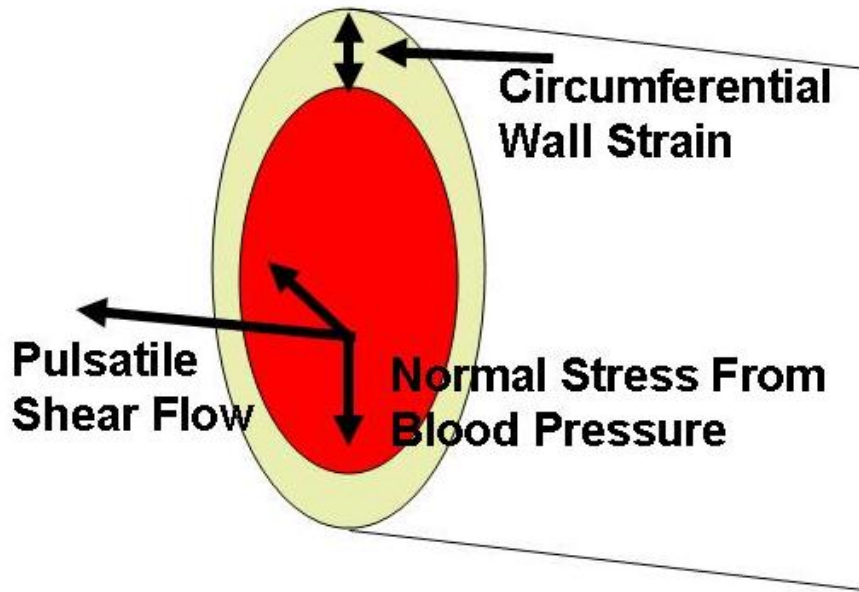


Figure 1-1. Schematic of forces exerted on the endothelium in the vasculature. Pressure driven blood flow results in shear stress and a normal force against the endothelium. The compliant vasculature undergoes cyclical circumferential wall strain as result of the pulsatile contractions of the heart.

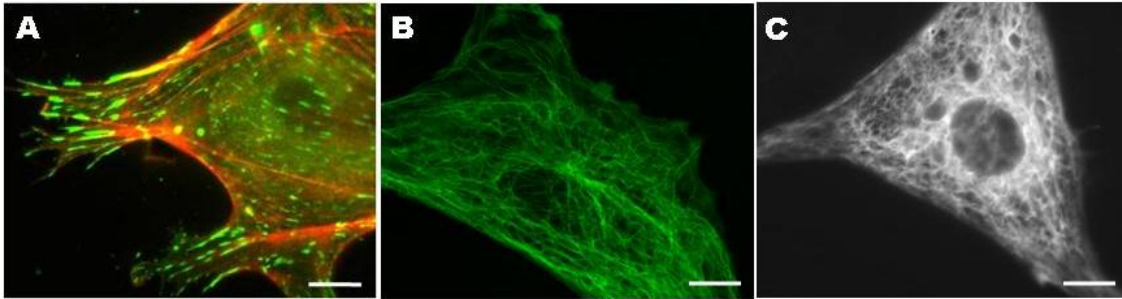


Figure 1-2. Elements of the cellular cytoskeleton. (A) Micrograph of BCE cell stained with phalloidin for actin stress fibers (red) and immunostained for vinculin (green) in focal adhesions. (B) Micrograph of BCE cell infected with adenoviral EGFP- α -tubulin displaying microtubules emanating from the centrosome. (C) Micrograph of BCE cell transfected with EGFP-vimentin to visualize the intermediate filament network. Scale Bars 20 μ m

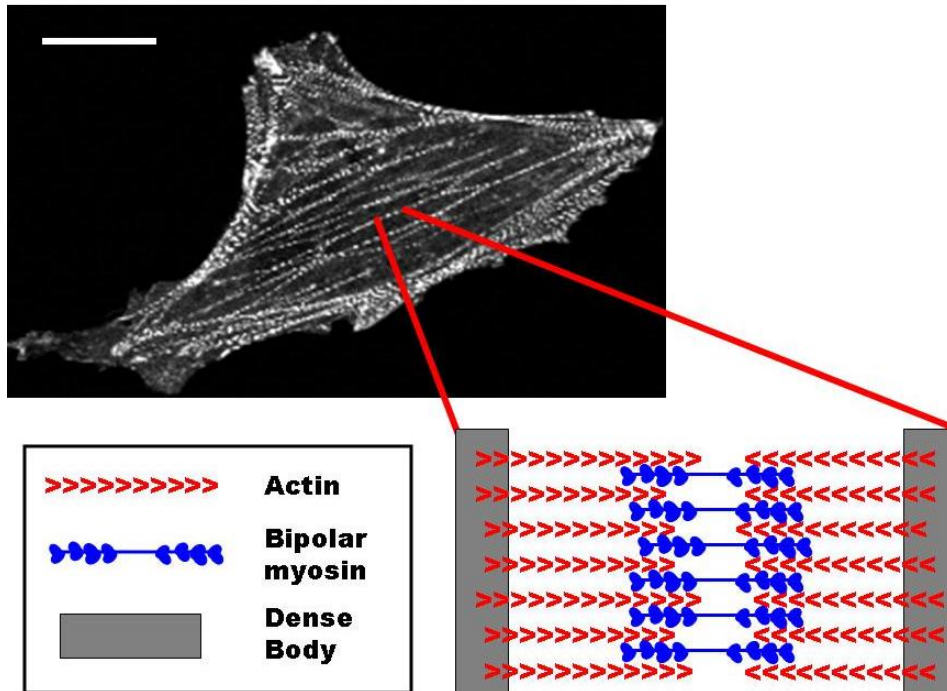


Figure 1-3. Microstructure of stress fibers consists of sarcomeric subunits. A micrograph of BCE cell transfected with EGFP- α -actinin which results in a punctate staining of dense bodies. The cartoon schematic illustrates the microstructure of a single stress fiber sarcomere which marked by two penultimate dense bodies. Scale bar 20 μ m

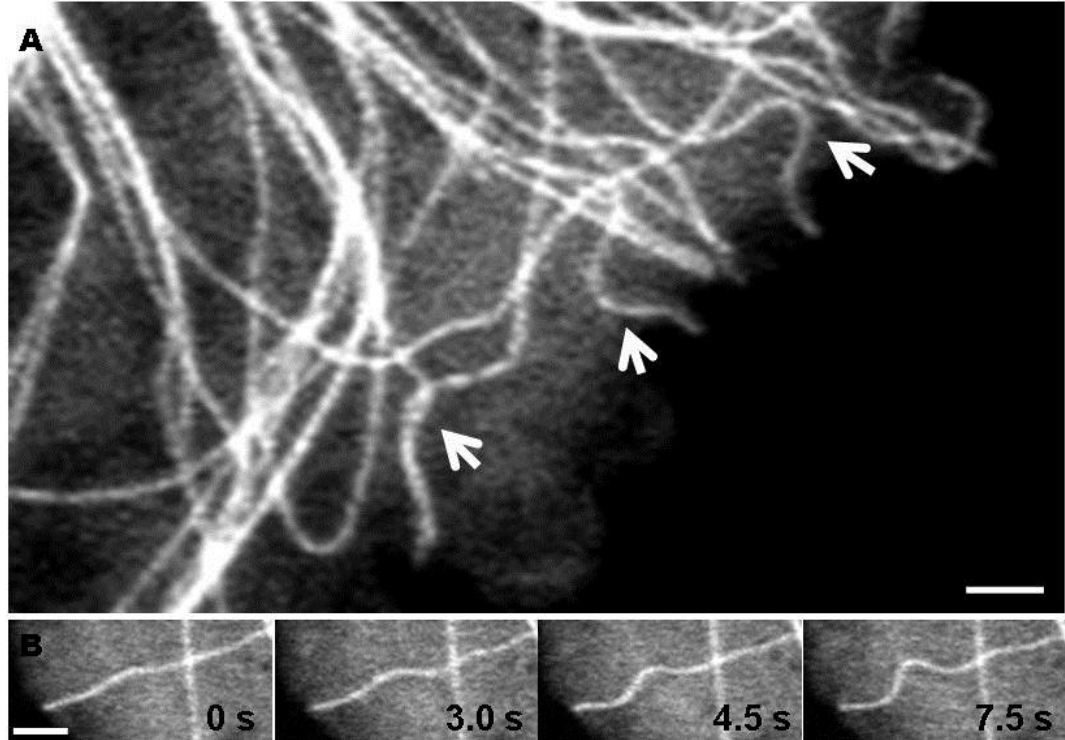


Figure 1-4. Microtubules exhibit short wavelength buckling at the cell periphery. (A) Microtubules buckle with short wavelengths ($\sim 2\text{-}3\ \mu\text{m}$) at the periphery. (B) Time series of a single microtubule as it contacts the periphery and undergoes buckling. Scale bars are $2\ \mu\text{m}$.

CHAPTER 2 SARCOMERE MECHANICS IN CAPILLARY ENDOTHELIAL CELLS

Tension generation inside cells and its transmission to the extracellular matrix at cell-matrix adhesions enables cells to adhere, spread, migrate and maintain tissue form. Tension is generated in vascular endothelial cells by actomyosin stress fibers. While stress fibers are observed in many cell types cultured in vitro, stress fibers in vivo are observed in endothelium of intact tissues such as the aorta (25), the spleen (32) and the eye (68). Tension in stress fibers promotes strong adhesion between endothelial cells and the basement membrane (32). This adhesion allows endothelial cells to resist blood flow-induced mechanical stresses including cyclic strain, hydrostatic pressure and shear flow (25,32,68-71). Endothelial cells respond to applied mechanical stresses by changing their orientation both in tissue (69,70) and culture (71-74), which depends on remodeling of stress fibers (71). Thus stress fibers are necessary for resisting and sensing mechanical stresses in vascular endothelial cells. Stress fiber tension is also greatly altered in tumor endothelial cells which have aberrant response to mechanical stresses (75). Stress fiber tension is implicated in abnormal endothelial response to altered hemodynamic forces that cause atherosclerotic plaques at vascular bifurcations (76). Owing to their key importance as a contractile structure that enables normal endothelial cell function, there is considerable recent interest in understanding the mechanical properties of stress fibers (48,49,52,53). However, it has remained a fundamental challenge to measure these properties in the context of a living, functioning cell.

Stress fibers are composed of repeating units termed sarcomeres after the analogous muscle structures (36-38,47,77,78). Using electron microscopy, Mitchison

and co-workers confirmed the sarcomeric microstructure of stress fibers in non-motile PtK2 cells by showing that they contain actin filaments of alternating polarity along the entire length of the fiber (40). Tension is generated in the sarcomere by walking of bipolar myosin heads in opposite directions, resulting in contraction of the sarcomere ((32,46,79) and see Figure 2-1A for a schematic). Neighboring sarcomeres are connected by dense bodies containing α -actinin, filamin and VASP (Figure 2-1B). Physical coupling between stress fibers and focal adhesions allows transfer of the tension to the substrate (80).

Recently proposed mechanical models for stress fiber sarcomeres (52,53) assume that velocity-dependent myosin contraction operates in parallel with an elastic element, analogous to the Kelvin-Voigt model (spring-and-dashpot in parallel) for viscoelasticity. A feature of these models is that expanded or compressed elastic elements partially balance the tension and account for the distribution of sarcomere sizes (52,53). These mechanical models have been used to explain the experimental observation of Peterson et. al (51) that sarcomeres contract near focal adhesions on activation of myosin light chain kinase (52,53). However, to date no direct experimental evidence has been offered to test current mechanical models of SF sarcomeres.

While the majority of experimental data on stress fiber mechanics is from in vitro experiments of extracted stress fibers (21,48), a recent study used a femtosecond laser to sever individual stress fibers allowing the first in vivo measurements of stress fiber mechanics (49). Cutting the fiber caused the severed ends to retract (see Figure 2-1C for an example). The retraction of the fiber exhibited an exponential relaxation characteristic of that following tension loss in a Kelvin-Voigt element (49), with a

relaxation time constant of ~6 seconds. Myosin inhibition completely eliminated retraction in severed stress fibers (49). While this work pioneered a new approach to measure mechanics of stress fibers in living cells, it did not provide a mechanistic explanation for the observed mechanical response. For example, the molecular origin of the apparent viscosity of the fiber is unknown, and it is unclear whether the observed lack of retraction under myosin inhibition can be explained by existing sarcomere models. To explain this viscoelastic retraction of the severed ends, a recent model represented the stress fiber as a tensegrity structure containing tensed and compressed elements (81). However, this model did not involve a sarcomeric description of the stress fiber.

We used femtosecond ablation to sever individual fibers and directly measured sarcomere contraction by tracking the position of α -actinin labeled dense bodies in the severed fiber. The lengths of individual sarcomeres decreased in two phases: an instantaneous initial decrease, followed by a linear contraction at constant speed. The latter phase, interpreted as active myosin-mediated contraction, ceased abruptly after a minimum sarcomere length was achieved. The linear response suggests that there is no increase in resisting force (for example, due to a spring element) during contraction. In addition, subsequent inhibition of myosin following severing and contraction yielded no elastic recovery, suggesting that elastic potential energy is not stored in the contracted fiber. Together, these observations argue against models that have elastic elements in parallel with myosin contractile elements. Based on these findings, we propose a new and simpler mechanical model for the sarcomere in which stress fiber tension is determined only by myosin contraction in series with a stiff elastic element. The

fundamental difference between this model and previous models is that all tension in the stationary stress fiber is borne entirely by the myosin contractile elements in each sarcomere, with no apparent elastic element existing in parallel with the myosin contractile element.

Materials and Methods

Cell Culture and Transfection

Bovine capillary endothelial (BCE) cells were used at passages 11-14 and were maintained at 37°C in humidified 10% CO₂. The BCE cells were cultured on tissue culture dishes in complete medium consisting of low-glucose Dulbecco's modified Eagle's medium (DMEM; Mediatech, Manassas, VA) supplemented with 10% donor bovine serum (Gibco), 1% 1M HEPES (Mediatech) and glutamine (0.292 mg/ml)/ penicillin (100 U/ml)/ streptomycin (100 g/ml) (Sigma). The growth media was supplemented with 1 µl of basic FGF (final concentration 2 ng/ml; Sigma) per 1 ml of media. This culture method was described previously in (82). For experiments cells were transiently transfected with EGFP- α -actinin plasmid (kindly provided by Prof. Carol Otey) or EGFP-actin using the Effectene (Qiagen, Valencia, CA) reagent. Previous studies have shown that the fusion construct is functional and localizes with the endogenous protein (83).

Transfections were done approximately 2 full days before any planned microscopy experiments. Cells were transfected for 6 hours in a 12 well cell culture dish using the Effectene transfection kit. For transfections 1-2 µg of plasmid DNA was found to be sufficient for both the EGFP- α -actinin and EFGP actin plasmids. The manufacturer supplied protocol was optimized and used for all transfections. After 24 hours the cells

were trypsinized (Gibco) and plated sparsely on glass bottom dishes (MatTek, Ashland, TX).

For imaging experiments the media was changed to a CO₂-independent media as described previously (84). Briefly the CO₂-independent imaging medium (pH 7.3) was prepared by dissolving Hanks balanced salts, which are phenol-red and bicarbonate free, in 1000 ml of DD H₂O. The following supplements were added; HEPES (20.0mM), 1% bovine serum albumin, and MEM essential and nonessential amino acids (Sigma). Imaging media was prepared by adding 10% DBS and glutamine (0.292 mg/ml)/ penicillin (100 U/ml)/ streptomycin (100 g/ml) (Sigma)

Laser Ablation of Stress Fibers

For laser ablation experiments, an inverted Zeiss Axiovert 200M laser scanning confocal microscope (LSM 510 NLO, Thornwood, NY) was used with 63X, 1.4-NA Plan-Approchromatic oil immersion lens (Zeiss). In order to image EGFP- α -actinin, the 488 nm laser line with the power attenuated to 5-10% and the appropriate EGFP bandpass filter was used. Single stress fiber ablation was done with a Ti:Sapphire laser at 50-100% transmission (Chameleon XR, Coherent, Santa Clara, CA) as previously described (49). The Ti:Sapphire laser was focused through the objective and scanned a thin, \sim 0.14 μ m, rectangle orthogonally crossing the width of the stress fiber for 1-7 iterations. A wavelength of 790 nm was used with a laser-head power of 1.5 W, pulse duration of 140 fs and repetition rate of 90 MHz. After ablation confocal scans as described previously were collected using Zeiss LSM 510 4.2 software at 100-1000 ms/frame to capture the kinetics of sarcomere contraction. A cartoon schematic of the microscope used for the ablation and imaging is included in Figure 2-2. Detailed methods used for ablation of single stress fibers follow in the next paragraph.

Once cells were placed on the microscope and the correct focal plane was found the laser parameters for cutting were optimized. The separate lasers that were used for ablation and imaging must be aligned correctly to focus on the exact same position in the z-direction for optimal cutting. Changes in the alignment resulted in slightly different laser parameters being needed for optimal ablation from day to day. Before experiments were conducted a cell expressing clear stress fibers was found and used to test laser parameters for cutting. The FRAP module included with the Zeiss microscope software was used to conduct ablation by scanning with the Ti:Sapphire laser at 790 nm. To optimize laser parameters the laser was initially set at 100% transmission power and to scan for one iteration. These conditions were tested by ablating a single fiber. In the case where a fiber was cut and no collateral damage was observed in the DIC image then experiments were continued using these settings. When collateral damage was observed the laser power was reduced incrementally by 10 % until a clean cut occurred. If the fiber would not cut at 100% transmission, multiple scanning iterations were used. No more than approximately 7 scans were used because the cutting scans took too long which resulted in unacceptable time resolution. In the case where it was not possible to sever the stress fiber with multiple iterations, the 488 nm Argon and the Ti:Sapphire lasers were realigned. To realign the lasers, a cell was focused using the 488 nm laser and then the imaging conditions were switched to image the cell using the Ti:Sapphire laser at 790 nm. The vertical position of the Ti:Sapphire laser was slowly adjusted until the cell came into focus.

For myosin inhibition, BCE cells were treated with 50 μ M blebbistatin for ~30 minutes after stress fibers were severed and allowed to reach steady state. Confocal

images were taken to determine if stress fibers were able to lengthen or relax after myosin poisoning. For all blebbistatin experiments, exposure to the 488 nm laser was minimized to prevent photoinactivation or phototoxicity.

Image Correlation Based Tracking of Dense Bodies

To measure the change in length of the sarcomeres during stress fiber retraction an image correlation based tracking method was developed in MATLAB 7.2 (The MathWorks, Natick, MA). This method was used to determine the positions of GFP- α -actinin labeled dense bodies to sub-pixel accuracy. Image sequences from the Zeiss software were exported to ImageJ (NIH) for image processing, images were rotated to make the stress fibers horizontal and then smoothed to remove noise. MATLAB was used for contrast stretching (MATLAB function `strelim`) on the image sequences before analysis. The commented MATLAB code for tracking single dense bodies is provided in Appendices A.1 and A.2.

The image correlation based method works as described previously in references (85,86). Briefly, a kernel was chosen containing the GFP- α -actinin labeled dense body from the image at time t which was used for a correlation calculation (MATLAB function `normxcorr2`) with an image at time $t+\Delta t$. The relative spatial offset between images t and $t+\Delta t$ was then calculated from the peak position of the correlation matrix. A paraboloid was fit to the correlation function around the peak in order to achieve sub-pixel accuracy for the offset. In order to assign positions to the feature through time, an intensity weighted centroid calculation was done on the first frame to provide initial conditions to be updated by offsets from the correlation calculations. To minimize any error due to changes in the dense body shape, averaged positions were found by correlating each

image with every other image and averaging the result. Tracking a simulated particle indicated that the error was minimal, less than 1%, for the spatial offsets.

As mentioned above, programs were used to track individual dense bodies in severed stress fibers. These programs were semi-automated and required selection of the dense body in the initial frame but then tracked the feature through specified number of frames. Images were prepared for analysis in ImageJ as mentioned above by first cropping out a single stress fiber and then rotating it until it was aligned horizontally. The Dense Body Tracking program provided in Appendix A.1 was run first on the data to get initial position estimates for the dense body in all frames. To run this program, a single dense body was selected by drawing a rectangle around it with the mouse. The program then used this template to track the movement of the dense body through the time series. The initial tracking program prepared a series of images where the surrounding area of the tracked dense body is blacked out.

The Averaging Position Software provided in Appendix A.2 was then run on the modified image series to get accurate position estimates. To run this code the dense body must again be selected by drawing a rectangle with the mouse. The output of this code was the final averaged coordinates for the position of the dense body at each time points. The output was saved for later reference and directions on how to save the data generated were commented into the code in Appendix A.2. After one dense body was run through both programs, neighboring dense bodies were then analyzed and the results were saved for each.

After multiple dense bodies were analyzed (between 2-5) the sarcomere trajectories with respect to time were found using the code provided in Appendix A.3.

This code provided both a composite image of all dense bodies labeled and the time-dependent lengths of all the sarcomeres. The composite image generated by this program allowed the user to check the fidelity of the tracking of each dense body. If at this step the tracking of one dense body was found to jump to a neighbor for one or multiple time frames then that dense body was reanalyzed.

Parameter Estimation for Sarcomere Model

The sarcomere lengths measured during contraction were fit with the four parameter model by minimizing the sum of the square of the residuals (MATLAB function `fminsearch`) to estimate the parameter set, $\underline{p} \equiv [\delta \quad x_{\min} \quad x_c \quad V]^T$. The code used for fitting the four parameter model is provided in Appendix A.4.1. In the case where no sustained linear decrease in length was observed and a line could not be fit, a two parameter model was fit to the data with parameter set, $\underline{p} \equiv [\delta \quad x_{\min}]^T$. The code used for fitting the four parameter model is provided in Appendix A.4.2. In order to determine the uncertainty and correlation in the parameter estimates, the variance-covariance matrix was found for each data set.

To calculate the variance-covariance matrix, the $n \times 4$ Jacobian matrix, \underline{F} was constructed where $F_{i,j} \equiv \partial x(t_i) / \partial p_j$. This was used to calculate the variance-covariance of the parameters according to this formula:

$$\underline{\underline{C}}_p = \left(\frac{1}{n-4} \sum_{i=1}^n \varepsilon_i^2 \right) [\underline{\underline{F}}^T \underline{\underline{F}}]^{-1} \quad (2-1)$$

where $\varepsilon_i \equiv y_i - x(t_i)$ are the residuals. The parameter variances, s_i , lie along the diagonal of $\underline{\underline{C}}_p$ and were used to calculate a weighted mean and standard deviation:

$$\hat{p} = \sum_{i=1}^n w_i p_i \quad (2-2)$$

$$\sqrt{s^2} = \sqrt{\frac{\sum_{i=1}^n w_i (\bar{x}_j - \hat{x})^2}{1 - \sum_{j=1}^n w_j^2}} \quad (2-3)$$

where the weighting factor was calculated using the parameter variances

calculated from Eq. 2-1 and the form $w_i = \frac{1/s_i^2}{\sum_{j=1}^n 1/s_j^2}$.

Results and Discussion

Sarcomeres Contract in the Severed Stress Fiber

To measure sarcomere contraction in living BCEs, we expressed GFP- α -actinin, which labels stress fibers at junctions of neighboring sarcomeres (Figure 2-1B). Next, we severed individual stress fibers in living cells using a recently developed femtosecond laser ablation technique (49). A key feature of femtosecond laser ablation is that it minimizes collateral damage outside the ablated spot (34). On severing a stress fiber, individual sarcomere units in the fiber contracted (kymograph in Figure 2-1C). The severed end appeared to retract exponentially with time (Figure 2-1D), consistent with a previous study by Kumar et al. (49). Thus, the net retraction of the severed edge corresponded to the contractions of individual sarcomeres as measured by the distance between α -actinin-labeled dense bodies.

Although the severed edge of the cut fiber appeared to retract exponentially, the contraction of individual sarcomeres was quite variable but shared qualitatively similar

non-exponential behavior. As shown in Figure 2-3A, the contraction of individual sarcomeres from their initial length, $x_{initial}$, to their final contracted length, x_{min} , occurred in two distinct phases. First, a nearly-instantaneous contraction occurred of distance, $\delta \sim 0.1 \mu\text{m}$, which was followed by a slower contraction over a variable distance of $x_c \sim 0 - 0.4 \mu\text{m}$ at nearly-constant speed. After the linear phase, the contraction ceased abruptly and the sarcomere remained constant at the final length, x_{min} , for the duration of the experiment. Noting this consistent behavior, all sarcomere contraction trajectories were fit by least squares regression to the following piecewise linear model,

$$x(t) = \begin{cases} x_{min} + x_c + \delta \equiv x_{initial} & \text{for } t = 0 \\ x_{min} + x_c - Vt & \text{for } 0 < t < x_c / V \\ x_{min} & \text{for } t \geq x_c / V \end{cases} \quad (2-4)$$

The fit allowed us to estimate the sarcomere contraction parameters V , δ , x_c and x_{min} . The characteristic time for the transition from linear contraction to steady state was calculated as x_c / V . For all analyzed sarcomeres from different stress fibers, normalized contraction $(x - x_{min}) / x_c$ was plotted against Vt / x_c excluding initial sarcomere lengths, (Figure 2-3B). As seen in Figure 2-3B, there is a clear linear trend followed by a stationary non-contracting phase in the pooled, normalized contraction data.

The initial and final lengths ($x_{initial}$ and x_{min} , respectively) were approximately Gaussian distributions, with means and standard deviations, $1.21 \mu\text{m} \pm 0.31 \mu\text{m}$ and $0.97 \mu\text{m} \pm 0.32 \mu\text{m}$ respectively. Shown in Figure 2-4 are the distributions of contraction distances. The distribution of the initial contraction distance, δ , was approximately

symmetric with a mean and standard deviation of $0.085 \mu\text{m} \pm 0.059 \mu\text{m}$ (Figure 2-4A). The linear contraction distance was approximately exponentially distributed, with mean and standard deviation of $0.19 \mu\text{m} \pm 0.087 \mu\text{m}$ (Figure 2-4B). The net contraction had a mean and standard deviation of $0.28 \mu\text{m} \pm 0.11 \mu\text{m}$. (Figure 2-4C). For sarcomeres with a significant linear contraction regime, ($x_c > 0.1$), the fit to Eq. 1 yielded the velocity V of the slower contraction phase. The mean and standard deviation of the contraction velocities was found to be $0.0099 \mu\text{m}/\text{sec} \pm 0.010 \mu\text{m}/\text{sec}$.

Potential Energy is not Stored in Severed Stress Fibers

To confirm that stress fiber retraction is myosin dependent, we severed stress fibers in cells pre-treated with blebbistatin for 30 minutes. As shown in Figure 2-5A, stress fibers in cells treated with blebbistatin retracted insignificantly compared to non-treated cells (see Figure 2-5B). This confirms the results of as reported by Kumar et. al. (49) that retraction in the severed fiber is myosin dependent.

To determine the extent to which the sarcomere contraction could be reversed, we quantified recovery of sarcomere length upon inhibition of myosin. Stress fibers were severed and sarcomeres were allowed to contract to a new steady state. Next, myosin activity was poisoned by treatment with blebbistatin (Figure 2-5B and 2-6) or ML7 (Figure 2-7). The severed fiber length was determined after myosin inhibition and compared with the severed fiber length before inhibition. As seen in Figure 2-5B, there was no visible lengthening of the contracted stress fiber several minutes time after blebbistatin treatment (see Figure 2-6 for another example). This result was confirmed when cells were treated with the myosin light chain kinase inhibitor ML7 (see Figure 2-7). These results show that there is no elastic energy stored in contracted sarcomeres

which can be recovered upon inhibition of myosin contraction. This finding argues against the presence of an elastic element in parallel with myosin force generation. This finding is also in agreement with the results of Katoh et al. (21) who showed that isolated stress fibers cannot relax after contracting in a myosin dependent fashion.

A Mechanical Model for the Sarcomere

The behavior of contracting sarcomeres following loss of tension, i.e. a near-instantaneous initial retraction followed by slower linear contraction until a minimum length is reached can be explained with the simple mechanical model shown in Figure 2-8. In this model, an elastic element is in series with a myosin contractile element. Following severing, the sarcomere initially relaxes elastically, followed by slower myosin-mediated contraction at a constant speed, V , which is likely limited by the maximum (unhindered) myosin motor velocity. The abrupt cessation of contraction suggests that either a strong resistance to further contraction is suddenly encountered, which could reflect a rigid steric barrier, or that myosin motors have reached a limiting minimal distance from the dense bodies where the motors can no longer walk on actin filaments.

Because myosin motors are sensitive to load, the uniform speed of the contraction phase suggests that elastic forces do not increase (and are not relieved) during contraction. This observation, combined with the observation that elastic energy is not stored in contracted stress fibers, suggests that there is no elastic element in parallel with the contractile element, contrary to other recent models for stress fiber sarcomere mechanics (14,15).

Based on the model in Figure 2-8, V corresponds to the zero-load working velocity of myosin motors in living stress fibers. The mean velocity of myosin walking is found to be $0.0099 \mu\text{m}/\text{sec}$ (in vitro measurements of myosin velocity are in the range of $0.14 \mu\text{m}/\text{sec}$, Umemoto et al. (87)). While this speed may be limited by the maximum speed of the ensemble of myosin motors, we cannot rule out other sources of internal friction within the sarcomere operating in parallel with myosin motors. However, the near-instantaneous initial retraction argues against a significant external viscous drag limiting the rate of contraction after severing. Also, any internal or external viscous drag does not alter the main conclusions of the model: that spring elements do not contribute to the force balance in the stress fiber, and that there are internal barriers present which limit contraction under zero tension.

Based on the exponential distribution of contraction distances, x_c , reported in Figure 2-4B, the most probable state of a sarcomere following the initial instantaneous contraction is at its minimum length. This surprising conclusion again argues against models that invoke tensile or compressive elastic elements within the sarcomere to position the sarcomere length at some optimal value. A key question remains: how does the observed exponential distribution of contraction distances arise in a steady-state stress fiber? One possibility is that the tension in the stress fiber fluctuates in way that results in this distribution in lengths, as demonstrated by the following model.

If tension is balanced by myosin contractile forces only, and the tension-velocity relation is linear, then the contraction velocity has the form

$$v \equiv dx_c/dt = V(T/T_{\max} - 1) \quad (2-5)$$

Where V is the maximum myosin contraction speed at zero tension, as obtained from the sarcomere contraction measurements, and T_{\max} is the fiber tension required to stall contraction. Assume that the mean tension in the stress fiber, \bar{T} , is less than the stall tension for myosin contraction in the sarcomere, such that the sarcomeres tend to contract, thus decreasing x_c , with an effective drift velocity

$$\bar{v} = V(\bar{T}/T_{\max} - 1) < 0 \quad (2-6)$$

However, fluctuations in the instantaneous T could lead to transient increases in x_c , analogous to diffusion. The effective diffusion coefficient D for x_c arising from fluctuations in T , is given by

$$D = \left(\frac{V}{T_{\max}} \right)^2 \int_0^{\infty} C(\tau) d\tau \quad (2-7)$$

Where $C(\tau) \equiv \overline{T(t+\tau)T(t)} - \bar{T}^2$ is the autocorrelation function for the fluctuations. Under these assumptions, the distance x_c is governed by a diffusion process with constant drift toward an impenetrable barrier ($x_c \geq 0$), for which the stationary probability density, $p(x_c)$, has the exponential form

$$p(x_c) = \frac{\bar{v}}{D} \exp(-\bar{v}x_c / D) \quad (2-8)$$

Therefore, this model predicts an exponential distribution in x_c as observed experimentally, and the mean value of x_c is equal to $D/V(1 - \bar{T}/T_{\max})$.

In addition to explaining the distribution of contraction distances, the above model provides an alternative mechanical explanation for the observation that stimulation of myosin contraction of sarcomeres at a cell boundary by calyculin-A (51) causes

shortening of the stimulated sarcomeres and a corresponding lengthening of distal sarcomeres. The increase in myosin activity causes an overall increase the stress fiber tension, \bar{T} , and an overall increase in T . However, a greater stimulation of peripheral sarcomeres leads to a corresponding increase in their value of T_{\max} . In this interpretation, the calyculin-A treatment decreases the ratio \bar{T}/T_{\max} and hence the mean of x_c in peripheral sarcomeres, while increasing this ratio in distal sarcomeres. This can cause the observed distribution of sarcomere lengths in cells treated with calyculin-A.

Insight into the Mechanics of Stress Fibers

A key prediction of the proposed model is that, after the initial elastic retraction, sarcomere tension is entirely balanced by myosin contraction, without invoking elastic elements in parallel or a dependence of tension on sarcomere length. Removal of tension causes linear contraction against zero external resistance until the minimum distance is reached. Because the dynamics of individual sarcomeres in the linear retraction model differs from the stress fiber end retraction as a whole, a question arises as to whether this linear retraction model is consistent with the exponential retraction curves reported here (Figure 2-1D) and by Kumar et al. (49).

In fact, an approximately exponential retraction of the severed fiber end does arise from the linear contraction of multiple sarcomeres in series, if contraction distances x_c come from an exponential distribution, as we found in our measurements (Figure 2-4B). The measurements suggest that x_c has a probability density that can be approximated as an exponential density, such that

$$p(x_c)dx_c = \Delta^{-1}e^{-x_c/\Delta}dx_c \quad (2-9)$$

is the probability of a contraction distance between x_c and $x_c + dx_c$, and Δ is the mean contraction distance ($\Delta = D/V(1 - \bar{T}/T_{\max})$ in the above model). From Equation 2-4, the time-dependent mean sarcomere length is thus exponential, given by

$$\langle x(t) \rangle = x_{\min} + \int_{Vt}^{\infty} (x_c - Vt)p(x_c)dx_c = x_{\min} + \Delta e^{-Vt/\Delta} \quad (2-10)$$

For a stress fiber consisting of N sarcomeres, the mean initial length is $L_0 = N[\delta + x_{\min} + \Delta]$. Following cutting and the initial elastic retraction, the mean time-dependent length is $L(t) = N[x_{\min} + \Delta e^{-Vt/\Delta}]$, such that relative retraction length is

$$R(t) \equiv \frac{L_0 - L(t)}{L_0 - L_{\min}} = \frac{\delta + \Delta(1 - e^{-Vt/\Delta})}{\delta + \Delta} \quad (2-11)$$

The solid line in Figure 2-1D is a least-squares regression fit of Equation 2-11 to these data, illustrating the good agreement of the exponential model, with initial retraction, to the stress fiber retraction data. If the initial retraction δ happens to be small relative to Δ , then this equation becomes approximately $R(t) \cong (1 - e^{-Vt/\Delta})$, consistent with the exponential distribution reported by Kumar et al. (49). Therefore, there is no inconsistency between the linear contraction model and the apparent exponential retraction curves of the severed ends of the stress fiber.

Summary of Findings

In summary, we have performed the first measurements of sarcomere contraction in stress fibers formed by living endothelial cells. Our results suggest that tension in the fiber is established entirely by myosin activity, and is not influenced by spring elements as is currently believed. Taken together, our experiments and analysis shed new light into the behavior of living sarcomeres and suggest a new model for stress fiber

sarcomere mechanics. Future avenues of investigation will need to identify molecular players that contribute to the stiffness of sarcomeres and determine the barrier position.

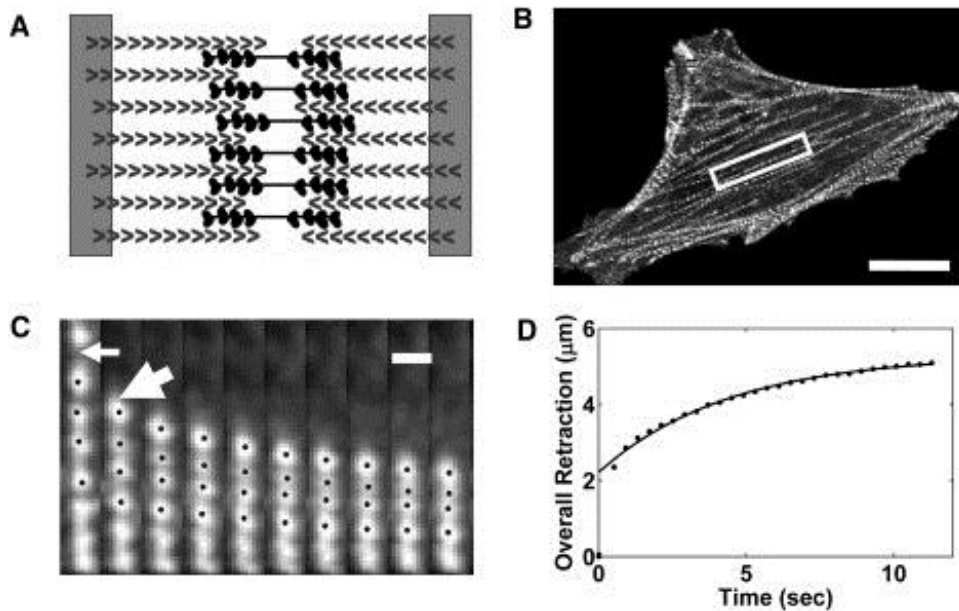


Figure 2-1. Sarcomeres contract in a severed fiber. (A) Schematic showing the structure of a sarcomere with: dense bodies of actin bundling proteins such as α -actinin marking the ends and polymerization competent ends of actin filaments pointing inwards joined by bipolar myosin filaments. (B) An epi-fluorescence micrograph illustrating the punctate staining of EGFP- α -actinin in dense bodies of bovine capillary endothelial cell stress fibers (Scale bar, 20 μm). (C) A kymograph showing the results for one half of a severed fiber cut at the thin arrow. Notice that sarcomeres contract and that the contraction is not uniform in every sarcomere (thick arrow) (Scale bar, 1.4 μm and time between frames is 840 ms). (D). The distance the severed edge moves follows an exponential form; the solid line is a least-squares regression fit of the retraction model (Eq. 2-11) to the data.

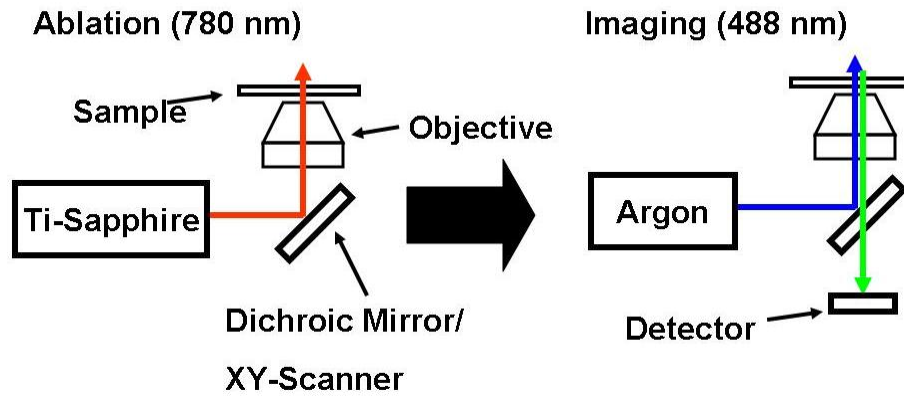


Figure 2-2. Cartoon schematic of microscope system used for ablation and imaging. A mode-locked ultrafast Ti-Sapphire laser at 780 nm is used to selectively sever GFP- α -actinin labeled stress fibers in Bovine Capillary Endothelial Cells. After the fiber is severed the confocal images are continuously recorded at 488 nm until retraction is complete

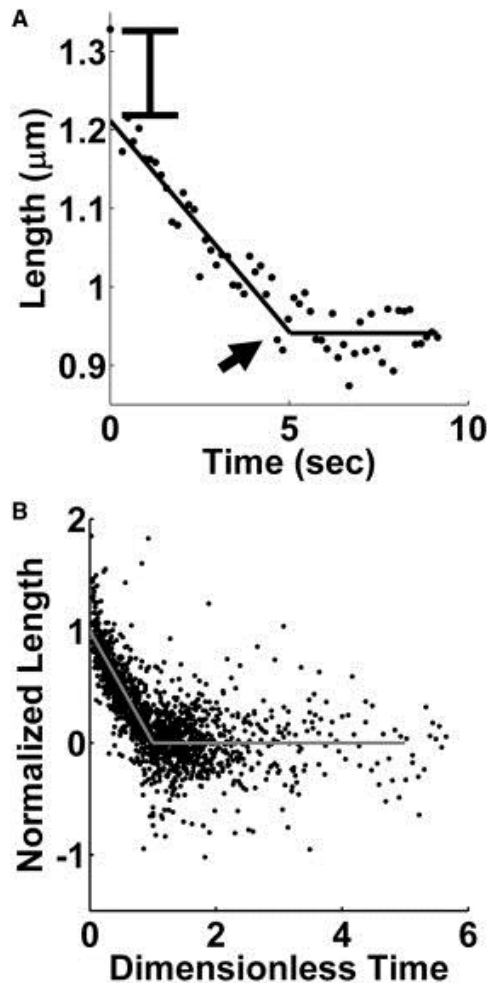


Figure 2-3. Time dependent length change of a sarcomere. (A) Representative example of sarcomere length change in a severed fiber. The contraction occurs in two distinct phases: first a quick initial drop (marked on plot) followed by sustained contraction at nearly constant speed. After some time the sarcomere reaches a steady state length (arrow) and remains there for the remainder of the experiment. (B) Pooled data from contraction of 28 sarcomeres in 18 cells was normalized and plotted together excluding initial sarcomere lengths (see text for details). A clear linear trend is visible in the normalized data.

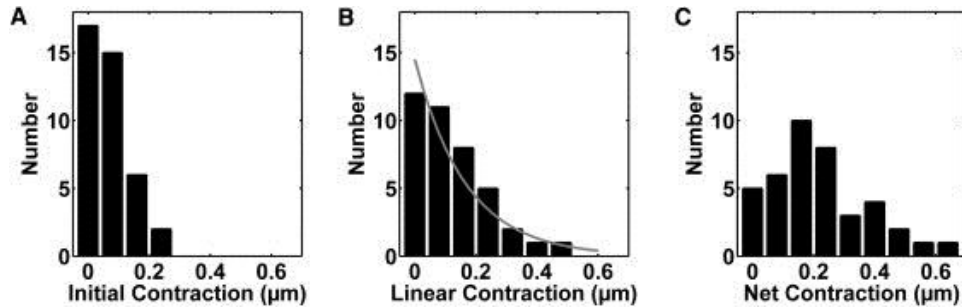


Figure 2-4. Histograms of sarcomere contraction parameters. (A) The distribution of the initial length of sarcomeres appears symmetric with a mean and standard deviation of $0.10 \mu\text{m} \pm 0.06 \mu\text{m}$ ($N = 40$ sarcomeres, 18 cells). (B) Interestingly the distribution of the linear contraction appears to be approximately exponential (grey curve is drawn for visualization) with a mean and standard deviation of $0.15 \mu\text{m} \pm 0.09 \mu\text{m}$ ($N = 28$ sarcomeres, 18 cells). (C) The distribution of the net contraction appears to be a shifted exponential with a mean and standard deviation of $0.26 \mu\text{m} \pm 0.11 \mu\text{m}$ ($N = 40$ sarcomeres, 18 cells).

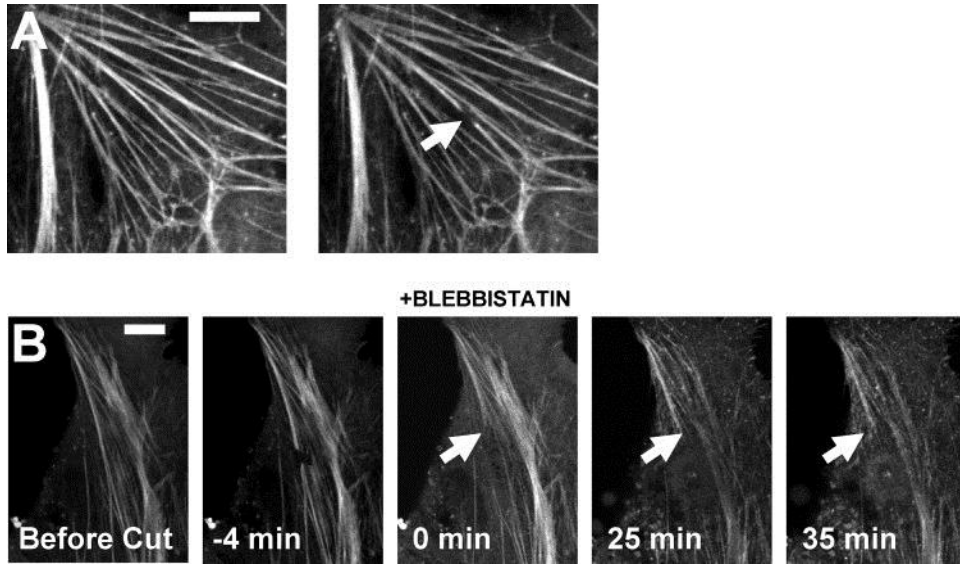


Figure 2-5. Potential energy is not stored in a severed stress fiber. (A) A stress fiber severed in a cell treated with 50 μM blebbistatin retracted minimally ($\sim 1 \mu\text{m}$ in 20 sec) indicating that myosin activity is responsible for the stress fiber retraction (Scale bar 10 μm). (B) A cut stress fiber that is allowed to reach steady state (marked by arrow) before myosin poisoning does not recover its length after blebbistatin treatment for several minutes. This indicates that potential energy was not stored in the contracted fiber. (Scale bar 10 μm).



Figure 2-6. Second example of potential energy not stored in a severed stress fiber. Stress fibers labeled with GFP-actin in bovine capillary endothelial were severed using a femtosecond laser and allowed to reach steady state (Scale bar 10 μm). After stress fiber contraction reached steady state, myosin activity was poisoned with blebbistatin and a confocal micrograph was taken after 35 minutes. Stress fibers did not significantly lengthen or relax during the time course indicating that potential energy was not stored in the contracted fiber.

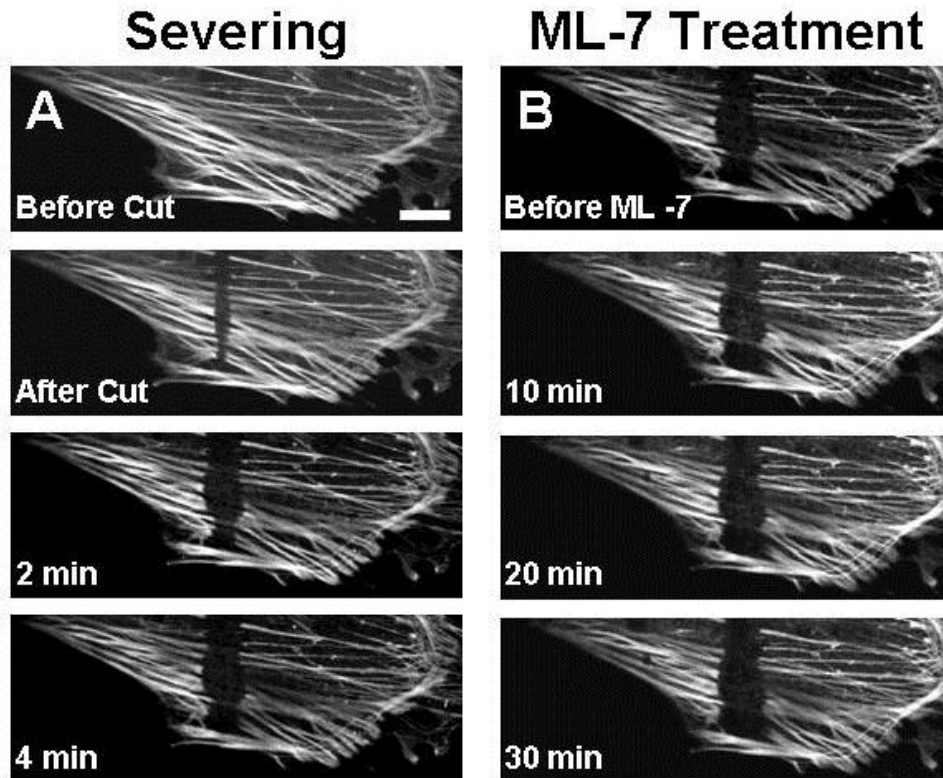


Figure 2-7. Fully contracted severed stress fibers do not relax when treated with ML7. (A) Stress fibers labeled with GFP-actin in bovine capillary endothelial were severed using a femtosecond laser and allowed to reach steady state (Scale bar 10 μm). (B) After stress fiber contraction reached steady state, myosin activity was poisoned with ML-7 and confocal micrographs were taken every 10 minutes. Stress fibers did not lengthen or relax during the time course indicating that potential energy was not stored in the contracted fiber.

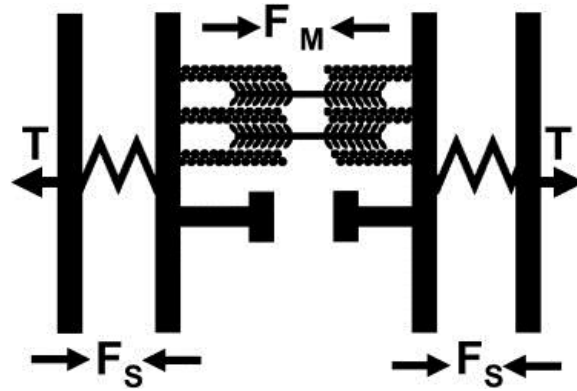


Figure 2-8. Proposed mechanical model for the sarcomere. The tension, T , in the stress fiber is only determined by myosin forces, F_M , in series with a stiff elastic element, F_S . An impenetrable barrier prevents further sarcomere contraction at some minimal sarcomere length.

CHAPTER 3 SARCOMERE LENGTH FLUCTUATIONS AND FLOW IN CAPILLARY ENDOTHELIAL CELLS

Generation and maintenance of intracellular tension is necessary for endothelial cells to adhere to the basement membrane and resist external mechanical stresses such as those due to blood flow. Tension in endothelial cells is generated in stress fibers which are observed not only in vitro, but also in vivo (25,32) in endothelial cells. Endothelial stress fibers are made from tens of repeating contractile units called sarcomeres assembled end to end (37,44). Stress fiber sarcomeres consist of periodic actomyosin contractile elements separated by crosslinked regions of actin filaments referred to as “dense bodies” containing proteins such as α -actinin. Translocation of bipolar myosin filaments along the actin filaments generates force in the sarcomere. This tension is balanced by the extracellular matrix at focal adhesions (23).

Stress fibers are extremely dynamic structures that form as a result of continual generation of F-actin at focal adhesions and the cell membrane (88,89) and subsequent crosslinking and bundling of microfilaments (90). Dynamic assembly and disassembly of stress fibers is crucial for the cell's ability to adapt to external mechanical stimuli (72). Recently it has been reported that stress fibers undergo force induced thinning events that result in stress fiber breakage (91). Surprisingly, the dynamic behaviors of sarcomeres, which are building blocks of stress fibers, have not received such attention. It is known that sarcomeres respond dynamically on treatment with calyculin A with shortening of peripheral sarcomeres and lengthening of central sarcomeres (51). Nascent sarcomeres have also been shown to flow in at focal adhesions at the cell periphery (88,89). Using femtosecond laser ablation to sever individual stress fibers, we

recently explained the measured sarcomere contraction length distributions by hypothesizing that sarcomeres in a stress fiber may continually fluctuate with time (92). However, we are not aware of studies which have actually demonstrated fluctuations in sarcomere lengths in living cells.

We found that sarcomere lengths indeed continually fluctuate in living endothelial cells. Nascent sarcomeres were observed to flow into pre-existing fibers at focal adhesions throughout the cell with flow velocities that do not correlate with focal adhesion size. Frequently sarcomeres were observed to be consumed in 'sinks' at stress fiber junctions. Together, these results shed new light into the dynamics of stress fiber sarcomeres in endothelial cells.

Materials and Methods

Cell Culture and Transfections

Bovine capillary endothelial (BCE) cells, passages 10-13, were maintained at 37°C in humidified 10% CO₂. The BCE cells were cultured on tissue culture dishes in complete medium consisting of low-glucose Dulbecco's modified Eagle's medium (DMEM; Mediatech, Manassas, VA) supplemented with 10% donor bovine serum (Gibco, Grand Island, NY), 1% 1M HEPES (Mediatech), glutamine (0.292 mg/ml)/ penicillin (100 U/ml)/ streptomycin (100 g/ml) (Sigma, St. Louis, MO) and basic FGF (2 ng/ml; Sigma). This culture method was described previously in (92) and in great detail in Chapter 2.

For experiments, cells were transiently transfected with an EGFP- α -actinin-1 plasmid (kindly provided by Prof. Carol Otey) using the Effectene (Qiagen, Valencia, CA) reagent. Previous studies have rigorously shown that the fusion construct is functional and localizes with the endogenous protein (83). Cells were transfected for 6

hours in 12 well cell culture dish. After 24 hours the cells were trypsinized (Gibco) and plated sparsely on glass bottom dishes (MatTek, Ashland, TX). Cells were imaged approximately 24 hrs after seeding on glass bottom dishes. The transfection protocol used for these studies is described in Chapter 2.

Because the epi-fluorescence microscope used for these imaging experiments was outfitted with an environmental chamber capable of keeping a 10% CO₂ environment normal culture media was used except for one change. Culture media was replaced with imaging media consisting of low-glucose phenol red free Dulbecco's modified Eagle's medium (Gibco) supplemented with 10% donor bovine serum (Gibco), 1% 1M HEPES (Mediatech) and glutamine (0.292 mg/ml)/ penicillin (100 U/ml)/ streptomycin (100 g/ml) (Sigma).

Micropatterning of Bovine Capillary Endothelial Cells

To determine if sarcomere dynamics were dependent on cellular shape changes, BCE cells were seeded onto micropatterned islands of fibronectin. Microcontact printing was done according to previously published methods (93). Molds for the stamps were produced using standard UV lithography techniques. PDMS (Sylgard 184 kit, Dow Corning, MI) stamps were created by casting photo-resist mold using a 10:1 ratio (w/w) of elastomer to hardener and cured at 60°C for 2 hr and postcured at 100°C for 1hr. These PDMS stamps can be used for many experiments and should be kept in a clean environment.

To micropattern BCE cells the following steps were used. Human fibronectin (50µg/ml solution) (BD Biocoat™, Franklin Lakes, NJ) was adsorbed on the PDMS stamps by coating stamps with FN solution and allowed to incubate overnight at 4°C.

Stamps were then thoroughly washed by pipetting 1 ml of DD H₂O onto the stamp 5 times. After washing, the water was aspirated and the stamps were blown dry with N₂. Using tweezers the stamp was carefully placed feature side down onto an Ibidi dish. A small weight was placed onto the stamp to enhance transfer of the FN from the stamp to the dish. After 5 minutes the stamp and the weight were removed with care taken not to slide the stamp. The uncontacted area was then blocked with PLL-g-Poly-ethylene glycol (SuSoS AG) for 15 minutes, preventing protein adsorption and cell attachment. After treatment the surface was washed and trypsinized cells are plated.

Time- Lapse Imaging of Labeled Sarcomeres

Imaging was done on an inverted Nikon TE-2000 equipped with a temperature and CO₂ controlled environmental chamber. The environmental chamber allowed experiments to be conducted at the culture conditions described above (37°C and humidified 10% CO₂). Time-lapse live cell widefield epi-fluorescent imaging was conducted with a 63X, 1.49 NA or a 40X 1.4 NA oil immersion objective. Images were captured at 3 minute intervals with a cooled CCD camera controlled by Nikon Elements software. To minimize photobleaching and toxic effects, the exposure time was kept below 500 ms and less than 50% of light intensity was used. In order to observe significant dynamics each cell was imaged between 2-8 hours.

Image Analysis

To measure sarcomere fluctuations in stress fibers during time lapse imaging, custom tracking software describe previously (92) was used to determine the positions of GFP- α -actinin labeled dense bodies to sub-pixel accuracy. Image sequences from the Nikon Elements software package were exported to ImageJ (NIH) for image

processing. Tracking a simulated particle indicated that the error was minimal, less than 1 percent. The procedure for using the software is identical to what is described in Chapter 2.

Kymographs were prepared in ImageJ by first identifying focal adhesions in the time lapse image series that displayed clear production of dense bodies. Focal adhesions of interest were rotated to align vertically and then cropped from the image. The 'stacks' function of ImageJ was then used to create kymographs. Flow velocities were calculated by identifying the centroid of a single dense body at multiple time points. Then a line was fit using linear regression whose slope was used as the flow velocity after correcting the units.

Particle Image Velocimetry was performed in MATLAB using MatPIV (94) for all images (20) of square cells collected over 1 hr. The individual velocity fields were then averaged to obtain a time averaged velocity field for the cell. Vectors were plotted at 12 pixel increments (5 μm) on the first image of the time series to illustrate the time averaged flow field.

Results

Fluctuations in Sarcomere Length

To investigate sarcomere dynamics in endothelial cells, we imaged the dynamics of EGFP- α -actinin transfected BCE cells. Sarcomeres in the same fiber were observed to undergo significant changes in length on the time scale of several minutes (Figure 3-1 A and B) in cells cultured in normal growth medium. Individual sarcomeres in a given fiber exhibited different behaviors, with some sarcomeres shortening or lengthening while others fluctuated around the mean (Figure 3-1B). The length changes were random because the deviation from the mean length remains close to zero throughout

the time course of the measurement (Figure 3-1C). The autocorrelation of the pooled population of measured sarcomeres revealed that correlations in sarcomere length changes die out over a time scale of approximately 20 minutes. The mean sarcomere length from the autocorrelation was found to be 1.3 μm and a standard deviation of the fluctuations was 0.2 μm (Figure 3-1D).

We next asked if sarcomere length fluctuations resulted in perturbations to the stress fiber network from cellular shape changes. To control cell shape, we confined cells on 40 μm square micropatterned islands of fibronectin, which has been shown to minimally affect cellular viability (95). BCE cells transfected with EGFP- α -actinin displayed an ordered network of stress fibers with most fibers aligned along the diagonal (Figure 3-2A). Sarcomere lengths fluctuated continuously even in confined patterned cells (Figure 3-2A), suggesting that fluctuations were not dependent on overall cell shape changes.

Flow of Nascent Sarcomeres from Focal Adhesions

Previous studies have shown that nascent sarcomeres flow out from focal adhesions at the cell periphery (88,89). In BCEs, we found that nascent sarcomeres flowed out of adhesions at the periphery as well as at adhesions in the interior of the cell. (Figure 3-3A, 3-4C). In many cases, the sarcomeres did not have coherent dense bodies, but became more organized as they flowed into the cell (Figure 3-3A). Focal adhesions remain stationary as the dense bodies moved inward which established that the sarcomeres were indeed flowing in (and not just sliding because of focal adhesion movement). In the majority of cases, the velocity of nascent dense bodies was constant with increasing distance from the focal adhesion (Figure 3-3E). When the trajectories for

successive emerging sarcomeres from a single focal adhesion were tracked, the velocity was found to be remarkably uniform (Figure 3-3E). The measured mean sarcomere velocity in endothelial cells was $0.075 \mu\text{m}/\text{min} \pm 0.0066 \mu\text{m}/\text{min}$ which was roughly three times less than that measured in U2OS cells (89) and podocytes and fibroblasts (88).

Focal adhesions in cells confined to square micropatterned islands of fibronectin were found to exist at both the periphery as reported before (96) and in the interior of the cell (Figure 3-4A). Particle image velocimetry (PIV) was used to determine the flow pattern of dense bodies in the micropatterned BCE cells. The results indicated that there was continual flow of nascent dense bodies from all focal adhesions towards the center of the cell (Figure 3-4B). Flow of dense bodies from an interior focal adhesion is illustrated in the kymograph of Figure 3-4C.

Sarcomere Flow Velocity from Focal Adhesions is Tension Independent

Dense bodies were observed to flow from focal adhesions of all sizes throughout the cell. It has been previously established that focal adhesion size is correlated with the net tensile force on the adhesion (22,97,98). To determine whether the rate of sarcomere production was dependent on focal adhesion size and thus tension, the flow velocity was plotted against size of the associated focal adhesion (Figure 3-4). No correlation was found between dense body flow rate and focal adhesion size suggesting that flow does not depend on tension.

Sarcomeres are Consumed at 'Sinks'

Since new sarcomeres are continually incorporated at focal adhesions, it stands to reason that sarcomeres must be consumed somehow along the fiber length. We

observed sarcomeres being consumed at discrete points, or “sinks”, along the stress fibers, most often (but not always) at junctions between adjacent stress fibers (Figure 3-5A and 3-6). In some cases sarcomeres were seen to join end-on as illustrated in Figure 3-5B. Taken together these results indicate that multiple mechanisms for disassembly of sarcomeres exist in capillary endothelial cells.

Discussion

While stress fibers have been shown to be dynamic and responsive to mechanical stimuli, little is known about the dynamics of the sarcomeric subunits of stress fibers. In this paper, we present observations of a rich array of dynamic behaviors exhibited by sarcomeres in living cells. Stress fiber sarcomeres were observed to fluctuate in length, flow from focal adhesions and be consumed at ‘sinks’. Identical behaviors were found in cells confined to micropatterned islands of fibronectin. The rate of new sarcomere formation and incorporation from focal adhesions was found not to be correlated with focal adhesion size.

Interestingly, within the same stress fiber, some sarcomeres elongated while other nearby sarcomeres simultaneously shrunk. Since tension is commonly assumed to be uniform along the length of the stress fiber, such fluctuations are difficult to explain with models which assume that sarcomere length is elastically coupled to tension. On the other hand, if tension and length were weakly coupled and instead only contraction/expansion speeds were governed by tension, then small changes in local myosin activity could lead to large changes in sarcomere length, while maintaining a uniform overall tension. We recently proposed such a model to explain the constant contraction speed and the exponential distribution of contraction distances following removal of tension by laser-severing of stress fibers (92).

Previous studies have reported that sarcomeres are assembled and flow out of focal adhesions in podocytes, fibroblasts (88) and U2OS cells (89). Because stress fibers are anchored to the substrate at focal adhesions and are under isometric tension, any new sarcomeric units added to the fiber must form under tension. We found that sarcomere flow velocities are independent of focal adhesion size; it has been shown that focal adhesion size correlates with tension ((22,97,98)). It has been previously demonstrated that inhibition of myosin stops the flow of sarcomeres into the fiber (88). Taken together these findings suggest that while myosin activity is necessary for flow, the flow is not influenced by the magnitude of tension. This independence of actin assembly rate on tension is consistent with an end-tracking motor model for insertional polymerization of focal adhesion-attached filaments plus-ends (99,100) but not models where actin assembly of attached filaments is enhanced by tension (101,102). Moreover, the slow, uniform speed of actin assembly that is independent of focal adhesion size argues against an assembly mechanism limited by the rate of monomer diffusion, and suggests that the assembly rate is governed by a molecular timer with a rate constant of around 0.5 s^{-1} (based on the measured speed divided by the 2.7 nm added length per actin monomer).

The PIV analysis in patterned cells suggests that there is continual flow of dense bodies from all focal adhesions directed towards the diagonal of the square cell. Because the steady state length of the stress fiber is approximately constant, in the absence of any sinks the length of each sarcomere would decrease continuously along the fiber. A simple number balance would require the existence of “sinks” in order to maintain a steady state stress fiber length. Our finding of sarcomere fusion along the

stress fiber length, therefore suggests a mechanism by which the cell controls sarcomere length at optimal values.

Summary of a Comprehensive Sarcomere Model

We have demonstrated that endothelial stress fiber sarcomeres undergo a variety of dynamic behaviors including fluctuations, generation and consumption. Stress fibers form a dynamic and continually evolving connected network that has mechanisms to both increase and decrease tension. Further work is needed to determine the molecular mechanisms of sarcomere assembly at focal adhesions and to parse out the mechanisms underlying tensional fluctuations. Our results of sarcomere contraction and our observations of sarcomere fluctuations in intact stress fibers are enough to lead to a self consistent model of the sarcomere.

As reported in Chapter 2 sarcomeres in severed fibers contracted linearly at constant velocity, V , following a fast initial contraction δ . The sustained linear contraction ended at minimum sarcomere length, x_{\min} , suggesting a barrier to prevent further contraction. While the initial contraction distances, δ , were distributed randomly, distribution of the linear contraction distance, x_c , was exponential with a mean $\overline{x_c} \equiv \Delta \approx 0.19 \mu\text{m}$ (Figure 2-4B). In this chapter we report observations of fluctuating sarcomeres in intact stress fibers with standard deviation $\sigma \approx 0.20$. This estimation is consistent with the mean linear contracted distance reported in Chapter 2 because for an exponential distribution the variance is equal to the mean squared ($\sigma^2 = \Delta^2$). The autocorrelation function of the sarcomere fluctuations gave a relaxation time, $\tau_L \approx 1000 \text{ sec}$.

Taken together these observations suggest a model where tension fluctuations determine the distribution of sarcomere lengths. What follows is a description of a sarcomere model which meets this criterion. First we assume that the instantaneous contraction speed in the i th sarcomere, v_i , is proportional to the net tension in the sarcomere and thus follows this form:

$$\frac{dL_i}{dt} = -v_i = -\beta(T_i - T_{ext}) \quad (3-1)$$

where L_i is the i th sarcomere length, T_i is the tension generated by myosin within the sarcomere, and T_{ext} is the tension on stress fiber (assumed uniform along the length of the stress fiber). Assuming that there exists instantaneous fluctuations in myosin activity in the sarcomere then T can be assumed to be a fluctuating random variable with a mean of $\bar{T} = v_d / \beta$ and variance σ_T^2 . The external tension, T_{ext} , on a stress fiber at

constant length consisting of n sarcomeres can be described as $T_{ext} = \frac{1}{n} \sum_{i=1}^n T_i$, hence

$\bar{T}_{ext} = \bar{T}$ and $\sigma_{T_{ext}}^2 = \frac{1}{n} \sigma_T^2$. Thus fluctuations in T_{ext} are expected to be small (by factor $1/n$)

relative to fluctuations in T . Tension fluctuations lead to diffusive behavior of the sarcomere length, with probability density $p(L, t)$ described by the Fokker-Planck equation,

$$\partial_t p(L, t) = \partial_L v_d p(L, t) + D \partial_L^2 p(L, t) \quad (3-2)$$

where $v_d = \beta(\bar{T} - T_{ext})$ is the drift velocity, and D is a diffusion coefficient. The diffusion coefficient can be related to fluctuations in the myosin contraction velocity by integrating the area under the velocity-velocity autocorrelation function and thus described as:

$$D = \frac{1}{2} \sigma_v^2 \tau_v \quad (3-3)$$

where σ_v^2 is the variance in velocity fluctuations (equal to $\beta^2 \sigma_T^2$), and τ_v is the relaxation time in speed fluctuations. The relaxation time of the speed fluctuations, τ_v , can be described according to the following form.

$$\tau_v \equiv \int_0^{\infty} \frac{\langle v(t)v(t+t') \rangle - v_d^2}{\sigma_v^2} dt' = \int_0^{\infty} \frac{\langle T(t)T(t+t') \rangle - \bar{T}^2}{\sigma_T^2} dt' \quad (3-4)$$

The steady-state solution to Equation 3-2, imposing the boundary condition $p_s(L) = 0$ for $L < L_m$, is:

$$p_s(L) = \frac{v_d}{D} e^{-v_d(L-L_m)/D} \text{ for } L \geq L_m \quad (3-5)$$

Comparing Equation 3-5 to the observed distribution of the linear contraction distance, x_c , implies that $\Delta = D/v_d$. From Equation 3-2 we get that the relaxation time constant for length fluctuations is $\tau_L = D/v_d^2$. Hence we can solve for D and v_d in terms of experimentally estimated parameters Δ and τ_L where $D = \Delta^2/\tau_L$ and $v_d = \Delta/\tau_L$. We have established earlier that for an exponential distribution $\sigma^2 = \Delta^2$ and thus D and v_d can be estimated using only from parameters obtained from the autocorrelation of sarcomere length fluctuations. Using the estimates of Δ and τ_L from the autocorrelation reported in Figure 3-1 we find that $D = 4 \times 10^{-5} \mu\text{m}^2/\text{sec}$ and $v_d = 2 \times 10^{-4} \mu\text{m}/\text{sec}$.

In summary we have shown that our sarcomere contraction experiments and our observations of sarcomere fluctuations are consistent with each other and lead to a model where sarcomere lengths are dependent on tension fluctuations. We have demonstrated that the autocorrelation function of fluctuating sarcomeres is itself

sufficient to estimate the parameters that govern the distribution of sarcomere lengths. In the future further breakdown of D into variance and relaxation time in speed (Equation 3-3) can be obtained from the autocorrelation in the fluctuation speed on the shorter time scale.

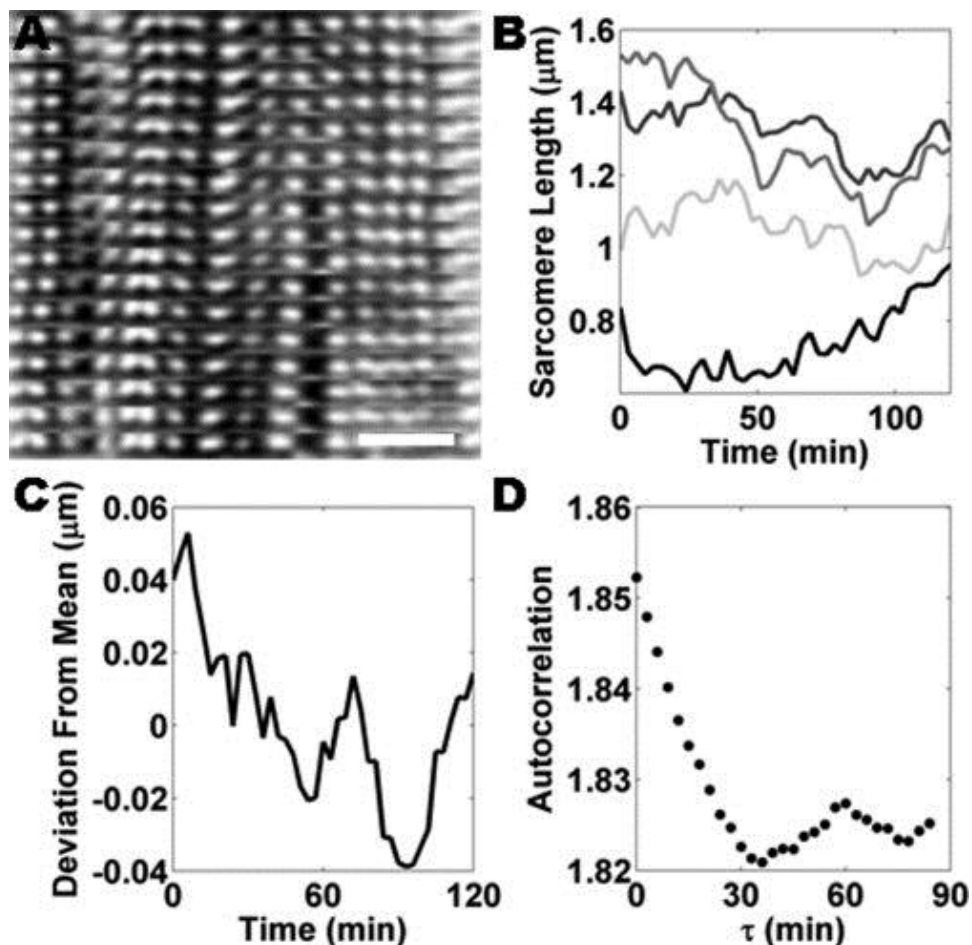


Figure 3-1. Sarcomeres undergo dynamic length fluctuations. (A) A kymograph showing sarcomeres undergoing length fluctuations during time lapse epi-fluorescence imaging (Scale bar is 1.4 μm and time between frames is 3 min). Note that sarcomeres do not behave uniformly during the time course. (B) Four sarcomere lengths from the same stress fiber are plotted with respect to time. The trajectories show the heterogeneous nature of sarcomere fluctuations. (C) The deviation from the mean for 13 sarcomeres is plotted with respect to time. The fluctuations can be assumed to be random because the deviation fluctuates around zero. (D) The pooled autocorrelation was calculated for 13 sarcomeres indicating that correlations in the fluctuations die out after approximately 30 minutes.

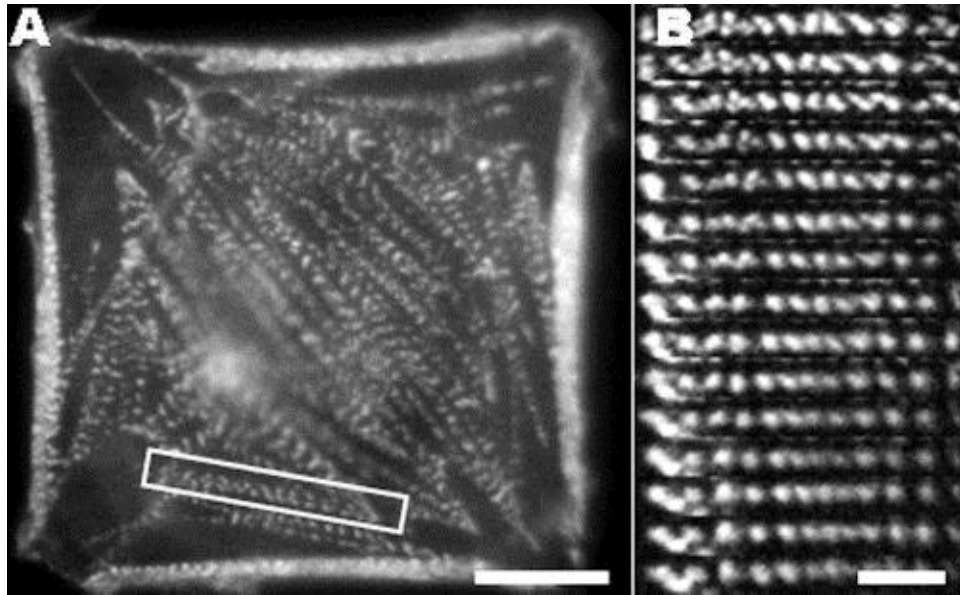


Figure 3-2. Sarcomeres undergo length fluctuations in cells with confined shaped. (A) BCE cells transfected with EGFP- α -actinin were seeded onto square micropatterned islands of fibronectin. Shown here is an epi-fluorescence micrograph illustrating the stress fiber network of micropatterned BCE cells (Scale Bar 10 μ m) (B). This kymograph shows the dynamics of a stress fiber (labeled with box in A) in a micropatterned BCE cell. The fiber undergoes qualitatively similar fluctuations to stress fibers from unpatterned cells suggesting that transient shape changes are not the cause of fluctuations (Scale Bar 4 μ m and 18 min).

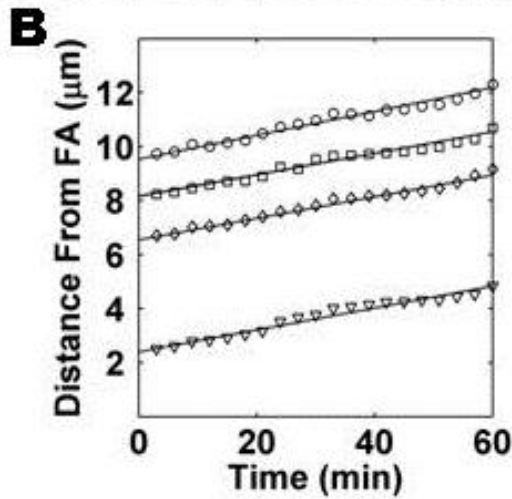
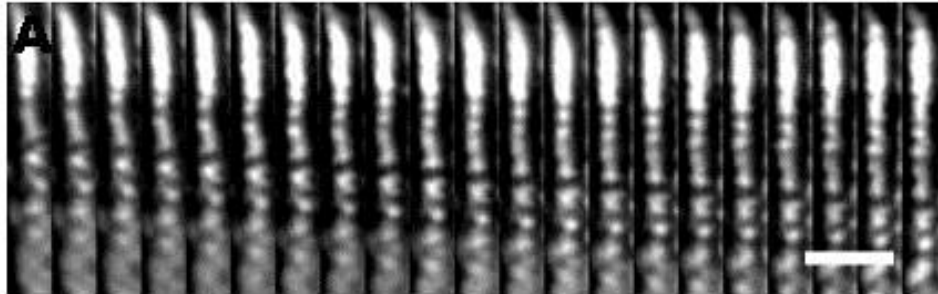


Figure 3-3. Nascent sarcomeres flow from all focal adhesions. (A) A kymograph illustrating the continual flow of nascent sarcomeres from focal adhesions in BCE cells. The focal adhesion remains stationary and approximately the same size ruling out focal adhesion sliding. (Scale bar 5 μm and 6 min) (B) The trajectories of four dense bodies flowing from a single focal adhesion are plotted with respect to time. Sarcomeres were observed to flow from focal adhesions at constant velocity as evidenced by the constant slope of each dense body. Successive sarcomeres displayed almost identical velocities as evidenced by the parallel trajectories

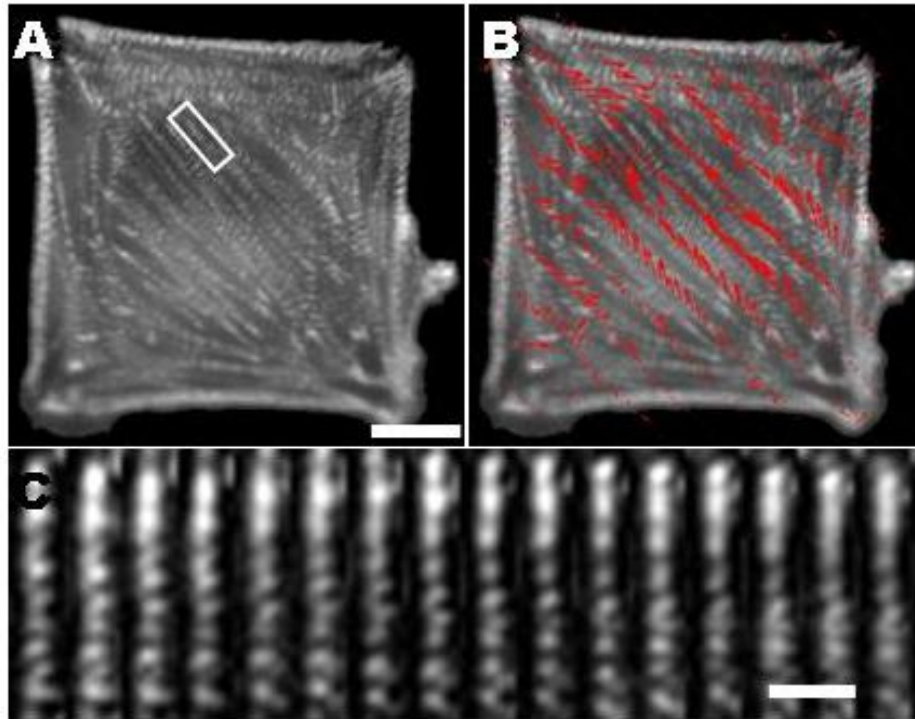


Figure 3-4. Nascent sarcomeres flow inwards from all focal adhesions in patterned cells (A) A fluorescence micrograph of EGFP- α -actinin transfected BCE cells confined to square micropatterned islands of fibronectin (Scale bar 10 μ m). (B) Particle image velocimetry was used to determine bulk flow patterns throughout the entire micropatterned BCE cell. The PIV results indicate that nascent dense bodies flow from focal adhesions throughout the entire cell and not just at the periphery. (C) A kymograph of flow of dense bodies from an interior focal adhesion (labeled with box in B) illustrates that flow occurs from interior focal adhesions (Scale bar 5 μ m and 6 min).

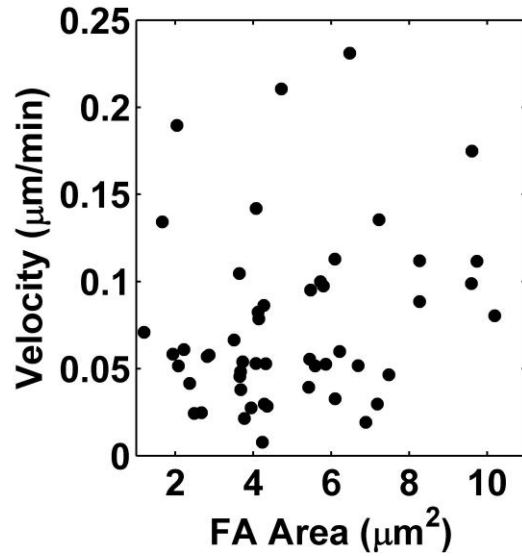


Figure 3-5. Sarcomere flow rate is independent of mechanical stress. (A) Sarcomere flow velocities from single focal adhesions are plotted with respect to the focal adhesion size (n= 51 FA from 7 cells). There is little correlation between sarcomere flow rate and focal adhesion size (correlation coefficient of 0.23).

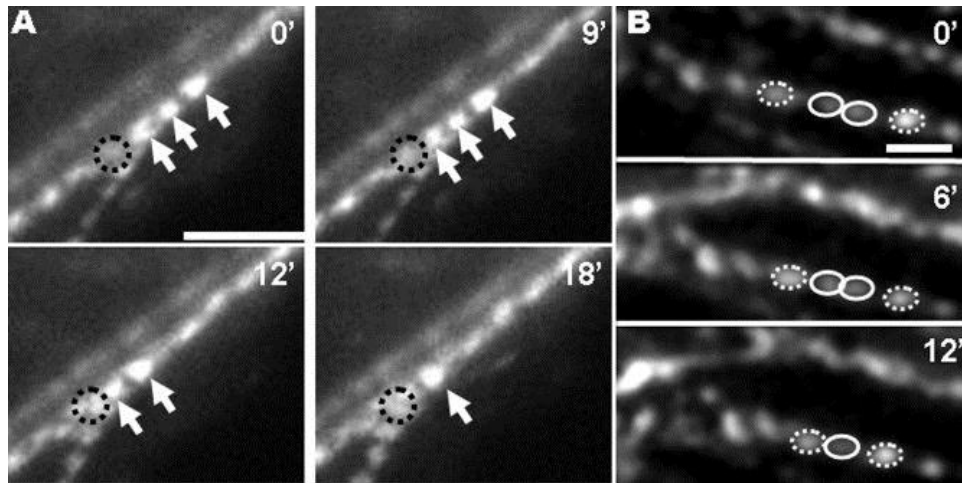


Figure 3-6. Sarcomeres are consumed at sinks and join end-on to maintain tension. (A) Time lapse images of EGFP- α -actinin transfected BCE cells reveal that sarcomeres are consumed in “sinks” that exist at the junction of two stress fibers. Dense bodies (arrows) move towards the “sink” (black dotted circle) until two disappear during the course of 18 minutes (Scale Bar 5 μ m). (B) Dense bodies were observed to join end-on in stress fibers during time lapse imaging. A sarcomere shortens continuously until the two dense bodies (solid black circles) are indistinguishable while the neighboring sarcomeres (between solid and dotted black circles) maintain their integrity. (Scale Bar 2.5 μ m).

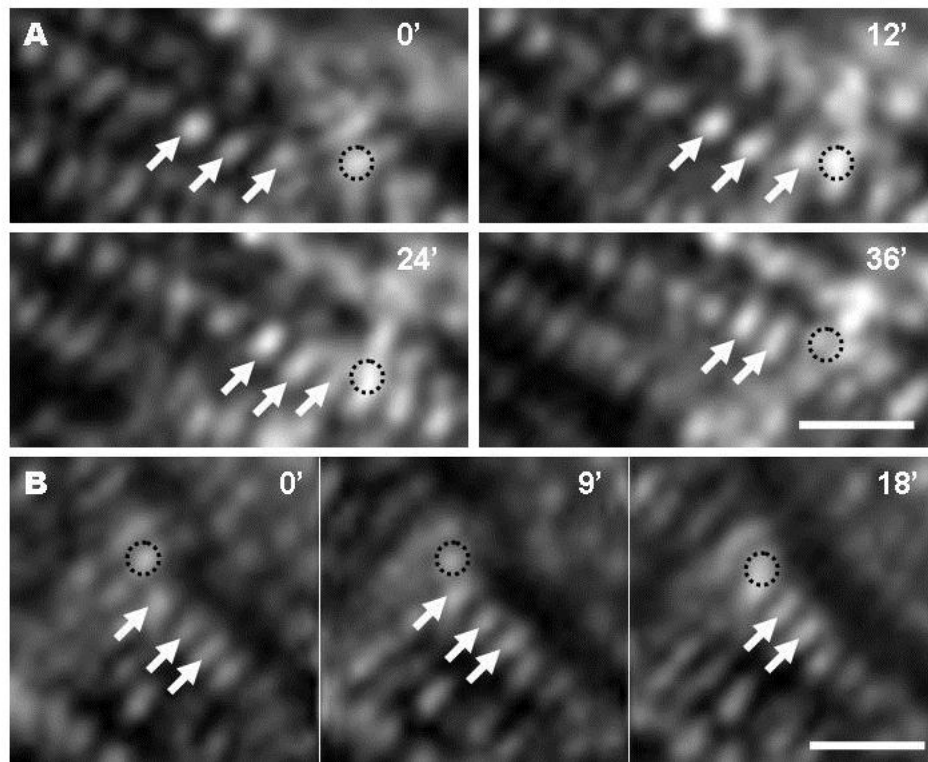


Figure 3-7. Sarcomeres are consumed to maintain tension. (A) Time lapse images of EGFP- α -actinin transfected BCE cells reveal that sarcomeres are consumed in “sinks” that exist at the junction of multiple stress fibers. Dense bodies (arrows) move towards the “sink” (black dotted circle) until one disappears during the course of 36 minutes (Scale Bar 2.5 μ m). (B) A second example of a sarcomere being consumed in a “sink” (black dotted circle) over the course of 18 minutes.

CHAPTER 4 EFFECTS OF DYNEIN ON MICROTUBULE MECHANICS

Microtubules are long stiff biopolymers observed in eukaryotic cells emanating outward from a central organizing center called the centrosome (29). Microtubules are known to play a key role in normal cell processes including transport of proteins and organelles, forming the mitotic spindle and positioning the centrosome for polarized cellular migration (29). These functions require force generation and transmission by microtubules. Despite their relatively high flexural rigidity (microtubules are the stiffest cytoskeletal filament by two orders of magnitude (54)), microtubules are frequently observed in buckled conformations at the cell periphery (29,55). As a result microtubules are generally assumed to be under compressive loading from force generated through polymerization at the plus-end tip (55). Based on observations of buckled microtubules, it has been hypothesized that microtubules act as cellular struts resisting tensile forces generated by the acto-myosin cytoskeleton (57-59).

Compressive forces have also been hypothesized to be responsible for centrosome centering (103-105). An issue with this hypothesis is that microtubules in vivo are in long conformations, such that the critical buckling force is approximately 1 pN which even a single motor protein can exceed (56,106). Recently Weitz and coworkers suggested that microtubules supported laterally by an elastic medium could support larger forces (55). Increasingly the minus-end directed motor dynein has been implicated in force generation in microtubules (63,65,107). Immobilized dynein on the actin cortex has been hypothesized to generate tensile forces on the centrosome by 'walking' towards the centrosome (107-109). A recent study by Odde and coworkers

implicated dynein in the anterograde motion of microtubules during microtubule buckling (29).

In this chapter, we investigated the role of dynein in determining buckled shapes of microtubules in living cells. Individual buckled microtubules were severed with a femtosecond laser to probe the nature of the force balance in a buckled microtubule. The purpose of severing the microtubule was to perturb the overall force balance and to use the time dependent dynamics of the newly freed ends to determine the key forces involved in microtubule buckling. Upon severing, the newly created minus-ended microtubules did not release their stored bending energy by straightening as expected of a filament under compression. Rather the slower depolymerizing minus-ended microtubules actually increased in curvature and bending energy. In those microtubules where a relatively small increase in curvature was observed, the minus-end depolymerized while maintaining shape. Individual microtubules were next severed in dynein inhibited cells. In dynein inhibited cells newly freed minus-ended microtubules were observed to release stored bending energy and straighten. These results suggest a new model in which where dynein generates tangential tensile forces on microtubules and frictionally resists lateral motion of microtubules.

Materials and Methods

Cell Culture, Plasmids and Transfection

Bovine capillary endothelial (BCE) cells were used at passages 11-14 and were maintained at 37°C in humidified 10% CO₂. The BCE cells were cultured on tissue culture dishes in complete medium consisting of low-glucose Dulbecco's modified Eagle's medium (DMEM; Mediatech, Manassas, VA) supplemented with 10% donor bovine serum (Gibco), 1% 1M HEPES (Mediatech) and glutamine (0.292 mg/ml)/

penicillin (100 U/ml)/ streptomycin (100 g/ml) (Sigma). The growth media was supplemented with 1 μ l of basic FGF per 1 ml of media (final concentration 2 ng/ml; Sigma). This culture method was described previously in (82).

For control experiments cells were infected with adenoviral EGFP- α -tubulin was provided by Prof. Donald Ingber. For dynein inhibition studies cells were transfected with DsRed-CC1 plasmid that was provided by Prof. Trina Schroer and infected with adenoviral EGFP- α -tubulin. To confirm that dynein inhibition by transfected CC1 was effective cells were fixed and immunostained with mouse monoclonal Golgi marker (Abcam) and Hoechst 33342. Transient transfection of plasmids into BCEs was done with Effectene[®] Transfection Reagent (QIAGEN). For microtubule stabilization experiments, Paclitaxel (Taxol, SIGMA-ALDRICH) was added to the media to a final concentration of 1 μ M one hour before the experiment.

Imaging was conducted with a CO₂-independent media as described previously (84). Briefly the CO₂-independent imaging medium (pH 7.3) was prepared by dissolving Hanks balanced salts, which are phenol-red and bicarbonate free, in 1000 ml of DD H₂O. The following supplements were added HEPES (20.0mM), 1% bovine serum albumin, and 1% of both MEM essential and nonessential amino acids (Sigma). Imaging media was further supplemented with 10% DBS and glutamine (0.292 mg/ml)/ penicillin (100 U/ml)/ streptomycin (100 g/ml) (Sigma).

Laser Ablation

For laser ablation experiments, an inverted Zeiss Axiovert 200M laser scanning confocal microscope (LSM 510 NLO, Thornwood, NY) was used with 63X, 1.4-NA Plan-Approchromatic oil immersion lens (Zeiss). In order to image EGFP- α -tubulin, the 488 nm laser line with the power attenuated to 5-10% and the appropriate GFP bandpass

filter was used. For dynein inhibition experiments, cells were confirmed to be expressing DsRed-CC1 using epifluorescence microscopy through the eyepiece and then a single confocal image was recorded using the 543 nm laser. To increase the quality of microtubule images, two frames were taken per time point and averaged. Single microtubule ablation was done with a Ti:Sapphire laser at 50-100% transmission (Chameleon XR, Coherent, Santa Clara, CA) as previously described (49,92). The Ti:Sapphire laser was focused through the objective and scanned a thin, $\sim 0.14 \mu\text{m}$, rectangle orthogonally crossing the width of the microtubule for 1-2 iterations. A wavelength of 790 nm was used with a laser-head power of 1.5 W, pulse duration of 140 fs and repetition rate of 90 MHz. After ablation confocal scans as described previously were collected using Zeiss LSM 510 4.2 software at 1-3 seconds/frame to capture the dynamics of microtubules after severing. A cartoon schematic of the microscope used for the ablation and imaging is included in Figure 2-2. Detailed methods used for ablation of single microtubules follow in the next paragraph and are similar to those discussed in Chapter 2.

Once cells were placed on the microscope and the correct focal plane was found the laser parameters for cutting were optimized. The separate lasers that were used for ablation and imaging must be aligned correctly to focus on the exact same position in the z-direction for optimal cutting. Changes in the alignment resulted in slightly different laser parameters being needed for optimal ablation from day to day. Before experiments were conducted a cell expressing clear microtubules was found and used to test laser parameters for cutting. Microtubules were generally most clearly visible in either thin protrusions around the periphery of the cell or under the nucleus. The FRAP module

included with the Zeiss microscope software was used to conduct ablation by scanning with the Ti:Sapphire laser at 790 nm.

Because microtubules were generally found in thin protrusions surrounding the cell periphery great care was taken to prevent collateral damage to the membrane. To optimize laser parameters the laser was initially set at 100% transmission power and to scan for one iteration. These conditions were tested by ablating a single microtubule. In the case where the microtubule was severed and no collateral damage was observed in the accompanying DIC image then experiments were continued using these settings. When collateral damage was observed the laser power was reduced incrementally by 10 % until a clean cut occurred. If the microtubule would not cut at 100% transmission multiple scanning iterations were used. No more than approximately 2 scans were used because the extended cutting scans resulted in unacceptable time resolution. In the case where it was not possible to sever the microtubule with multiple iterations then the 488 nm Argon and the Ti:Sapphire lasers were realigned. To realign the lasers, a cell was focused using the 488 nm laser and then the imaging conditions were switched to image the cell using the Ti:Sapphire laser at 790 nm. The vertical position of the Ti:Sapphire laser was slowly adjusted until the cell came into focus.

Root Mean Squared Curvature Calculations

To measure the root mean squared curvatures of buckled microtubules before and after severing a custom program was developed in MATLAB 7.2 (The MathWorks, Natick, MA). Before curvature measurements in MATLAB were performed, image sequences were processed by exporting image sequences to ImageJ (NIH). Images were then rotated to align in the horizontal direction and then processed using built in ImageJ functions to reduce noise, enhance contrast and smooth the image. The

commented MATLAB code for determining root mean squared microtubule curvatures is provided in Appendices B.1 and B.2.

The curvature of microtubules was estimated from traces of microtubules using the method described by Odde and coworkers as the three point method (29,110). Custom Matlab code was developed to determine coordinates for the microtubule traces with sub-pixel accuracy adapting methods described previously (110,111). A description of the process for determining microtubule coordinates and curvature is described below.

An initial trace of the microtubule to be analyzed was first provided to the program listed in Appendix B.1 by using the mouse to select points along the contour of the microtubule. The initial points were then used to segment the microtubule and local maxima were identified either row wise or column wise for each segment depending on the orientation of microtubule in the segment. The coordinates of the local maxima were refined to subpixel resolution by fitting a one dimensional Gaussian approximately orthogonally across the microtubule. The sub-pixel coordinates determined by Gaussian fitting were then provided to the program listed in Appendix B.2

Coordinates were then smoothed using the MATLAB function, “smooth”, to eliminate short wavelength measurement error and preserve long range microtubule buckles. The coordinates were then coarse grained such that coordinates a defined number, n , apart were connected with a line segment. The series of line segments were then used to estimate the local curvature according the three-point method described by Odde and coworkers (29,110). The three point method estimates local curvatures according to the following equation:

$$\kappa = \left| \frac{d\theta(s)}{ds} \right| = \left| \frac{\Delta\theta}{(\Delta s_1 + \Delta s_2)/2} \right| \quad (4-1)$$

where κ is the local curvature estimate and $\theta(s)$ is the tangent angle as function of contour length s . The estimation of κ is done by calculating the angle θ between two coarse grained line segments and dividing by the average length of the line segments s_1 and s_2 (29,110). After local curvature estimates were calculated the root mean squared curvature was determined for the microtubule contour in question.

Results

Dynamics of Severed Microtubules

Recently Weitz and coworkers suggested that microtubules buckle as a result of compressive loading through a combination of experiments and modeling (55). The authors noted that microtubules buckle in much smaller wavelengths than would be expected from typical Euler buckling. Through both observation of polymerizing microtubules impinging on the cell periphery and the use of exogenous force the authors confirmed that the short wavelength buckles were the result of compressive loading. Through modeling and experiments the authors show that individual microtubules supported laterally by an elastic medium would exhibit the observed short wavelength buckles and could support larger compressive forces than previously thought, on the order of 100 pN (55). In this model the stored energy in both the bent microtubule and the surrounding elastic medium is balanced by energy generated by microtubule polymerization. These results and conclusions are in line with the hypothesis that microtubules bear compressive loads and serve as struts to balance acto-myosin generated tensional forces in the cell (57-59).

To determine if compressive stresses are significant components of the force balance on bent microtubules, we used femtosecond laser ablation to sever individual

microtubules. Upon severing a single microtubule both a new plus-ended and minus-ended microtubule fragment were formed. The newly formed fragments were distinguished by differences in depolymerization rate; previous studies (112) and our own results (Figure 4-1) have reported markedly larger depolymerization rates at the plus-end versus the minus-end. An example of the time dependent evolution of a severed buckled microtubule is illustrated in Figure 4-2A.

As result of the three-fold faster depolymerization kinetics the newly formed plus-ended microtubule (top portion) was observed to rapidly depolymerize along the original contour of the microtubule. Interestingly the newly formed minus-ended microtubule (bottom portion) was observed not to straighten as one would expect of a buckled filament under compression but rather increased in curvature. Time dependent shape traces from the images in Figure 4-2B illustrate the differing dynamics of the two newly freed ends. The root mean squared (RMS) curvature was found to increase with time in the newly formed minus-ended filament as illustrated in Figure 4-2C.

These differing behaviors of the newly formed filaments were found to be reproducible across many experiments; another example of a buckled microtubule at the cell periphery is included as Figure 4-2D. Overall, newly freed plus-ended microtubules were observed to rapidly depolymerize along the original contour without relaxing. Newly freed minus-ended microtubules were always observed to either preserve the original contour or increase in RMS curvature. The increase in RMS curvature varied from microtubule to microtubule but was not found to be correlated with the initial RMS curvature of the microtubule, Figure 4-3A. The change in RMS curvature

was also found not be correlated with the position in the cell as illustrated in Figure 4-3B.

In experiments where small increases in RMS curvature were observed (see Figure 4-4A), the slowly depolymerizing minus-ended filament was observed to depolymerize around the original contour. To determine if the relaxation kinetics of buckled microtubule were slower than the possible observation time before depolymerization (approximately 10-15 seconds), the experiments were performed with microtubules stabilized with Taxol treatment. A severed buckled microtubule in a Taxol treated cell was observed to hold the original contour for tens of seconds, Figure 4-4B.

Dynein Inhibition Alters the Dynamics of Severed Microtubules

Recently Odde and coworkers reported results suggesting that the molecular motor protein dynein may play a fundamental role in buckling microtubules (29). Through direct observation of buckling microtubules using fluorescent speckle microscopy they reported that during buckling microtubules move anterogradely, towards the cell periphery and the microtubule plus-end (29). To directly test the role of dynein in buckling and stabilizing bent microtubules individual microtubules were severed in cells transfected with the DsRed-CC1 plasmid. The DsRed-CC1 fusion protein competitively binds to dynein rendering it inactive. DsRed-CC1 inhibition of dynein activity was confirmed by immunostaining for the Golgi complex, see Figure 4-5A. In DsRed-CC1 transfected cells the Golgi complex was observed to diffusively surround the nucleus instead of being closely packed in control cells. This has been reported in the literature as a positive control for dynein inhibition (113).

In DsRed-CC1 transfected cells newly freed minus ends were not observed to hold the contour or increase in RMS curvature but rather were observed to straighten, Figure 4-5B. The straightening occurred in a relatively short time scale, 4 seconds for the case of the experiment in Figure 4-5B. This strikingly different result compared to normal cells occurred reproducibly in CC1 transfected cells over multiple experiments. On average, newly freed minus-ended microtubules in control cells were observed to increase in RMS curvature while in CC1 treated cells an average decrease in RMS curvature was observed, Figure 4-5C.

Discussion

The results of this chapter provide new insights into the forces generated by dynein on microtubules. Generally, buckled microtubules have been assumed to be under compressive loading due to forces generated by polymerization (55). Weitz and coworkers have proposed that buckled microtubules are supported laterally by deforming the surrounding elastic medium and as a result can support larger compressive forces (55). If microtubules are indeed under compression then one would expect that severed buckled microtubules to relax to release the stored bending energy. Furthermore if the surrounding elastic matrix is deformed this should increase the energy available for newly freed microtubules to straighten. Surprisingly when individual buckled microtubules were severed using a femtosecond laser both newly freed ends did not straighten. Rather both freed ends were observed to hold the original contour or actually increase in RMS curvature in the case of the minus-ended microtubule. The increase in curvature of the minus-ended microtubule suggests that dynein tangentially pulls on the microtubule as it walks toward the minus end. In the newly formed minus-ended microtubule, an ensemble of dynein molecules increases the bending energy of

by translating the freed end towards the plus-end. Recently Odde and coworkers reported that microtubules move anterogradely during buckling and hypothesized that minus-end directed motor immobilized to the cortical actin network could be responsible (29). Here we have provided direct experimental evidence that suggests that dynein provides the major contribution to the stress in microtubules. Furthermore severed microtubules in dynein inhibited cells were observed to straighten on time scales of approximately 4 seconds. This suggests that dynein provides the dominant frictional resistance to microtubule straightening.

These conclusions have interesting implications on the directionality of force that individual microtubules apply to the centrosome. Generally it has been assumed that buckled microtubules are under compression and exert pushing forces on the centrosome. Our experimental results lend themselves to a model where dynein generated stresses in the microtubule lead to tensile forces on the centrosome. In this model, a schematic is included as Figure 4-6, each microtubule is connected at the minus-end to the immovable centrosome and plus end is free to polymerize at the cell periphery. The centrosome is considered stationary because of the radial symmetry of the microtubules emanating outwards. An ensemble of dynein molecules immobilized on the cortical actin network bind to the microtubule and pull it taut against the centrosome. At some boundary point near the periphery the force in the microtubule switches from tensile to compressive as slack generated from polymerization is compressed against the cell periphery. The dynein motors exerting an anterograde force results in concentrating buckles near the cell periphery.

Summary of Findings

In summary our results have provided novel insight into the mechanics of microtubules and the role that dynein plays in these mechanics. Through relatively few but surprisingly informative experiments we can provide a qualitative picture of how dynein contributes to the force balance of a microtubule. Further quantitative analysis of the mechanics of dynein in microtubules and how these impact the centrosome are discussed in (114,115)

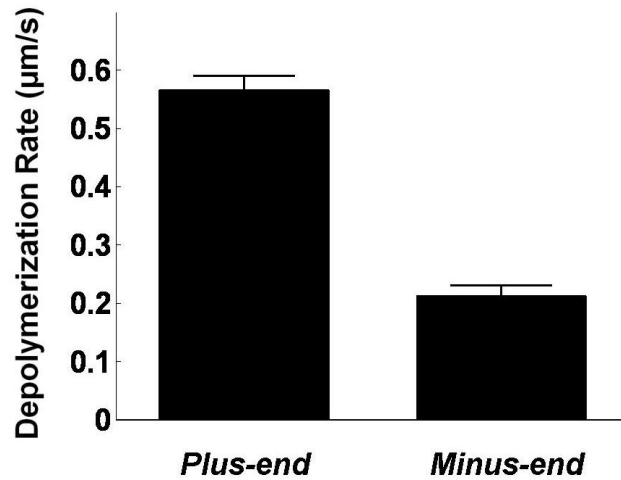


Figure 4-1. Depolymerization rates differ between plus-ended and minus-ended microtubules. The depolymerization rates of newly formed plus-ended and minus-ended was measured in severed microtubules. The plus-ended microtubule fragments were found to have a newly three fold higher depolymerization rate then minus-ended fragments.

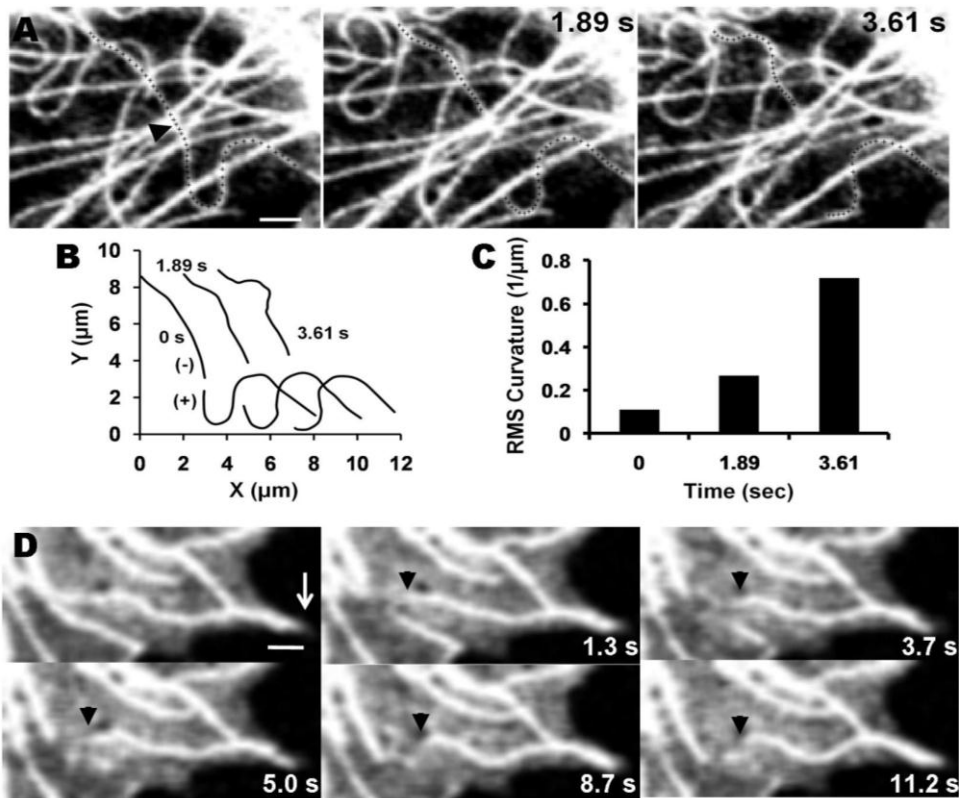


Figure 4-2. Minus-ended microtubule fragments increase in curvature after severing. (A) Upon severing (at the black arrow) microtubule (highlighted by crosses) were not observed to straighten. The quickly depolymerizing plus-ended fragment was observed to depolymerize along the original contour. Surprisingly the minus-ended fragment was observed to increase in curvature. Scale bar is 2 μm . (B) Shape traces of the two fragments created by severing illustrate the differing dynamics. (C) The RMS curvature was found to increase in the minus-ended fragment with time and in this example increased almost 7 fold. The plus-ended microtubule fragments were not observed to change in curvature. (D) Increases in the RMS curvature were found to be reproducible across many experiments. A representative example of experiments where a single microtubule, near the cell periphery (white arrow), was severed. Images show increased bending of minus-ended microtubules after severing (cut at black arrow). Note that the plus end depolymerizes but does not show a change in curvature. Scale bar is 1 μm .

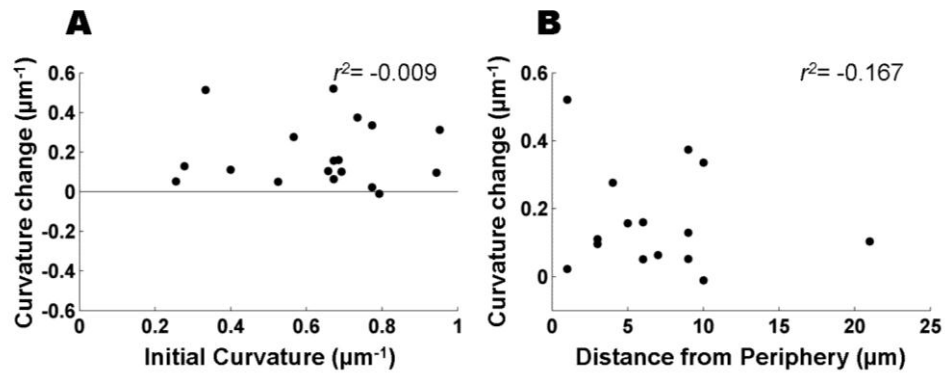


Figure 4-3. There is no correlation observed between the change in RMS curvature and either the initial RMS curvature or position of the microtubule. (A) The maximum change in RMS curvature for 18 experiments is plotted with respect to the initial curvature. In all experiments that were analyzed the change was positive and there exists no correlation. (B) The change in RMS curvature was plotted with respect to the shortest distance from the cut location to the cell periphery. No correlation was observed suggesting that the increase in curvature is location dependent.

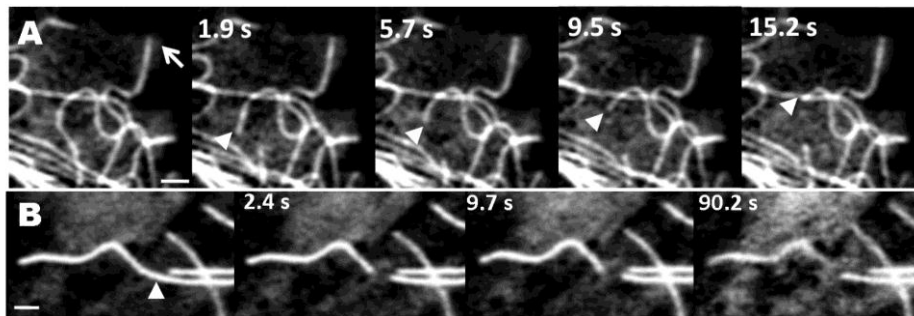


Figure 4-4. Bent microtubules are stable over significant time scales. (A) In experiments where minimal increases in curvature were observed, the minus-ended fragment depolymerized along the original contour. This data indicates that microtubules in living cells are pinned to the cytoplasm. Scale bar is 2 μm . (B) In taxol treated cells bent microtubules in severed minus-ended fragments were stable for tens of seconds. Scale Bar is 1 μm .

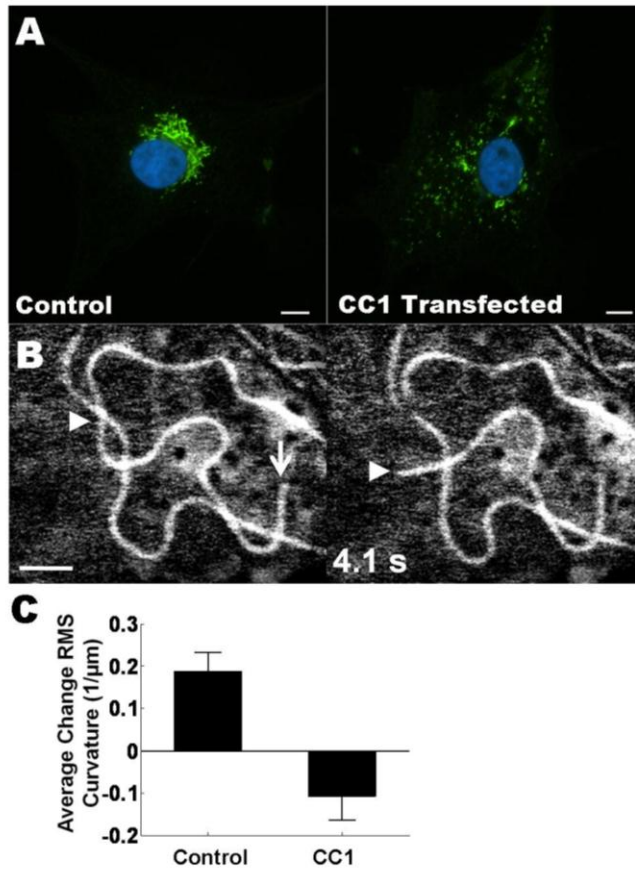


Figure 4-5. Severed microtubules in dynein inhibited cells were observed to straighten. (A) BCE cells were transfected with DsRed-CC1 to inhibit dynein. To confirm that dynein was inhibited the cells were immunostained for the Golgi complex. Control cells (left) show a compact Golgi complex (green) near the nucleus (blue), while DsRed-CC1 transfected cells (right) show a dispersed Golgi complex. Scale bars are 10 μm . (B) Severed minus-ended microtubules were observed to straighten in dynein-inhibited cells on a time scale of seconds. This suggests the dynein plays a fundamental role in providing friction for the microtubule. Scale bar is 2 μm . (C) On average newly formed minus-ended microtubules were observed to increase in RMS curvature while in dynein inhibited cells a decrease in RMS curvature was observed.

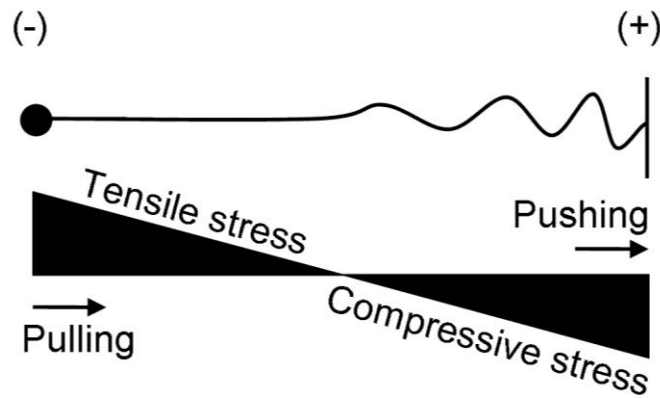


Figure 4-6. Cartoon schematic of proposed model of dynein force generation in microtubules. Microtubules that are buckled near the periphery are under compressive stress but pinned to the cytoplasm. The compressive stress results from the polymerizing plus-end tip impinging on the cell periphery. Along the length of the microtubule an ensemble of dynein molecules immobilized on the cortical actin network exert tensile forces that eventually overcome the compressive stresses. As result the individual microtubule exerts a net tensile force on the centrosome.

CHAPTER 5 CONCLUSIONS

Summary of Findings

The endothelium lines the vasculature and consists of a single monolayer of specialized endothelial cells. Endothelial cells are subjected to a continuous external mechanical stress due to blood flow. Endothelial cell function is critical for normal function of the vasculature and numerous pathologies have been shown to result from altered EC function including hypercholesterolemia, atherosclerosis, myocardial ischemia, and chronic heart failure (10). Past work has focused on pathological biochemical pathways (11). Increasingly, altered mechanical forces on endothelial cells is being studied as an initial inciting event in atherosclerosis (76). For example it has been shown that disturbed blood flow at vasculature bifurcations leads to the expression of pro-atherosclerotic genes in endothelial cells (76). Thus understanding the mechanisms by which endothelial cells sense mechanical forces and transduce them into intracellular response is critical for developing effective therapies. Furthermore endothelial cell mechanotransduction has broad implications for regenerative medicine which seeks to create engineered organs in vitro. Creating an adequate microvasculature in engineered tissues is a key challenge in regenerative medicine, and depends on tuning endothelial function through biochemical and mechanical factors (116). Future engineered tissues and tissue substitutes will have to recapitulate the in-vivo mechanical environment for proper endothelial cell function (117). The cytoskeleton is key to endothelial mechanotransduction. Therefore, this thesis focused on understanding the mechanical properties of the cytoskeleton in endothelial cells.

Specifically, our findings considerably advance fundamental understanding of the endothelial cytoskeleton as summarized below.

Stress Fiber Sarcomere Mechanics

Stress fibers are tension generating actomyosin structures in endothelial cells that allow endothelial cells to resist shear stresses from blood flow. Stress fibers are composed of linearly arranged contractile subunits referred to as sarcomeres. While theoretical mechanical models have been proposed for the stress fiber sarcomere, there exists no direct experimental evidence to support these sarcomere models.

Understanding the mechanics of the sarcomere is critical for a comprehensive mechanical model of the stress fiber. A novel technique of femtosecond laser ablation was applied to study the mechanics of stress fiber sarcomeres (92). Upon severing, stress fibers were observed to retract and the ends followed exponential kinetics as reported in the literature. Individual sarcomeres were observed to shorten in three distinct phases. These phases included a rapid contraction followed by a sustained linear contraction at constant speed and finally a steady state. Fully contracted stress fibers were shown to not release potential energy after treatment with myosin inhibitors. This result suggests that mechanical energy is stored in a fully contracted stress fiber. Based on these observations a mechanical model of the stress fiber sarcomere was proposed consisting of an elastic element in series with active myosin contraction that stops upon reaching a barrier. This sarcomere model lends itself to a stress fiber model where tension in the fiber is directly determined by myosin activity and that the force in a sarcomere is balanced by the neighboring sarcomeres

An interesting result from these experiments was the existence of an exponential distribution of linear contraction distances, the distance which the sarcomere contracted

at constant velocity. This finding suggests that the most probable state for a sarcomere is fully contracted at the barrier. Furthermore the reported viscoelastic retraction of the stress fiber as a whole can be adequately modeled with the exponential distribution of contraction distances. Sarcomere fluctuations were hypothesized as one possible explanation of this exponential distribution which were observed through live cell imaging and are discussed in the following section.

Sarcomere Dynamics in Endothelial Cells

The number of sarcomeres and sarcomere lengths dynamically change in the cell but the mechanisms by which these processes occur are not understood. Novel observations of sarcomere behavior in BCE cells were observed and interpreted through our proposed mechanical model. These observations suggest that sarcomeres undergo a variety of dynamic behaviors including fluctuations, generation at focal adhesions and consumption (118). These behaviors are not dependent on cell shape changes as they were observed in cells confined to micropatterned islands of fibronectin. The rate of generation at focal adhesions was shown to be independent of focal adhesion area, suggesting the rate of generation of sarcomeres is tension-independent. The fluctuating length of individual sarcomeres under constant tension is consistent with our mechanical model whereby sarcomere contraction/expansion speed, rather than sarcomere length, is modulated by tension.

Furthermore our results from the sarcomere contraction experiments were found to be consistent with our observations of sarcomere length fluctuations. These findings lend support to a model where the distribution of sarcomere lengths is determined by tension fluctuations. We demonstrated mathematically that the mechanical model

parameters of effective sarcomere diffusion coefficient and drift velocity can be obtained from only the autocorrelation function of sarcomere length fluctuations.

Our experimental results lead to a self-consistent mechanical model of the stress fiber that recapitulates observations in the literature, such as seemingly viscoelastic retraction of a severed fiber and inhomogeneous sarcomere contractions. Recently O'Shaughnessy and coworkers (119) published a model for a stress fiber contraction mechanism to capture the dynamics of stress fiber retraction reported by Kumar et al. (49). A key finding of this model was that substantial drag forces act on the severed fiber that could result from specific or non-specific interactions. Our model is consistent with this study in that we assume that the velocity of contraction of a sarcomere is proportional to the net tension on that sarcomere. Thus the proportionality constant could include contributions from both internal and external friction.

A recent study by Stelzer and coworkers suggests that stress fibers in epithelial cells and fibroblasts are connected to the ventral cellular surface (120). This result was based on the observation that in severed fibers retraction is limited to close proximity to the cut and that new focal adhesions were formed at the severed stress fiber end (120). This finding is not in line with our observations of stress fiber retraction in BCE cells where fibers were regularly observed to retract across the entirety of the cell, see Figure 2-6 for an example and to our knowledge focal adhesions were not formed at severed ends. These different findings suggest that that there may be cell type variations in stress fiber mechanics and that possible future studies in other types of endothelial cells could be useful.

Effects of Dynein on the Microtubule Force Balance

Microtubules are stiff biopolymers that emanate outwards from a central organizing center known as the centrosome. Microtubules are consistently observed to exist in bent conformations surrounding the cell periphery and are assumed to be under compression. Recently the minus-ended directed motor protein has been implicated in the buckling of microtubules. To determine the role of dynein in the force balance of microtubules, individual buckled microtubules were severed in living cells using femtosecond laser ablation. Surprisingly, buckled microtubules were not observed to straighten as would be expected for a compressed filament. Rather newly formed minus-ended microtubule fragments were observed to increase in bending energy. In dynein inhibited cells newly formed minus-ended microtubule fragments were observed to straighten releasing stored bending energy. These results suggest that dynein contributes significantly to the microtubule force balance. Furthermore this points to a model where microtubules are both under tension and compression. The net result of this model is that microtubules exert a tensile force on centrosome but are compressed at the cell periphery.

Future Work

The purpose of this section is to outline possible future studies to expand on our models and propose new future work based on the methods and ideas contained in this dissertation.

Biophysical Analysis of Mechanical Factors Leading to Atherosclerosis

Recently the role of altered shear stress has been implicated in the expression of pro-atherosclerotic genes in endothelial cells (76). Generally atherosclerotic plaques first form near vasculature bifurcations with disturbed blood flow patterns (121). Arterial

stiffening has been demonstrated to lead to vascular pathologies in the aging population (122). Both of these results suggest that understanding how endothelial cells react to a changing mechanical environment is crucial to understanding the pathology of atherosclerosis. Stress fibers are believed to play an integral role in the mechanotransduction in endothelial cells (121). A natural progression for the results in this work is to use our stress fiber model to determine how mechanical forces are transduced and affect the mechanics of the stress fiber. This is the first step in delineating how shear stress and arterial stiffening may incite atherosclerotic phenotypes. Furthermore gene-expression assays for pro-atherosclerotic genes will allow the determination of a biophysical phenotype for atherosclerosis. The experimental approach for this work would be to first characterize stress fiber mechanics under differing mechanical conditions and then determine expression levels of pro-atherosclerotic genes under matching mechanical conditions. A brief outline of the experimental procedure follows.

Our initial work on stress fiber mechanics was conducted on glass substrates with static flow conditions. To gain an understanding of how stress fibers transduce mechanical forces from the external environment we would culture cells on compliant poly-acrylamide gels or apply shear stresses to cells cultured on glass. Both of these methods have been well established in the literature (123,124). Sarcomere fluctuations and production from focal adhesions would be observed using time lapse microscopy to obtain model parameters discussed in this document. Samples of ECs exposed to matching mechanical stresses would be processed for RT-PCR quantification of pro-atherosclerotic gene expression. This would allow us to determine what mechanical

stresses result in maximum expression of pro-atherosclerotic genes and understand the state of the stress fiber network. A discussion of how model parameters may be affected by changes in cellular tension follows.

The impact of overall cell tension determined by external mechanical forces on the model parameters is not easily interpretable without experimental results. The external tension, T_{ext} , of the sarcomere is expected to change but it is not clear how the range of tension, T , that myosin in sarcomere can generate would be affected. If it is assumed that the range of T is fixed based on the stall force of myosin and constant for all conditions then for increasing T_{ext} the drift velocity v_d would be expected to decrease. Under the same assumption an increase in T_{ext} should lead to a decrease in the variance of tension fluctuations and thus velocity fluctuations, σ_v^2 , and as a result decrease D .

Force Transmission Between Endothelial Cells in a Mono-Layer

Vascular endothelial cells regulate the permeability of the endothelium by binding tightly to neighboring cells through specialized multi-protein cell-cell adhesion structures, tight junctions and adherens junctions (125). The endothelium must dynamically adjust in permeability to allow the passage of leukocytes from the blood stream to tissues (126). Actin stress fibers have been identified as key players in leukocyte transmigration and regulation of small-solute permeability (126). A recent paper by Ridley and coworkers suggests that stress fibers in adjacent cells are connected through specialized adhesions called adherens junctions (126). While this result suggests that there is mechanical continuity between endothelial cells, little is known about how forces are transmitted between cells and what the key molecular players are in this process. A possible direction for continuation of this work would be to

investigate force transmission mechanisms between endothelial cells in a mono-layer to gain a greater understanding of mechanisms for regulating paracellular permeability.

Recently poly-acrylamide hydrogels have been used to culture cells reliably on substrates of differing stiffness (123) and the inclusion of fluorescent micro-beads has allowed the researchers to calculate traction stresses that cells exert on the substrate (127). Using this technique along with femtosecond laser ablation a future study could determine how forces are transferred through cell-cell adhesions and the key molecular players. A brief description of a basic experiment for this study follows.

A mono-layer of ECs would be grown on a compliant poly-acrylamide substrate with embedded blue-green microspheres. The EC monolayer would then be transfected with EGFP- α -actinin and mCherry-VE-cadherin (a critical AJ protein). Single stress fibers would be ablated in one cell and the surrounding cells would be on image on three channels (red, green, and blue). This experiment would yield useful data about how forces are transmitted either between cells or to the substrate. Upon releasing tension in the severed stress fiber there are three possible outcomes. One of these is that all dissipated tension is transferred to the neighboring cells in which case the AJs and sarcomeres would translate. Another possible outcome is that all dissipated tension would be transferred to the substrate in which case the AJs and sarcomeres remain stationary and the microspheres translate. The third outcome is a hybrid of both of these in which some dissipated tension is transferred to both neighboring cells and the substrate. One would expect that for effective regulation of vascular permeability the majority of tension would be transmitted between cells. This would allow for the

endothelium to directly remodel itself to regulate permeability without wasting energy transmitting too much force to the substrate.

Further experiments could be done at differing substrate compliances to determine the affect of substrate compliance on force transfer between cells. The use of small interfering RNAs, si-RNA, has allowed researchers to knockdown the expression of specific proteins of interest. In this proposed study, si-RNAs directed towards AJ proteins could be used to determine the key molecular factors in efficient force transmission between cells. Overall this proposed project would contribute to the understanding of how the endothelium regulates permeability both mechanistically and by identifying proteins responsible for this functionality.

Mechanics of Myofilament Repair in C2C12 Myoblasts

Cellular damage occurs in mammalian cells during normal physiological functions as well as the result of local trauma (128). There exists cellular mechanisms for repair but these mechanisms be hindered in pathologies such as muscular dystrophy (129). A recent paper by Beckerle and coworkers suggests a zyxin mediated repair mechanism for stress fibers in non-muscle cells (91). Unfortunately there are no good model systems where one can create subcellular damage and follow the repair process. Recently we (92,115) and others (49) have used to femtosecond laser ablation to selectively sever individual cytoskeletal structures in BCE cells.

When myofilament bundles were severed with a femtosecond laser in C2C12 myoblasts transfected with EYFP- α -actinin the myofilaments were observed to repair themselves over the course of 1-2 minutes, Figure 5-1. After ablation of a small section of the actomyosin structure the newly severed ends were observed to pull apart as expected from other studies, Figure 5-1A. The wound was observed to be repaired

upon a local recruitment of EYFP- α -actinin, Figure 5-1B and C. After 150 seconds the myofilaments appear to have been completely repaired and resemble the same structure as before ablation, Figure 5-1D. To determine if this structure was still functioning and contractile the myofilaments were severed again in the same spot and minimal retraction was observed. These results suggest that a mechanism for myofilament repair exists in C2C12 myoblasts and that further studies are needed to determine the mechanics and key molecular factors for this mechanism.

This proposed project would be to first study the mechanics and kinetics of the repair mechanism in C2C12 myoblasts by ablating small sections and observing the dynamics of repair in cells transfected with EYFP- α -actinin. A second phase of this project would be to transfect cells with different sarcomeric fluorescent fusion proteins such as zyxin or VASP to determine if they play a role and their kinetics in the repair mechanism. Finally si-RNA knockdowns of key sarcomeric proteins will be used to determine key molecular players for this process. Overall this proposed project will enhance the collective understanding of the mechanics and molecular players for subcellular repair.

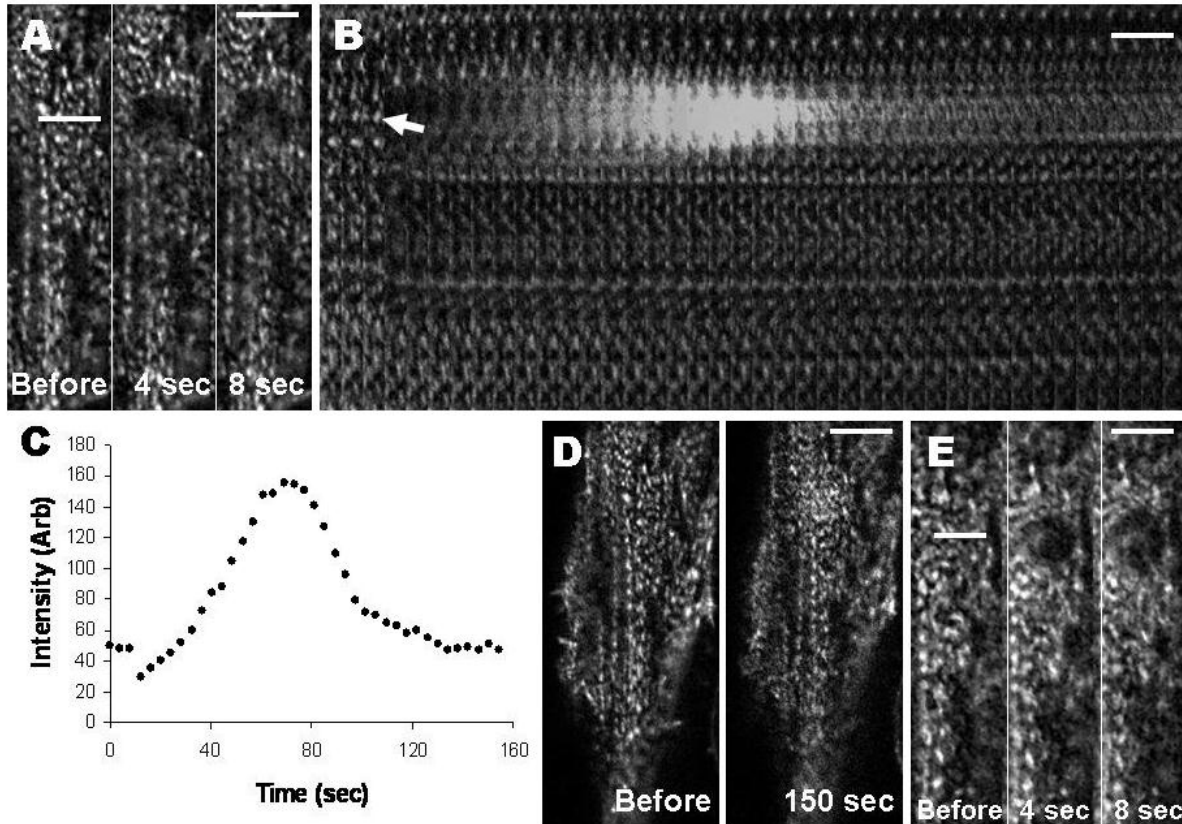


Figure 5-1. Severed myofilaments in C2C12 myoblasts display a repair mechanism. (A) Myofilaments in C2C12 myoblasts transfected with EYFP- α -actinin were severed using a femtosecond laser (white line) and upon severing the ends of fiber retracted away from each other. (B) A kymograph of a section of severed myofilament reveals that shortly after severing (at arrow) there is a transient increase in α -actinin concentration resulting in repair of the myofilaments. (C) The plot of α -actinin intensity with time in the severed myofilament. Intensity of α -actinin peaks at approximately 60 seconds after the cut. (D) Comparing images before cutting and at the end of the time series suggests that the sarcomeric structure has been repaired in the cut region. (E) Ablation (white line) in the repaired zone reveals that the myofilaments are again generating tension and functioning normally. Scale bars are 5 μ m

APPENDIX A MATLAB CODE FOR ANALYZING SARCOMERE DYNAMICS

Included in this appendix are the MATLAB programs used for most of the data analysis in this document. These programs were written as semi-automated methods to reproducibly analyze dynamics of cytoskeletal structures. Various image processing methods were included and are explained in the method sections of appropriate chapters.

Dense Body Tracking Software

This code was written and used for tracking dense bodies using a correlation based method but could be used for tracking any distinguishable feature. To improve accuracy a secondary centroid based correction method is also included. The code is semi-automated in that the user must select the feature in the initial frame and the code will compute positions for a user defined number of frames. The code calculates two separate coordinates for each frame which are calculated by distinct methods that are discussed in Chapter 2. For some applications a second program, discussed in A.2, can be run using the data generated from this program to ensure greater accuracy and refine the coordinate calculations.

```
%Start of densebodytracking.m

%This code tracks features in fluorescent images based on a correlation.

clear all
close all

%%%%%%%%%%%%%%%%%%%%%%%%%%%%%%%%%%%%%%%%%%%%%%%%%%%%%%%%%%%%%%%%%%%%%%%%
%set program parameters
n=1 ; %starting image for analysis
m=20; %ending image for analysis
threshold=.6; % Set thresh holding parameter. This will depend on the quality
of the images being analyzed and is best determined by trial and error for
the experiments being analyzed
```

```

num=3; % This is the size around the correlation peak to which we fit a
paraboloid. This parameter probably doesn't need to be changed and gives
accurate results
%Import image files and process them

matfiles =dir(fullfile('H:','Sept232010', 'cell8','ForPIV', '*.tiff'));
size_matfiles=size(matfiles);

for i =1:size_matfiles(1)

%temp_image = imread(matfiles(size_matfiles(1)-i+1).name); % Sometimes need
to reverse the sequence of images so that we start from bad photobleached
images and move on to better ones.

temp_image = imread(matfiles(i).name);
%temp_image=rgb2gray(temp_image);
temp_image = imadjust(temp_image, stretchlim(temp_image), [0 1]); %This line
contrast stretches the images to improve the ability to track
size_image=size(temp_image);

[p,q]=size(temp_image); %Use this code to add extra rows or columns to the
image. In cases where the feature approaches the image boarder this will help
prevent the tracking program from losing the feature
D=zeros(p+20,q+20);
D(11:p+10,11:q+10)=temp_image;
imag{i}=D;
imag{i}=temp_image;

end

%The user must select the feature in the initial frame numbered n.
[template, rectcrop] =imcrop(imag{n},[min(min(imag{n})),max(max(imag{n}))]);
rectcrop(1)=round(rectcrop(1));
rectcrop(2)=round(rectcrop(2));
width=round(rectcrop(3));
height=round(rectcrop(4));

[template, rectcrop]=imcrop(imag{n},[rectcrop(1),rectcrop(2),width,height]);
%To ensure accurate calculations the positions of the selection are rounded
to integer values and stored

save_template{1}=template;
save_rectcrop{1}=rectcrop;

%%%%%%%%%%%%%%%%%%%%%%%%%%%%%%%%%%%%%%%%%%%%%%%%%%%%%%%%%%%%%%%%%%%%%%%%

%First must calculate the centroid of the feature in the initial frame.
Because correlation only gives displacements this will be the starting point
for all coordinates that are calculated.

imag_cent{1}=template;
imag_max=max(max(imag_cent{1})); %Calculate maximum intensity value in
selection
imag_max=double(imag_max);

```

```

size_imag=size(template);

%Threshold selection to try eliminate noise or influence of neighboring
features
for i = 1:size_imag(1)
    for j = 1:size_imag(2)
        if imag_centr{1}(i,j)<imag_max*threshold
            imag_centr{1}(i,j)=0;
        else
            imag_centr{1}(i,j)=imag_centr{1}(i,j);
        end
    end
end

%Use built-in MATLAB functions to make a binary and calculate centroids
L = bwlabel(imag_centr{1});
s = regionprops(L, 'Centroid','Area');

%Determine the centroid with maximum area and then the corresponding centroid
cc = struct2cell(s);
asd=cc(1,:);
[maxval, I]=max(cell2mat(asd));

%Record position as initial positions. The variables (xcord,ycord) will refer
to positions determined using displacements calculated by correlation. The
variables (xCent, yCent) correspond to the centroid calculated in the region
of interest.
xcord(n)=s(I).Centroid(1)+rectcrop(1)-1;
ycord(n)=s(I).Centroid(2)+rectcrop(2)-1;
xCent(n)=xcord(n);
yCent(n)=ycord(n);

sizeofimage=size(imag{1});
imag1=imag;

%These lines black-out the surrounding areas of the selected feature and save
a modified series of images that can be used with the second program.
for i= 1:sizeofimage(1)

    if (i < rectcrop(2)-7)
        imag1{n}(i,:)=0;
    end

    if (i >rectcrop(2)+height+7)
        imag1{n}(i,:)=0;
    end

end

for i= 1:sizeofimage(2)

    if (i < rectcrop(1)-10)
        imag1{n}(:,i)=0;
    end
end

```

```

        if (i >rectcrop(1)+width+10)
            imag1{n}(:,i)=0;
        end
    end
end

%%%%%%%%%%%%%%%%%%%%%%%%%%%%%%%%%%%%%%%%%%%%%%%%%%%%%%%%%%%%%%%%%%%%%%%%
%Run the correlation code on each frame to update positions of the feature
and save coordinates

for g=n+1:m

%To prevent the code from jumping to similar neighboring features the code
blacks out the area far away from the feature. The user may need to adjust
these parameters to ensure that code tracks the correct particle.

    for i= 1:sizeofimage(1)

        if (i < (rectcrop(2))-10)
            imag1{g}(i,:)=0;
        end

        if (i >(rectcrop(2)+height+10))
            imag1{g}(i,:)=0;
        end
    end

    for i= 1:sizeofimage(2)

        if (i < rectcrop(1)-7)
            imag1{g}(:,i)=0;
        end

        if (i >rectcrop(1)+width+5)
            imag1{g}(:,i)=0;
        end
    end

    image=imag1{g};

    [c,corner_y(g),corner_x(g),xrefined,yrefined,cvalue]=process(template,image,num); %This gives the corner position in the ith image of the old template
    (i.e. from the i-1 image). The main code passes three things to the custom
    function "process" including the template from image i-1, image i and the
    parameter num.

    x_offset(g)=round(rectcrop(1))-corner_x(g);
    y_offset(g)=round(rectcrop(2))-corner_y(g);
    %These are the measured offsets between images and is used to update the
    positions

    cvalues(g)=cvalue;          %The correlation values are saved for troubleshooting
    if needed.

```

```

%Update positions are calculated with the offsets and stored
xcord(g)=xcord(g-1)-x_offset(g);
ycord(g)=ycord(g-1)-y_offset(g);

%Updated positions are used to determine the template position in image i
templatex=round(xcord(g)-width/2);
templatey=round(ycord(g)-height/2);

%Cropping new template for the next correlation
[template,rectcrop]=imcrop(imag{g},[templatex,templatey,width,height]);

%Refine the new template position by calculating the centroid
imag_centr{g}=template;
imag_max=max(max(imag_centr{g}));
imag_max=double(imag_max);
size_imag=size(template);
for i = 1:size_imag(1)
    for j = 1:size_imag(2)
        if imag_centr{g}(i,j)<imag_max*threshold
            imag_centr{g}(i,j)=0;
        else
            imag_centr{g}(i,j)=imag_centr{g}(i,j);
        end
    end
end
end

L = bwlabel(imag_centr{g});
s = regionprops(L, 'Centroid','Area');

cc = struct2cell(s);
asd=cc(1,:);
[maxval, I]=max(cell2mat(asd));

%Store the centroid position as a secondary position for each time frame
xCent(g)=s(I).Centroid(1)+rectcrop(1)-1;
yCent(g)=s(I).Centroid(2)+rectcrop(2)-1;

%Redefine the new template positions using the calculated centroid
templatex=round(xCent(g)-width/2);
templatey=round(yCent(g)-height/2);

%Recrop template
[template,rectcrop]=imcrop(imag{g},[templatex,templatey,width,height]);

%Save template and template coordinates
save_template{g}=template;
save_rectcrop{g}=rectcrop;

end

%Store 2D coordinates in one variable
Cent(:,1)=xCent;
Cent(:,2)=yCent;

```

```

cord(:,1)=xcord;
cord(:,2)=ycord;
%Create new series of images where area surrounding feature is blacked out
for Averaging Program
for g=n:m

    for i= 1:sizeofimage(1)

        if (i < (yCent(g)-((height)/2)))
            imag1{g}(i,:)=0;
        end

        if (i >(yCent(g)+((height)/2)))
            imag1{g}(i,:)=0;
        end

    end

    for i= 1:sizeofimage(2)

        if (i < (xCent(g)-((width)/2)))
            imag1{g}(:,i)=0;
        end
        if (i >(xCent(g)+((width)/2)))
            imag1{g}(:,i)=0;
        end

    end

end

end

%For each frame plot coordinates on image as well blacked out image
for l=n:m

    figure(1)
    subplot(2,1,1)
    imshow(imag{1},[min(min(imag{n})),max(max(imag{n}))])
    hold on
    plot(xcord(1), ycord(1), 'bx')
    hold on
    plot(xCent(1), yCent(1), 'rx')
    subplot(2,1,2)
    imshow(imag1{1},[min(min(imag{n})),max(max(imag{n}))])

end

save tracking

%End of densebodytracking.m

```

Correlation Processing Function

This function uses the built in MATLAB function `normxcorr2` to do the correlation calculation and then find the maximum. The integer values of the maximum are passed to the custom function `refineparaboloidnew` to refine to sub-pixel resolution.

```
%Start of process.m

%This function takes in a template and an image and returns the position of
the template in the new image.

function
[c,corner_y,corner_x,xrefined,yrefined,cvalue]=process(template,image,num)

    c = normxcorr2(template, image); % find correlation of dense body with
image

    [max_c, imax]= max (c(:)); %find the maximum correlation
    [ypk, xpk]= ind2sub(size(c), imax(1)); %Get coordinates for the maximum
    [xrefined,yrefined,cvalue]=refineparaboloidnew(ypk,xpk,num,c);

%This is the predicted sub-pixel position of the cropped rectangle in the
image at the next time point.
    corner_y=yrefined-size(template,1)+1;
    corner_x=xrefined-size(template,2)+1;
end

%End of process.m
```

Paraboloid Fitting Function

This function refines the peak found in the correlation spectrum by fitting it to a paraboloid function using the method of least squares. It returns the refined x and y peak positions (sub-pixel) as well as the correlation value at the peak.

```
%Start of refineparaboloidnew.m

function [xrefined,yrefined,cvalue,coeff]=refineparaboloidnew(ypk,xpk,num, c)

%Create matrices for the calculation based on the least squares method.
A=zeros(2,2);
B=zeros(2,1);
D=zeros(6,6);
E=zeros(6,1);
coeff=zeros(6,1);

Z=double(c);
```

```

%Populate matrices

for i = xpk-num:xpk+num
    for j = ypk-num:ypk+num
        D(1,1)=D(1,1)+1;
        D(1,2)=D(1,2)+i;
        D(2,1)=D(1,2);
        D(2,2)= D(2,2)+i*i;
        D(5,1)=D(2,2);
        D(1,5)=D(2,2);
        D(1,3)=D(1,3)+j;
        D(3,1)=D(1,3);
        D(3,3)= D(3,3)+j*j;
        D(1,6)=D(3,3);
        D(6,1)=D(3,3);
        D(2,3)=D(2,3)+i*j;
        D(3,2)=D(2,3);
        D(4,1)=D(2,3);
        D(1,4)=D(2,3);

        D(4,2)=D(4,2)+i*i*j;
        D(2,4)=D(4,2);
        D(5,3)=D(4,2);
        D(3,5)=D(4,2);

        D(5,2)=D(5,2)+i*i*i;
        D(2,5)=D(5,2);

        D(3,4)=D(3,4)+i*j*j;
        D(4,3)=D(3,4);
        D(6,2)=D(3,4);
        D(2,6)=D(3,4);

        D(4,4)=D(4,4)+i*i*j*j;

        D(3,6)=D(3,6)+j*j*j;
        D(6,3)=D(3,6);
        D(5,4)=D(5,4)+i*i*i*j;
        D(4,5)=D(5,4);
        D(6,4)=D(6,4)+i*j*j*j;
        D(4,6)=D(6,4);
        D(5,6)=D(4,4);
        D(6,5)=D(4,4);
        D(5,5)=D(5,5)+i*i*i*i;
        D(6,6)=D(6,6)+j*j*j*j;

        E(1)=E(1)+Z(j,i);

        E(2)=E(2)+Z(j,i)*i;
        E(3)=E(3)+Z(j,i)*j;
        E(4)=E(4)+Z(j,i)*i*j;
        E(5)=E(5)+Z(j,i)*i*i;
        E(6)=E(6)+Z(j,i)*j*j;
    end
end

```

```

    end
end

%Calculate the coefficients using least squares method
coeff=inv(D)*E;

%Find the maximum
A=[ 2*coeff(5) coeff(4)
    coeff(4) 2*coeff(6)];
B=[-coeff(2)
    -coeff(3)];

maxpositions=inv(A)*B;
xrefined=maxpositions(1);
yrefined=maxpositions(2);

%Check to make sure the maximum is reasonable and if not return integer
values
if (abs(xrefined-xpk)>3)
    xrefined=xpk;
end

if (abs(yrefined-ypk)>3)
    yrefined=ypk;
end

%Calculate cvalue at maximum from coefficients for troubleshooting if needed
cvalue=coeff(1)+(coeff(2)*xrefined)+(coeff(3)*yrefined)+(coeff(4)*xrefined*yr
efined)+(coeff(5)*xrefined*xrefined)+(coeff(6)*yrefined*yrefined);

%End of refineparaboloidnew.m

```

Averaging Position Software

This code was written and used for refining the positions of dense bodies by taking into account possible shape changes during the time series. To improve accuracy the correlation calculation was done using a template from each frame compared to every other frame. These positions are then all averaged to give an averaged position. The code is semi-automated in that the user must select the feature in the initial frame and the code will compute positions for a user defined number of frames. The code calculates two separate coordinates for each frame as mentioned in A.1.

```

%Start of averagingtracking.m

clear all
close all

```

```

%%%%%%%%%%%%%%%%%%%%%%%%%%%%%%%%%%%%%%%%%%%%%%%%%%%%%%%%%%%%%%%%%%%%%%%%
%set program parameters
n=1; %starting image for analysis
threshold=.6; % set thresh holding parameter
num=4; % this is the size around the correlation peak to which we fit a
paraboloid

%%%%%%%%%%%%%%%%%%%%%%%%%%%%%%%%%%%%%%%%%%%%%%%%%%%%%%%%%%%%%%%%%%%%%%%%
%Import file generated by Tracking Program

load tracking
n
k=m;

imag=imag1;

%Select template in first image like before
[template, rectcrop] =imcrop(imag1{1},[min(min(imag{1})),max(max(imag{1}))]);
rectcrop(1)=round(rectcrop(1));
rectcrop(2)=round(rectcrop(2));
width=round(rectcrop(3));
height=round(rectcrop(4));

%Round template positions for accurate coordinate calculations
[template, rectcrop]=imcrop(imag1{1},[rectcrop(1),rectcrop(2),width,height]);

%Store template and template position
save_template{1,1}=template;
save_rectcrop{1,1}=rectcrop;

%%%%%%%%%%%%%%%%%%%%%%%%%%%%%%%%%%%%%%%%%%%%%%%%%%%%%%%%%%%%%%%%%%%%%%%%
%Find the centroid of the particle in the first image
imag_cent{1}=template;
imag_max=max(max(imag_cent{1}));
imag_max=double(imag_max);
size_imag=size(template);
for i = 1:size_imag(1)
    for j = 1:size_imag(2)
        if imag_cent{1}(i,j)<imag_max*threshold
            imag_cent{1}(i,j)=0;
        else
            imag_cent{1}(i,j)=imag_cent{1}(i,j);
        end
    end
end
end

L = bwlabel(imag_cent{1});
s = regionprops(L, 'Centroid');
cc = struct2cell(s);
asd=cc(1,:);
[maxval, I]=max(cell2mat(asd));

xcord(1,1)=s(I).Centroid(1)+rectcrop(1)-1;

```

```

ycord(1,1)=s(I).Centroid(2)+rectcrop(2)-1;
xCent(1,1)=xcord(1,1);
yCent(1,1)=ycord(1,1);

%%%%%%%%%%%%%%%%%%%%%%%%%%%%%%%%%%%%%%%%%%%%%%%%%%%%%%%%%%%%%%%%%%%%%%%%
%Do Correlation for first particle to update positions of particles. This
will use the blacked out images created in the Tracking Program. Since there
are no neighboring particles the tracking should be very accurate. This also
creates a template for each frame which is later used.

for g=n:m

image=imag1{g};

[c,corner_y(g),corner_x(g),xrefined,yrefined,cvalue]=process(template,image,n
um); %This gives the corner position in the ith image of the old template
(i.e. from the i-1st image)

%This is the measured offset immediately between images
x_offset(1,g)=round(rectcrop(1))-corner_x(g);
y_offset(1,g)=round(rectcrop(2))-corner_y(g);

cvalues(1,g)=cvalue;

%Saves the correlation based positions for each frame based on correlation
with the first frame.
xcord(1,g)=xcord(1,n)-x_offset(1,g);
ycord(1,g)=ycord(1,n)-y_offset(1,g);

%Calculate new template position for each frame and crop update template.
templatex=round(xcord(1,g)-width/2);
templatey=round(ycord(1,g)-height/2);
[templatel,rectcrop1]=imcrop(imag{g},[templatex,templatey,width,height]);

%Find centroids of particle in each frame to use as starting position for
later correlation calculation

imag_centr{g}=templatel;
imag_max=max(max(imag_centr{g}));
imag_max=double(imag_max);
size_imag=size(templatel);
for i = 1:size_imag(1)
    for j = 1:size_imag(2)
        if imag_centr{g}(i,j)<imag_max*threshold
            imag_centr{g}(i,j)=0;
        else
            %imag_centr(i,j)=255;
            imag_centr{g}(i,j)=imag_centr{g}(i,j);
        end
    end
end

cc = struct2cell(s);
asd=cc(1,:);

```

```

[maxval, I]=max(cell2mat(asd));

%Store centroid calculate position for each frame
xCent(1,g)=s(1).Centroid(I)+rectcrop1(1)-1;
yCent(1,g)=s(1).Centroid(I)+rectcrop1(2)-1;

%Reset template positions with centroids and recrop templates
templatex=round(xCent(1,g)-width/2);
templatey=round(yCent(1,g)-height/2);
[templatel,rectcrop1]=imcrop(imag{g},[templatex,templatey,width,height]);

%Store templates and template coordinates for use later
save_template{1,g}=templatel;
save_rectcrop{1,g}=rectcrop1;

end

%Goes through and uses each template for correlation calculation against
every frame. For example use template from frame 2 against frames n through m
then move onto template from frame 3.

for h=n+1:k

%Load template and template coordinates for respective frame.
template=save_template{1,h};
rectcrop=save_rectcrop{1,h};
templatel =template;
rectcrop1 =rectcrop;

%Store coordinates calculated from first correlation calculation as reference
point.
xcord(h,h)=xcord(1,h);
ycord(h,h)=ycord(1,h);

for g=n:m

%Load blacked out image for frame g
image=imag1{g};

%Do correlation calculation as mentioned before
[c,corner_y(g),corner_x(g),xrefined,yrefined,cvalue]=process(template,image,num);

%Calculate offsets as mentioned before. This represents the displacement of
the particle from frame g to frame g
x_offset(h,g)=round(rectcrop(1))-corner_x(g);
y_offset(h,g)=round(rectcrop(2))-corner_y(g);
cvalues(h,g)=cvalue;

%Calculate coordinates of particle
xcord(h,g)=xcord(h,h)-x_offset(h,g);
ycord(h,g)=ycord(h,h)-y_offset(h,g);

```

```

end
end

%Calculate average positions and save as variables (xfinal,yfinal)
xsum=cumsum(xcord,1);
xfinal=xsum(k,:)/(m-n+1);

ysum=cumsum(ycord,1);
yfinal=ysum(k,:)/(m-n+1);

%Plot cloud of coordinates as well as averaged coordinates for each frame
for l=n:m

    figure(1)
    subplot(2,1,1)
    imshow(imag{1},[min(min(imag{n})),max(max(imag{n}))])
    hold on
    plot(xcord(:,l), ycord(:,l), 'bx')
    hold on
    plot(xfinal(l), yfinal(l), 'rx')

    subplot(2,1,2)
    imshow(imag1{1},[min(min(imag{n})),max(max(imag{n}))])
    hold on
    plot(xfinal(l), yfinal(l), 'rx')

end

%Save the results with as averagingdensebody# where # is the number of the
dense body. Name penultimate dense bodies 1, 2,...5.

save averagingdensebody#

%End of averagingtracking.m

```

Sarcomere Length Calculation

This code takes the positions of individual dense bodies calculated from the Averaging Position program and calculates sarcomere lengths with respect to time. The code is written to handle up to five dense bodies/ four sarcomeres at time but can be expanded to handle more. In the case where all sarcomeres are not adjacent ignore spacings calculated between non-adjacent dense bodies. For example if dense bodies 1,2, and 3 correspond to penultimate sarcomeres but dense bodies 4 and 5 are

somewhere else in the stress fiber ignore the spacing calculated between dense body 3 and 4.

```
%Start of sarcomerecalculator.m

clear all
close all

%Load files of all dense bodies tracked
load averagingdensebody1
load averagingdensebody2
load averagingdensebody3
load averagingdensebody4
load averagingdensebody5

%Input time increment
t=543;
%Input pixel size in microns
pixelsize=.14;

%%%%%%%%%%%%%%%%%%%%%%%%%%%%%%%%%%%%%%%%%%%%%%%%%%%%%%%%%%%%%%%%%%%%%%%%
%Import image files and process them to create image with all dense bodies
labeled

matfiles =dir(fullfile('C:', 'Documents and Settings', 'BobRussell', 'Desktop',
'CellCutFiles', 'Dec5Experiments', 'Cell13top', '*.tif'));
size_matfiles=size(matfiles);
for i =1:size_matfiles(1)
%temp_image = imread(matfiles(size_matfiles(1)-i+1).name); % we reverse the
sequence of images so that we start from 'bad particles' and move to
betterones
temp_image = imread(matfiles(i).name);
temp_image=rgb2gray(temp_image);
temp_image = imadjust(temp_image, stretchlim(temp_image), [0 1]);
size_image=size(temp_image);
[p,q]=size(temp_image); %Use this code to add extra rows or columns to
D=zeros(p,q+10);
D(1:p,6:q+5)=temp_image;
imag{i}=temp_image(:,10:size_image(2));
imag{i}=D;
end

%Calculate Spacings based on each coordinate set calculated in Averaging
program
spacing45=(((x4-x5).^2)+ ((y4-y5).^2)).^5)*pixelsize;
spacing34=(((x3-x4).^2)+ ((y3-y4).^2)).^5)*pixelsize;
spacing23=(((x2-x3).^2)+ ((y2-y3).^2)).^5)*pixelsize;
spacing12=(((x1-x2).^2)+ ((y1-y2).^2)).^5)*pixelsize;

%May want total spacing
%spacingtotal=(((x1-x3).^2)+ ((y1-y3).^2)).^5)*.14;

%Now calculate mean spacing which is what is used for model fitting and
further analysis
```

```

mean45=mean(spacing45,1);
mean34=mean(spacing34,1);
mean23=mean(spacing23,1);
mean12=mean(spacing12,1);

%Calculate mean positions for each dense body. This corresponds to xfinal and
yfinal from the averaging program but they will all be overwritten because
they all have the same name
x1mean=mean(x1,1);
x2mean=mean(x2,1);
x3mean=mean(x3,1);
x4mean=mean(x4,1);
x5mean=mean(x5,1);

y1mean=mean(y1,1);
y2mean=mean(y2,1);
y3mean=mean(y3,1);
y4mean=mean(y4,1);
y5mean=mean(y5,1);

%Calculate max and min spacing to generate plots
meanmax1=max(mean12(1:m))+.1;
meanmax2=max(mean23(1:m))+.1;
meanmax3=max(mean34(1:m))+.1;
meanmax4=max(mean45(1:m))+.1;
meanmin1=min(mean12(1:m))-.1;
meanmin2=min(mean23(1:m))-.1;
meanmin3=min(mean34(1:m))-.1;
meanmin4=min(mean45(1:m))-.1;

tmax=(m*t)/1000;

%Generate image at each time point with all tracked dense bodies labeled
for l=1:m

    figure (l)
    subplot(1,3,2)
    imshow(imag{l},[min(min(imag{l})),max(max(imag{l}))])
    hold on
    plot(x1mean(l), y1mean(l), 'bx')
    hold on
    plot(x2mean(l), y2mean(l), 'bx')
    hold on
    plot(x3mean(l), y3mean(l), 'bx')
    hold on
    plot(x4mean(l), y4mean(l), 'bx')
    hold on
    plot(x5mean(l), y5mean(l), 'bx')

end

%Plot spacings versus time for each sarcomere
for l=2:m

```

```

figure (m+1)
title('Sarcomere Spacing 1,2','FontSize',18)
hold on
plot(((1-2)*t)/1000,spacing12(1), 'bx')
xlabel('Time (sec)','FontSize',16)
ylabel('Spacing (microns)','FontSize',16)
axis([0 tmax meanmin1 meanmax1])

figure(m+2)
title('Sarcomere Spacing 2,3','FontSize',18)
hold on
plot(((1-2)*t)/1000,mean23(1), 'bx')
xlabel('Time (sec)','FontSize',16)
ylabel('Spacing (microns)','FontSize',16)
axis([0 tmax meanmin2 meanmax2])

figure(m+3)
title('Sarcomere Spacing 3,4','FontSize',18)
hold on
plot(((1-2)*t)/1000,mean34(1), 'bx')
xlabel('Time (sec)','FontSize',16)
ylabel('Spacing (microns)','FontSize',16)
axis([0 tmax meanmin3 meanmax3])

figure(m+4)
title('Sarcomere Spacing 4,5','FontSize',18)
hold on
plot(((1-2)*t)/1000,mean45(1), 'bx')
xlabel('Time (sec)','FontSize',16)
ylabel('Spacing (microns)','FontSize',16)
axis([0 tmax meanmin4 meanmax4])

end

save "experimentname"

%End of sarcomerecalculator.m

```

Model Fitting Code

Sarcomere trajectories after severing that displayed a sustained linear contraction were fit to a piecewise linear function corresponding to the mechanical model discussed in Chapter 2. In cases where an initial elastic contraction was observed but no linear contraction trajectories were fit to a single phase model. The MATLAB function

fminsearch was used to minimize the sum of the square of the residuals to fit parameters.

Four Parameter Fitting

```
%Start of fourparameterfitting.m

clear all
close all

%%%%%%%%%%%%%%%%%%%%%%%%%%%%%%%%%%%%%%%%%%%%%%%%%%%%%%%%%%%%%%%%%%%%%%%%
%Enter time data and spacing data as column vectors
%%%%%%%%%%%%%%%%%%%%%%%%%%%%%%%%%%%%%%%%%%%%%%%%%%%%%%%%%%%%%%%%%%%%%%%%
spacing=[ ];

t=[ ];

%Provide initial guesses for fminsearch. These are some characteristic values
that should lead to a reasonably solution
linear0=[.1, .9, .02, .1];
linear1=[.8, .1, .1];

%Perform optimization using fminsearch to get model parameters
[linearparam, linearval]
=fminsearch(@(linearparam)twolinefit(linearparam,t,spacing),linear0);

%Get variables from row vector linearparam
A=linearparam(1);
B=linearparam(2);
m=linearparam(3);
C=linearparam(4);

sized=length(t);

%Calculate F(x) in order to get the residuals
for i=1:sized

    if t(i)==0
        F1(i)=C+B+A-m*t(i);
    end

    if t(i)>0
        F1(i)=B+A-m*t(i);
    end

    F2(i)=B;

end

f=[F1',F2'];
g=max(f,[],2);
```

```

%These are the time dependent values of the fit function
linearspacing=g(:,1);

%Calculate the residuals
linearresid=spacing-linearspacing;

%Normalize the spacing as described in Chapter 2 and calculate the
dimensionless time
normspacing=(spacing-B)/A;
tc=A/m;
normtime=t/tc;

%Plot data along with line fit
figure (1)
plot(t, spacing, 'o')
hold on
plot(t, linearspacing,'b')

%Plot residuals
figure(2)
plot(t, linearresid, 'bx')

save "experimentname"

%End of fourparameterfitting.m

```

This is the function that describes the two phase linear model to which the data is fit.

```

%Start of twolinefit.m

function F =twolinefit(linearparam,t,spacing)

A = linearparam(1); B=linearparam(2); m= linearparam(3); C=linearparam(4);

sized=length(t);

%This loop creates the piecewise linear function.
for i=1:sized

    if t(i)==0
        F1(i)=C+B+A-m*t(i);
    end

    if t(i)>0
        F1(i)=B+A-m*t(i);
    end

    F2(i)=B;

end

f=[F1',F2'];
g=max(f,[],2);

```

```

F=g(:,1);

%Determine the sum of the square of the residuals, F, to minimize
SR=(spacing-F).^2;
SSR=cumsum(SR);
F=SSR(sizet);

```

```
%Start of twolinefit.m
```

Two Parameter Fitting

```
%Start of twoparameterfitting.m
```

```
clear all
close all
```

```

%%%%%%%%%%%%%%%%%%%%%%%%%%%%%%%%%%%%%%%%%%%%%%%%%%%%%%%%%%%%%%%%%%%%%%%%
%Enter time data and spacing data as column vectors
%%%%%%%%%%%%%%%%%%%%%%%%%%%%%%%%%%%%%%%%%%%%%%%%%%%%%%%%%%%%%%%%%%%%%%%%
t=[];

```

```
spacing=[];
```

```

%Provide initial guesses for fminsearch. These are some characteristic values
that should lead to a reasonably solution
guess=[.1,.9] ;

```

```

%Perform optimization using fminsearch to get model parameters
[zeroparam, linearval]=
fminsearch(@(zeroparam) zeroslopline(zeroparam,t,spacing),guess);

```

```
sizet=length(t);
```

```
C=zeroparam(1); B=zeroparam(2);
```

```

%Calculate F(x)
for i=1:sizet

```

```

    if t(i)==0
    F2(i)=C+B;
    end

```

```

    if t(i)>0
    F2(i)=B;
    end

```

```
end
```

```

%Plot data along with line fit
plot(t, spacing, 'o')
hold on
plot(t, F2,'k')

```

```
%Start of twoparameterfitting.m
```

This is the function that describes the single phase linear model to which the data is fit.

```
%Start of zeroslopline.m

function F =zeroslopline(zeroparam,t,spacing)

C=zerosparam(1); B=zerosparam(2);

sized=length(t);

%This loop creates the single phase function.
for i=1:sized

    if t(i)==0
        F2(i)=C+B;
    end

    if t(i)>0
        F2(i)=B;
    end

end

F=F2;

%Determine the sum of the square of the residuals, F, to minimize
SR=(spacing-F').^2;
SSR=cumsum(SR);
F=SSR(sized);

%End of zeroslopline.m
```

APPENDIX B MATLAB CODE FOR DETERMINING MICROTUBULE CURVATURE

These programs were written and used to determine the curvature of microtubules. The programs adapt previously published methods to estimate the coordinates of a microtubule to sub-pixel accuracy and then determines the root mean squared curvature of buckled microtubules.

Microtubule Tracing Code

This code is used to reliably and reproducibly determine the coordinates of a microtubule to sub-pixel accuracy. The code requires the user to trace the general shape of the microtubule by clicking the mouse. The methods used to refine the coordinates are discussed in the Materials and Methods section of Chapter 4. This code works on only one frame at a time but could be made semi-automated in the future.

```
%Start of microtubuletracing.m

clear all
close all

%Load series of images
matfiles=dir(fullfile('H:', 'MTBendingNoChange', 'May8cell122nucleuscut', 'crop',
 '*.tif'));

%Provide name for file
name='May8cell122nucleuscut ';
size_matfiles=size(matfiles);

%Loop to load all images
for i =1:size_matfiles(1)
temp_image = imread(matfiles(i).name);

%These lines allow for manipulations to the make the image appear better but
are probably not necessary for this application.

%temp_image=rgb2gray(temp_image);
%temp_image = imadjust(temp_image, stretchlim(temp_image), [0 1]);
size_image=size(temp_image);
[p,q]=size(temp_image); %Use this code to add extra rows or columns to
%imag{i}=temp_image(:,10:size_image(2));
imag{i}=temp_image;
end
```

```

%Determines size of line scan to fit Gaussian distribution for sub-pixel
position refining. Should not need to change this.
num=2;

%Subtract back ground and apply blur if needed. This uses a custom function
to try to enhance the image to make the microtubule easier to analyze.

%Set the frame number of interest in either line

%image=double(imag{4});
%[image2]=convolve(image);

%If not needed use this
image2=double(imag{4});

%The user must provide the program with an initial trace of the microtubule.
In the future it could be possible to have to program "detect" the
microtubule but the user input seems to work very well. Click with the mouse
along the microtubule contour as many times as possible. End the trace by
pressing the "enter" key.

figure(1)
imshow(image2, [min(min(image2)),max(max(image2))])

compimage=zeros(size_image);
[x,y]=ginput;

%The initial selected points are displayed on the microtubule for later
reference.
imshow(image2)
hold on
plot(x,y,'r*')

%This code will divide the microtubule into rectangular "slices" from the
user defined points. The height and width are calculated by determining the
distance between adjacent points and then adding an arbitrary number. The
slices are then cropped out with cropping coordinates determined by the
relative positions of adjacent y coordinates. All slices are saved.

for i=1:length(x)-1

    %calc height and width
    width(i)= round(abs(x(i)-x(i+1)))+4;
    height(i)=round(abs(y(i)-y(i+1)))+4;

    if y(i)<y(i+1)
        [template, rectcrop1] =imcrop(image2,[round(x(i)-2),round(y(i)-
2),width(i),height(i))]);
    else
        [template, rectcrop1] =imcrop(image2,[round(x(i)-2),round(y(i)-
height(i)+2),width(i),height(i))]);
    end
end

```

```

savetemp{i}=double(template);
saverect{i}=rectcrop1;

end

%All of the slices are compiled to make a composite image of only the
microtubule excluding the surrounding area

close all

for i=1:length(width)
dimen=saverect{i};
compimage(dimen(2):dimen(2)+dimen(4),dimen(1):dimen(1)+dimen(3))=savetemp{i};
end

%Display the composite image for later reference
figure(2)
imshow(compimage,[min(min(image2)),max(max(image2))])
hold on

%This is a rule based algorithm to check the alignment of microtubule. Does
cumsum on the rows and then columns and then compares the STD for the cumsums
and determines if horizontal or vertical. Larger STD should result if mtube
is aligned in opposite direction of cumsum. Seems to work very well. Save
direction of each point
count=1;
for i=1:length(width)
sizetemp=size(savetemp{i});
temp1=cumsum(savetemp{i},1);
sdtemp1=std(temp1(sizetemp(1),:));
temp2=cumsum(savetemp{i},2);
sdtemp2=std(temp2(:,sizetemp(2)));

    if sdtemp1>sdtemp2

        direction(i)=1;
    else
        direction(i)=2;
    end

%Now use directions to calculate the local maximum in a one pixel wide slice
either horizontally or vertically across the microtubule. Coordinates are
saved and counted
for j=2:sizetemp(direction(i))-1

    if direction(i)==1
        [C,I]=max(savetemp{i}(j,:));
        xc(j)=I;
        yc(j)=j;
        xcord(count)=I+saverect{i}(1)-1;
        ycord(count)=j+saverect{i}(2)-1;
        dirsave(count)=direction(i);
    else
        [C,I]=max(savetemp{i}(:,j));
    end
end

```

```

        xc(j)=j;
        yc(j)=I;
        xcord(count)=j+saverect{i}(1)-1;
        ycord(count)=I+saverect{i}(2)-1;
        dirsave(count)=direction(i);
    end

    count=count+1;
end

clear j

end

%Display points refined by maxima
figure(3)
imshow(image2, [min(min(image2)),max(max(image2))])
hold on
plot(xcord,ycord,'xb')

%The initial point refinement will result in many duplicate points as a
result of the overlapping slices. This code is meant to eliminate the
duplicates and spurious points. First all points are sorted with respect to
the x direction which requires that the microtubule to appear as a function
y=f(x)

cords=[xcord', ycord', dirsave'];
cords=sortrows(cords);
xcord=cords(:,1);
ycord=cords(:,2);
dirsave=cords(:,3);

count2=1;
xcordnew=xcord(1);
ycordnew=ycord(1);
dirsave=dirsave(1);
for i=2:length(xcord)

    %First check if the x coordinate is unique. If it is unique but the ycord
is not this is most likely a flat portion of the microtubule where the y
position can be refined to subpixel accuracy.
    if xcord(i)~=xcord(i-1)

        if (ycord(i)==ycord(i-1))&&(dirsave(i)==2)
            count2=count2+1;
            xcordnew(count2)=xcord(i);
            ycordnew(count2)=ycord(i);
            dirsave(count2)=dirsave(i);
        else
            count2=count2+1;
            xcordnew(count2)=xcord(i);
            ycordnew(count2)=ycord(i);
            dirsave(count2)=dirsave(i);
        end
    end
end
else

```

```

%If the xcord is not unique and ycord is then save these points. This is
sharply sloped portion of the microtubule where the x positions can be
refined to subpixel accuracy
    if (xcord(i)==xcord(i-1))&& (ycord(i)~=ycord(i-1))&&(dirsave(i)==1)

        count2=count2+1;
        xcordnew(count2)=xcord(i);
        ycordnew(count2)=ycord(i);
        dirsavenew(count2)=dirsave(i);

    end
end
end

%It is necessary to check that the direction associated with each point is
optimal. This code checks each point by determining difference between the
intensity at the maximum and the average intensity of the pixels two away in
both the x and y direction. For a point located in horizontal part of a
microtubule there should be a larger difference in the vertical direction
then the horizontal. If these values are too close to each other then the
direction is undetermined and is noted.

for i=1:length(xcordnew)

    tempinten=image2(ycordnew(i),xcordnew(i));

    xslope=(image2(ycordnew(i),xcordnew(i)+2)+image2(ycordnew(i),xcordnew(i)-2))//;
    xslope=tempinten-xslope;
    yslope=(image2(ycordnew(i)+2,xcordnew(i))+image2(ycordnew(i)-2,xcordnew(i)))/;
    yslope=tempinten-yslope;

    if (xslope/yslope<.05 || yslope/xslope<.05)
        dirsavenew(i)=3;
    else
        if yslope< xslope
            dirsavenew(i)=1;
        else
            dirsavenew(i)=2;
        end
    end
end
end

%Use the directions to fit a Gaussian across the microtubule on single pixel
slice to get sub-pixel resolution

%Create a kernel for the Gaussian fitting and define slice size to send to
fitting function.
kernell=zeros(2*num+1,1);
imagepart=kernell;
kernell=(-num:1:num);

%Start display to show direction of "slice" for each point
figure(4)

```

```

hold on
imshow(image2, [min(min(image2)),max(max(image2))])
hold on

clear i

%Perform Gaussian fitting across microtubule to refine coordinates to
subpixel accuracy. If direction was undefined as mentioned above then fit in
both directions and average offsets.
for i=1:length(xcordnew)

    xguess=xcordnew(i);
    yguess=ycordnew(i);
    dir=dirsavenew(i);

    if dir==2

        plot([xguess, xguess], [yguess-num, yguess+num])
        imagepart=image2(yguess-num:yguess+num,xguess);
        [offset]=gaussfit(imagepart,kernel1,num);

        yfinal(i)=yguess+offset;
        xfinal(i)=xguess;

    end

    if dir==1

        plot([xguess-num, xguess+num], [yguess, yguess])
        imagepart=image2(yguess,xguess-num:xguess+num);

        [offset]=gaussfit(imagepart,kernel1,num);

        xfinal(i)=xguess+offset;
        yfinal(i)=yguess;

    end

    if dir==3
        plot([xguess-num, xguess+num], [yguess, yguess],'g')
        plot([xguess, xguess], [yguess-num, yguess+num],'g')

        imagepart1=image2(yguess-num:yguess+num,xguess);
        [offset1]=gaussfit(imagepart1,kernel1,num);
        imagepart=image2(yguess,xguess-num:xguess+num);
        [offset]=gaussfit(imagepart,kernel1,num);
        xfinal(i)=xguess+offset/2;
        yfinal(i)=yguess+offset1/2;
    end
end

end

```

```

%cords1=[xfinal', yfinal'];
%cords1=sortrows(cords1);
%xfinal=cords1(:,1);
%yfinal=cords1(:,2);

xfinaln=xfinal;
yfinaln=yfinal;

%Plot final coordinates
figure(4)

    hold on
    plot(xfinaln,yfinaln,'rx')

%Save data to pass to next program to calculate Bending Energy or Root Mean
Squared Curvature

save cord image2 compimage name xfinaln yfinaln

%End of microtubuletracing.m

```

Linear Gaussian Fitting Function

This function refines the coordinates of the maximum of the correlation function to sub-pixel accuracy by fitting a Gaussian to a line slice across the microtubule.

```

%Start of gaussfit.m

%This function refines the peak found in the correlation spectrum by fitting
it to a Gaussian function. It returns the refined x and y peak positions (sub-
pixel) as well as the correlation value at the peakfunction
[yrefined]=gaussfit(imagepart, kernel)

%Create matrices for the calculation
function [offset]=gaussfit(imagepart, kernell1, num)

A=zeros(2,2);
B=zeros(2,1);
D=zeros(3,3);
E=zeros(3,1);
coeff=zeros(6,1);

Z=log(imagepart);

%Populate matrix for the least squares fitting
for i = 1:length(kernell1)
    D(1,1)=D(1,1)+1;
    D(1,2)=D(1,2)+kernell1(i);
    D(2,1)=D(1,2);
    D(2,2)= D(2,2)+kernell1(i)*kernell1(i);

```

```

D(3,1)=D(2,2);
D(1,3)=D(2,2);
D(3,2)=D(3,2)+kernel1(i)*kernel1(i)*kernel1(i);
D(2,3)=D(3,2);
D(3,3)=D(3,3)+kernel1(i)*kernel1(i)*kernel1(i)*kernel1(i);

E(1)=E(1)+Z(i);
E(2)=E(2)+Z(i)*kernel1(i);
E(3)=E(3)+Z(i)*kernel1(i)*kernel1(i);
end

coeff=inv(D)*E;

%Determine sub-pixel offset
offset=coeff(2)/(-2*coeff(3));

%Check the offset to make sure it is reasonable
if abs(offset)>num
    offset=0;
end

end

%End of gaussfit.m

```

Curvature and Bending Energy Calculation Code

This code was written to calculate the curvature and the bending energy/ root mean squared curvature of microtubules from traces generated from the program B.1.

This code uses a previously published method known as the three point method to calculate curvature.

```

%Start of curvaturecalculator.m

%This program is used to calculate the Bending Energy or the RMS curvature
from the microtubule trace calculated in the Microtubule Tracer

close all
clear all

%Load coordinates generated from Microtubule Tracer
load cord

%Sort the coordinates by x one last time
cords1=[xfinaln', yfinaln'];
cords1=sortrows(cords1);
xfinaln=cords1(:,1);
yfinaln=cords1(:,2);

```

```

%Smooth the coordinates to eliminate short range oscillations from imaging
uncertainty but preserve long range microtubule buckles.
x=smooth(xfinaln,5);
y=smooth(yfinaln,5);

%Specify the number of points for line segment
nump=4;

%Display image of microtubule
figure (1)
imshow(image2, [min(min(image2)),max(max(image2))])
hold on

%Calculate segment lengths and slopes. Store starting and ending positions of
each lines segment. Also count the line segments
count=1
for i=1:nump:length(x)-nump

    s(count)=sqrt((x(i)-x(i+nump))^2+(y(i)-y(i+nump))^2);
    m(count)=(y(i+nump)-y(i))/(x(i+nump)-x(i));

    xpoint(count,:)=[x(i), x(i+nump)];
    ypoint(count,:)=[y(i),y(i+nump)];

    count=count+1;

end

%Plot the line segments on the microtubule
plot(xpoint,ypoint,'r-')
plot(xpoint,ypoint,'b*')

%Calc curvature with three point method
for i=1:length(s)-1

    theta(i)=atan((m(i+1)-m(i))/(1+(m(i)*m(i+1))));
    curve2(i)=abs(theta(i)/((s(i)+s(i+1))/2));
end

%Sum all segment lengths
scum=cumsum(s);

%Plot curvature a function of arclength
figure(2)
plot(scum(2:length(scum)),curve2, 'rx-')
xlabel('arclength s, pixels'), ylabel('curvature')

arcleng=scum(2:length(scum));

%Calculate Bending Energy by numerically integrating curvature squared.

```

```
BendingEnergy=trapz(arcleng,curve2.^2)
Enperleng=BendingEnergy/arcleng(length(arcleng))
```

```
save(name)
```

```
%End of curvaturecalculator.m
```

LIST OF REFERENCES

1. Cines, D. B., E. S. Pollak, C. A. Buck, J. Loscalzo, G. A. Zimmerman, R. P. McEver, J. S. Pober, T. M. Wick, B. A. Konkle, B. S. Schwartz, E. S. Barnathan, K. R. McCrae, B. A. Hug, A. M. Schmidt, and D. M. Stern. 1998. Endothelial cells in physiology and in the pathophysiology of vascular disorders. *Blood* 91:3527-3561.
2. Prasain, N. and T. Stevens. 2009. The actin cytoskeleton in endothelial cell phenotypes. *Microvasc Res* 77:53-63.
3. Aird, W. C. 2003. Endothelial cell heterogeneity. *Crit Care Med* 31:S221-230.
4. Aird, W. C. 2008. Endothelium in health and disease. *Pharmacol Rep* 60:139-143.
5. Gloor, S. M., M. Wachtel, M. F. Bolliger, H. Ishihara, R. Landmann, and K. Frei. 2001. Molecular and cellular permeability control at the blood-brain barrier. *Brain Res Brain Res Rev* 36:258-264.
6. Aird, W. C. 2007. Phenotypic heterogeneity of the endothelium: I. Structure, function, and mechanisms. *Circ Res* 100:158-173.
7. Gebb, S. and T. Stevens. 2004. On lung endothelial cell heterogeneity. *Microvasc Res* 68:1-12.
8. Ofori-Aquah, S. F., J. King, N. Voelkel, K. L. Schaphorst, and T. Stevens. 2008. Heterogeneity of barrier function in the lung reflects diversity in endothelial cell junctions. *Microvasc Res* 75:391-402.
9. Dudek, S. M. and J. G. Garcia. 2001. Cytoskeletal regulation of pulmonary vascular permeability. *J Appl Physiol* 91:1487-1500.
10. Drexler, H. and B. Hornig. 1999. Endothelial dysfunction in human disease. *J Mol Cell Cardiol* 31:51-60.
11. Wojciak-Stothard, B. and A. J. Ridley. 2002. Rho GTPases and the regulation of endothelial permeability. *Vascul Pharmacol* 39:187-199.
12. Gimbrone, M. A., Jr., T. Nagel, and J. N. Topper. 1997. Biomechanical activation: an emerging paradigm in endothelial adhesion biology. *J Clin Invest* 99:1809-1813.
13. Chien, S., S. Li, and Y. J. Shyy. 1998. Effects of mechanical forces on signal transduction and gene expression in endothelial cells. *Hypertension* 31:162-169.
14. Nehls, V. and D. Drenckhahn. 1991. Demonstration of actin filament stress fibers in microvascular endothelial cells in situ. *Microvasc Res* 42:103-112.

15. Barbee, K. A., T. Mundel, R. Lal, and P. F. Davies. 1995. Subcellular distribution of shear stress at the surface of flow-aligned and nonaligned endothelial monolayers. *Am J Physiol* 268:H1765-1772.
16. Galbraith, C. G., R. Skalak, and S. Chien. 1998. Shear stress induces spatial reorganization of the endothelial cell cytoskeleton. *Cell Motil Cytoskeleton* 40:317-330.
17. Steinmetz, M. O., D. Stoffler, A. Hoenger, A. Bremer, and U. Aebi. 1997. Actin: from cell biology to atomic detail. *J Struct Biol* 119:295-320.
18. Welch, M. D., A. Mallavarapu, J. Rosenblatt, and T. J. Mitchison. 1997. Actin dynamics in vivo. *Curr Opin Cell Biol* 9:54-61.
19. Matsudaira, P. 1994. Actin crosslinking proteins at the leading edge. *Semin Cell Biol* 5:165-174.
20. Small, J. V., K. Rottner, I. Kaverina, and K. I. Anderson. 1998. Assembling an actin cytoskeleton for cell attachment and movement. *Biochim Biophys Acta* 1404:271-281.
21. Katoh, K., Y. Kano, M. Masuda, H. Onishi, and K. Fujiwara. 1998. Isolation and contraction of the stress fiber. *Mol Biol Cell* 9:1919-1938.
22. Balaban, N. Q., U. S. Schwarz, D. Riveline, P. Goichberg, G. Tzur, I. Sabanay, D. Mahalu, S. Safran, A. Bershadsky, L. Addadi, and B. Geiger. 2001. Force and focal adhesion assembly: a close relationship studied using elastic micropatterned substrates. *Nat Cell Biol* 3:466-472.
23. Geiger, B. and A. Bershadsky. 2001. Assembly and mechanosensory function of focal contacts. *Curr Opin Cell Biol* 13:584-592.
24. Brakebusch, C. and R. Fassler. 2003. The integrin-actin connection, an eternal love affair. *Embo J* 22:2324-2333.
25. Wong, A. J., T. D. Pollard, and I. M. Herman. 1983. Actin filament stress fibers in vascular endothelial cells in vivo. *Science* 219:867-869.
26. Lee, T. Y. and A. I. Gotlieb. 2003. Microfilaments and microtubules maintain endothelial integrity. *Microsc Res Tech* 60:115-127.
27. Moritz, M. and D. A. Agard. 2001. Gamma-tubulin complexes and microtubule nucleation. *Curr Opin Struct Biol* 11:174-181.
28. Wade, R. H. 2009. On and around microtubules: an overview. *Mol Biotechnol* 43:177-191.

29. Bicek, A. D., E. Tuzel, A. Demtchouk, M. Uppalapati, W. O. Hancock, D. M. Kroll, and D. J. Odde. 2009. Anterograde microtubule transport drives microtubule bending in LLC-PK1 epithelial cells. *Mol Biol Cell* 20:2943-2953.
30. Luders, J. and T. Stearns. 2007. Microtubule-organizing centres: a re-evaluation. *Nat Rev Mol Cell Biol* 8:161-167.
31. White, G. E., M. A. Gimbrone, Jr., and K. Fujiwara. 1983. Factors influencing the expression of stress fibers in vascular endothelial cells in situ. *J Cell Biol* 97:416-424.
32. Drenckhahn, D. and J. Wagner. 1986. Stress fibers in the splenic sinus endothelium in situ: molecular structure, relationship to the extracellular matrix, and contractility. *J Cell Biol* 102:1738-1747.
33. Kim, D. W., B. L. Langille, M. K. Wong, and A. I. Gotlieb. 1989. Patterns of endothelial microfilament distribution in the rabbit aorta in situ. *Circ Res* 64:21-31.
34. Kim, D. W., A. I. Gotlieb, and B. L. Langille. 1989. In vivo modulation of endothelial F-actin microfilaments by experimental alterations in shear stress. *Arteriosclerosis* 9:439-445.
35. Pellegrin, S. and H. Mellor. 2007. Actin stress fibres. *J Cell Sci* 120:3491-3499.
36. Lazarides, E. 1975. Tropomyosin antibody: the specific localization of tropomyosin in nonmuscle cells. *J Cell Biol* 65:549-561.
37. Lazarides, E. and K. Burridge. 1975. Alpha-actinin: immunofluorescent localization of a muscle structural protein in nonmuscle cells. *Cell* 6:289-298.
38. Weber, K. and U. Groeschel-Stewart. 1974. Antibody to myosin: the specific visualization of myosin-containing filaments in nonmuscle cells. *Proc Natl Acad Sci U S A* 71:4561-4564.
39. Sanger, J. W., B. Mittal, and J. M. Sanger. 1984. Interaction of fluorescently-labeled contractile proteins with the cytoskeleton in cell models. *J Cell Biol* 99:918-928.
40. Cramer, L. P., M. Siebert, and T. J. Mitchison. 1997. Identification of novel graded polarity actin filament bundles in locomoting heart fibroblasts: implications for the generation of motile force. *J Cell Biol* 136:1287-1305.
41. Wang, K., J. F. Ash, and S. J. Singer. 1975. Filamin, a new high-molecular-weight protein found in smooth muscle and non-muscle cells. *Proc Natl Acad Sci U S A* 72:4483-4486.

42. Adams, J. C. 1995. Formation of stable microspikes containing actin and the 55 kDa actin bundling protein, fascin, is a consequence of cell adhesion to thrombospondin-1: implications for the anti-adhesive activities of thrombospondin-1. *J Cell Sci* 108 (Pt 5):1977-1990.
43. Price, C. J. and N. P. Brindle. 2000. Vasodilator-stimulated phosphoprotein is involved in stress-fiber and membrane ruffle formation in endothelial cells. *Arterioscler Thromb Vasc Biol* 20:2051-2056.
44. Langanger, G., M. Moeremans, G. Daneels, A. Sobieszek, M. De Brabander, and J. De Mey. 1986. The molecular organization of myosin in stress fibers of cultured cells. *J Cell Biol* 102:200-209.
45. Turnacioglu, K. K., J. W. Sanger, and J. M. Sanger. 1998. Sites of monomeric actin incorporation in living PtK2 and REF-52 cells. *Cell Motil Cytoskeleton* 40:59-70.
46. Kreis, T. E. and W. Birchmeier. 1980. Stress fiber sarcomeres of fibroblasts are contractile. *Cell* 22:555-561.
47. Sanger, J. M. and J. W. Sanger. 1980. Banding and polarity of actin filaments in interphase and cleaving cells. *J Cell Biol* 86:568-575.
48. Deguchi, S., T. Ohashi, and M. Sato. 2006. Tensile properties of single stress fibers isolated from cultured vascular smooth muscle cells. *J Biomech* 39:2603-2610.
49. Kumar, S., I. Z. Maxwell, A. Heisterkamp, T. R. Polte, T. P. Lele, M. Salanga, E. Mazur, and D. E. Ingber. 2006. Viscoelastic retraction of single living stress fibers and its impact on cell shape, cytoskeletal organization, and extracellular matrix mechanics. *Biophys J* 90:3762-3773.
50. Lu, L., S. J. Oswald, H. Ngu, and F. C. Yin. 2008. Mechanical properties of actin stress fibers in living cells. *Biophys J* 95:6060-6071.
51. Peterson, L. J., Z. Rajfur, A. S. Maddox, C. D. Freel, Y. Chen, M. Edlund, C. Otey, and K. Burridge. 2004. Simultaneous stretching and contraction of stress fibers in vivo. *Molecular Biology of the Cell* 15:3497-3508.
52. Besser, A. and U. S. Schwarz. 2007. Coupling biochemistry and mechanics in cell adhesion: a model for inhomogeneous stress fiber contraction. *New Journal of Physics* 9:-.
53. Stachowiak, M. R. and B. O'Shaughnessy. 2008. Kinetics of stress fibers. *New Journal of Physics* 10:-.

54. Gittes, F., B. Mickey, J. Nettleton, and J. Howard. 1993. Flexural rigidity of microtubules and actin filaments measured from thermal fluctuations in shape. *J Cell Biol* 120:923-934.
55. Brangwynne, C. P., F. C. MacKintosh, S. Kumar, N. A. Geisse, J. Talbot, L. Mahadevan, K. K. Parker, D. E. Ingber, and D. A. Weitz. 2006. Microtubules can bear enhanced compressive loads in living cells because of lateral reinforcement. *J Cell Biol* 173:733-741.
56. Dogterom, M. and B. Yurke. 1997. Measurement of the force-velocity relation for growing microtubules. *Science* 278:856-860.
57. Ingber, D. E. 1993. Cellular tensegrity: defining new rules of biological design that govern the cytoskeleton. *J Cell Sci* 104 (Pt 3):613-627.
58. Ingber, D. E. 1998. The architecture of life. *Sci Am* 278:48-57.
59. Stamenovic, D., S. M. Mijailovich, I. M. Tolic-Norrelykke, J. Chen, and N. Wang. 2002. Cell prestress. II. Contribution of microtubules. *Am J Physiol Cell Physiol* 282:C617-624.
60. Brangwynne, C. P., F. C. MacKintosh, and D. A. Weitz. 2007. Force fluctuations and polymerization dynamics of intracellular microtubules. *Proc Natl Acad Sci U S A* 104:16128-16133.
61. Waterman-Storer, C. M. and E. D. Salmon. 1997. Actomyosin-based retrograde flow of microtubules in the lamella of migrating epithelial cells influences microtubule dynamic instability and turnover and is associated with microtubule breakage and treadmilling. *J Cell Biol* 139:417-434.
62. Zhou, F. Q., C. M. Waterman-Storer, and C. S. Cohan. 2002. Focal loss of actin bundles causes microtubule redistribution and growth cone turning. *J Cell Biol* 157:839-849.
63. Koonce, M. P., J. Kohler, R. Neujahr, J. M. Schwartz, I. Tikhonenko, and G. Gerisch. 1999. Dynein motor regulation stabilizes interphase microtubule arrays and determines centrosome position. *Embo J* 18:6786-6792.
64. Dujardin, D. L., L. E. Barnhart, S. A. Stehman, E. R. Gomes, G. G. Gundersen, and R. B. Vallee. 2003. A role for cytoplasmic dynein and LIS1 in directed cell movement. *J Cell Biol* 163:1205-1211.
65. Malikov, V., A. Kashina, and V. Rodionov. 2004. Cytoplasmic dynein nucleates microtubules to organize them into radial arrays in vivo. *Mol Biol Cell* 15:2742-2749.

66. Baas, P. W., A. Karabay, and L. Qiang. 2005. Microtubules cut and run. *Trends Cell Biol* 15:518-524.
67. Ferenz, N. P. and P. Wadsworth. 2007. Prophase microtubule arrays undergo flux-like behavior in mammalian cells. *Mol Biol Cell* 18:3993-4002.
68. Hergott, G. J., M. Sandig, and V. I. Kalnins. 1989. Cytoskeletal organization of migrating retinal pigment epithelial cells during wound healing in organ culture. *Cell Motil Cytoskeleton* 13:83-93.
69. Remuzzi, A., C. F. Dewey, Jr., P. F. Davies, and M. A. Gimbrone, Jr. 1984. Orientation of endothelial cells in shear fields in vitro. *Biorheology* 21:617-630.
70. Deck, J. D. 1986. Endothelial cell orientation on aortic valve leaflets. *Cardiovasc Res* 20:760-767.
71. Dartsch, P. C. and E. Betz. 1989. Response of cultured endothelial cells to mechanical stimulation. *Basic Res Cardiol* 84:268-281.
72. Hayakawa, K., N. Sato, and T. Obinata. 2001. Dynamic reorientation of cultured cells and stress fibers under mechanical stress from periodic stretching. *Exp Cell Res* 268:104-114.
73. Wang, J. H., P. Goldschmidt-Clermont, J. Wille, and F. C. Yin. 2001. Specificity of endothelial cell reorientation in response to cyclic mechanical stretching. *J Biomech* 34:1563-1572.
74. Yano, Y., Y. Saito, S. Narumiya, and B. E. Sumpio. 1996. Involvement of rho p21 in cyclic strain-induced tyrosine phosphorylation of focal adhesion kinase (pp125FAK), morphological changes and migration of endothelial cells. *Biochem Biophys Res Commun* 224:508-515.
75. Ghosh, K., C. K. Thodeti, A. C. Dudley, A. Mammoto, M. Klagsbrun, and D. E. Ingber. 2008. Tumor-derived endothelial cells exhibit aberrant Rho-mediated mechanosensing and abnormal angiogenesis in vitro. *Proc Natl Acad Sci U S A* 105:11305-11310.
76. Pradhan, S. and B. Sumpio. 2004. Molecular and biological effects of hemodynamics on vascular cells. *Front Biosci* 9:3276-3285.
77. Lazarides, E. 1975. Immunofluorescence studies on the structure of actin filaments in tissue culture cells. *J Histochem Cytochem* 23:507-528.
78. Gordon, W. E., 3rd. 1978. Immunofluorescent and ultrastructural studies of "sarcomeric" units in stress fibers of cultured non-muscle cells. *Exp Cell Res* 117:253-260.

79. Sanger, J. W., J. M. Sanger, and B. M. Jockusch. 1983. Differences in the stress fibers between fibroblasts and epithelial cells. *J Cell Biol* 96:961-969.
80. Shemesh, T., B. Geiger, A. D. Bershadsky, and M. M. Kozlov. 2005. Focal adhesions as mechanosensors: a physical mechanism. *Proc Natl Acad Sci U S A* 102:12383-12388.
81. Luo, Y. Z., X. Xu, T. Lele, S. Kumar, and D. E. Ingber. 2008. A multi-modular tensegrity model of an actin stress fiber. *Journal of Biomechanics* 41:2379-2387.
82. Chen, J., B. Fabry, E. L. Schiffrin, and N. Wang. 2001. Twisting integrin receptors increases endothelin-1 gene expression in endothelial cells. *Am J Physiol Cell Physiol* 280:C1475-1484.
83. Edlund, M., M. A. Lotano, and C. A. Otey. 2001. Dynamics of alpha-actinin in focal adhesions and stress fibers visualized with alpha-actinin-green fluorescent protein. *Cell Motil Cytoskeleton* 48:190-200.
84. Alenghat, F. J., S. M. Nauli, R. Kolb, J. Zhou, and D. E. Ingber. 2004. Global cytoskeletal control of mechanotransduction in kidney epithelial cells. *Exp Cell Res* 301:23-30.
85. Gelles, J., B. J. Schnapp, and M. P. Sheetz. 1988. Tracking kinesin-driven movements with nanometre-scale precision. *Nature* 331:450-453.
86. Cheezum, M. K., W. F. Walker, and W. H. Guilford. 2001. Quantitative comparison of algorithms for tracking single fluorescent particles. *Biophys J* 81:2378-2388.
87. Umemoto, S. and J. R. Sellers. 1990. Characterization of in vitro motility assays using smooth muscle and cytoplasmic myosins. *J Biol Chem* 265:14864-14869.
88. Endlich, N., C. A. Otey, W. Kriz, and K. Endlich. 2007. Movement of stress fibers away from focal adhesions identifies focal adhesions as sites of stress fiber assembly in stationary cells. *Cell Motil Cytoskeleton* 64:966-976.
89. Hotulainen, P. and P. Lappalainen. 2006. Stress fibers are generated by two distinct actin assembly mechanisms in motile cells. *J Cell Biol* 173:383-394.
90. Hirata, H., H. Tatsumi, and M. Sokabe. 2007. Dynamics of actin filaments during tension-dependent formation of actin bundles. *Biochim Biophys Acta* 1770:1115-1127.
91. Smith, M. A., E. Blankman, M. L. Gardel, L. Luettjohann, C. M. Waterman, and M. C. Beckerle. 2010. A zyxin-mediated mechanism for actin stress fiber maintenance and repair. *Dev Cell* 19:365-376.

92. Russell, R. J., S. L. Xia, R. B. Dickinson, and T. P. Lele. 2009. Sarcomere mechanics in capillary endothelial cells. *Biophys J* 97:1578-1585.
93. Fink, J., M. Thery, A. Azioune, R. Dupont, F. Chatelain, M. Bornens, and M. Piel. 2007. Comparative study and improvement of current cell micro-patterning techniques. *Lab Chip* 7:672-680.
94. Sveen, J. K. 2006. MATPiv. Available at <http://www.math.uio.no/~jks/matpiv/>. Accessed August 20, 2009.
95. Chen, C. S., M. Mrksich, S. Huang, G. M. Whitesides, and D. E. Ingber. 1997. Geometric control of cell life and death. *Science* 276:1425-1428.
96. Parker, K. K., A. L. Brock, C. Brangwynne, R. J. Mannix, N. Wang, E. Ostuni, N. A. Geisse, J. C. Adams, G. M. Whitesides, and D. E. Ingber. 2002. Directional control of lamellipodia extension by constraining cell shape and orienting cell tractional forces. *Faseb J* 16:1195-1204.
97. Tan, J. L., J. Tien, D. M. Pirone, D. S. Gray, K. Bhadriraju, and C. S. Chen. 2003. Cells lying on a bed of microneedles: an approach to isolate mechanical force. *Proc Natl Acad Sci U S A* 100:1484-1489.
98. Chrzanowska-Wodnicka, M. and K. Burridge. 1996. Rho-stimulated contractility drives the formation of stress fibers and focal adhesions. *J Cell Biol* 133:1403-1415.
99. Dickinson, R. B. and D. L. Purich. 2002. Clamped-filament elongation model for actin-based motors. *Biophys J* 82:605-617.
100. Dickinson, R. B., L. Caro, and D. L. Purich. 2004. Force generation by cytoskeletal filament end-tracking proteins. *Biophys J* 87:2838-2854.
101. Mogilner, A. and G. Oster. 2003. Force generation by actin polymerization II: the elastic ratchet and tethered filaments. *Biophys J* 84:1591-1605.
102. Kozlov, M. M. and A. D. Bershadsky. 2004. Processive capping by formin suggests a force-driven mechanism of actin polymerization. *J Cell Biol* 167:1011-1017.
103. Inoue, S. and E. D. Salmon. 1995. Force generation by microtubule assembly/disassembly in mitosis and related movements. *Mol Biol Cell* 6:1619-1640.
104. Tran, P. T., L. Marsh, V. Doye, S. Inoue, and F. Chang. 2001. A mechanism for nuclear positioning in fission yeast based on microtubule pushing. *J Cell Biol* 153:397-411.

105. Howard, J. 2006. Elastic and damping forces generated by confined arrays of dynamic microtubules. *Phys Biol* 3:54-66.
106. Gittes, F., E. Meyhofer, S. Baek, and J. Howard. 1996. Directional loading of the kinesin motor molecule as it buckles a microtubule. *Biophys J* 70:418-429.
107. Dujardin, D. L. and R. B. Vallee. 2002. Dynein at the cortex. *Curr Opin Cell Biol* 14:44-49.
108. Burakov, A., E. Nadezhdina, B. Slepchenko, and V. Rodionov. 2003. Centrosome positioning in interphase cells. *J Cell Biol* 162:963-969.
109. Zhu, J., A. Burakov, V. Rodionov, and A. Mogilner. 2010. Finding the cell center by a balance of dynein and myosin pulling and microtubule pushing: a computational study. *Mol Biol Cell* 21:4418-4427.
110. Bicek, A. D., E. Tuzel, D. M. Kroll, and D. J. Odde. 2007. Analysis of microtubule curvature. *Methods Cell Biol* 83:237-268.
111. Brangwynne, C. P., G. H. Koenderink, E. Barry, Z. Dogic, F. C. MacKintosh, and D. A. Weitz. 2007. Bending dynamics of fluctuating biopolymers probed by automated high-resolution filament tracking. *Biophys J* 93:346-359.
112. Goodwin, S. S. and R. D. Vale. 2010. Patronin regulates the microtubule network by protecting microtubule minus ends. *Cell* 143:263-274.
113. Cole, N. B., N. Sciaky, A. Marotta, J. Song, and J. Lippincott-Schwartz. 1996. Golgi dispersal during microtubule disruption: regeneration of Golgi stacks at peripheral endoplasmic reticulum exit sites. *Mol Biol Cell* 7:631-650.
114. Misra, G. 2010. Multi-scale modeling and simulation of semi-flexible filaments [Dissertation]. Gainesville: University of Florida.
115. Wu, J., G. Misra, R. J. Russell, A. J. C. Ladd, T. P. Lele, and R. B. Dickinson. 2011. Effects of Dynein on Microtubule Mechanics and Centrosome Positioning. *Proc Natl Acad Sci U S A* In Review.
116. Shiu, Y. T., J. A. Weiss, J. B. Hoying, M. N. Iwamoto, I. S. Joung, and C. T. Quam. 2005. The role of mechanical stresses in angiogenesis. *Crit Rev Biomed Eng* 33:431-510.
117. Discher, D., C. Dong, J. J. Fredberg, F. Guilak, D. Ingber, P. Janmey, R. D. Kamm, G. W. Schmid-Schonbein, and S. Weinbaum. 2009. Biomechanics: cell research and applications for the next decade. *Ann Biomed Eng* 37:847-859.

118. Russell, R. J., A. Y. Grubbs, S. P. Mangroo, S. E. Nakasone, R. B. Dickinson, and T. P. Lele. 2011. Sarcomere length fluctuations and flow in capillary endothelial cells. *Cytoskeleton (Hoboken)* 68:150-156.
119. Stachowiak, M. R. and B. O'Shaughnessy. 2009. Recoil after severing reveals stress fiber contraction mechanisms. *Biophys J* 97:462-471.
120. Colombelli, J., A. Besser, H. Kress, E. G. Reynaud, P. Girard, E. Caussinus, U. Haselmann, J. V. Small, U. S. Schwarz, and E. H. Stelzer. 2009. Mechanosensing in actin stress fibers revealed by a close correlation between force and protein localization. *J Cell Sci* 122:1665-1679.
121. Katoh, K., Y. Kano, and S. Ookawara. 2008. Role of stress fibers and focal adhesions as a mediator for mechano-signal transduction in endothelial cells in situ. *Vasc Health Risk Manag* 4:1273-1282.
122. Shirwany, N. A. and M. H. Zou. 2010. Arterial stiffness: a brief review. *Acta Pharmacol Sin* 31:1267-1276.
123. Pelham, R. J., Jr. and Y. Wang. 1997. Cell locomotion and focal adhesions are regulated by substrate flexibility. *Proc Natl Acad Sci U S A* 94:13661-13665.
124. Chin, L. K., J. Q. Yu, Y. Fu, T. Yu, A. Q. Liu, and K. Q. Luo. 2011. Production of reactive oxygen species in endothelial cells under different pulsatile shear stresses and glucose concentrations. *Lab Chip*.
125. Bazzoni, G. and E. Dejana. 2004. Endothelial cell-to-cell junctions: molecular organization and role in vascular homeostasis. *Physiol Rev* 84:869-901.
126. Millan, J., R. J. Cain, N. Reglero-Real, C. Bigarella, B. Marcos-Ramiro, L. Fernandez-Martin, I. Correas, and A. J. Ridley. 2010. Adherens junctions connect stress fibres between adjacent endothelial cells. *BMC Biol* 8:11.
127. Dembo, M. and Y. L. Wang. 1999. Stresses at the cell-to-substrate interface during locomotion of fibroblasts. *Biophys J* 76:2307-2316.
128. Miyake, K. and P. L. McNeil. 2003. Mechanical injury and repair of cells. *Crit Care Med* 31:S496-501.
129. Clarke, M. S., R. Khakee, and P. L. McNeil. 1993. Loss of cytoplasmic basic fibroblast growth factor from physiologically wounded myofibers of normal and dystrophic muscle. *J Cell Sci* 106 (Pt 1):121-133.

BIOGRAPHICAL SKETCH

Robert J. Russell was born in Philadelphia, PA to Robert F. Russell and Nancy Clarke. After his graduation from Downingtown High School in 2001, he enrolled at Carnegie Mellon University in Pittsburgh, PA. While at Carnegie Mellon he double majored in chemical engineering and biomedical engineering with a minor in colloids, polymers and surfaces. During his time at Carnegie Mellon, Robert interned with MAB Paints in Philadelphia, PA and Bayer Materials Science in Pittsburgh, PA. Upon graduation from Carnegie Mellon in May 2006, he entered the Department of Chemical Engineering at the University of Florida as a graduate student in August 2006. He started work under Professors Tanmay Lele and Richard Dickinson in January 2007. During his time with Professors Lele and Dickinson he has studied force generation in actin stress fibers and the microtubule cytoskeleton of endothelial cells.